Model Reference Adaptive Control Laws: Application to Nonlinear Aeroelastic Systems

PhD Thesis submitted to the
Politecnico di Torino
in partial fulfillment of the requirements for the

Doctor of Philosophy
in
Aerospace Engineering

Mario Cassaro _____

Prof. P. Gili _____

Prof. M. Battipede _____

Prof. P. Marzocca _____

March 2015, Turin, Italy

To you all

Contents

List of Figures

List of Tables

Nomenclature

α	Aerodynamic Angle of Attack
β	Trailing edge flap deflection angle
μ_α	Coulomb damping coefficient for pitch degree of freedom
μ_h	Coulomb damping coefficient for plunge degree of freedom
ρ	Air density
θ	Static angle of attack
ζ	Nonlinear stiffness parameter for pitch degree of freedom
ζ	Nonlinear stiffness parameter for plunge degree of freedom
a	Nondimensional distance from the midchord to the elastic axis
b	Semichord of the wing
$c.g.$	Center of gravity
c_α	Wing section pitch damping coefficient
c_h	Wing section plunge damping coefficient
$C_{L_\alpha} C_{m_\alpha}$	Lift and moment curve slopes per angle of attack
$C_{L_\beta} C_{m_\beta}$	Lift and moment curve slopes per control surface deflection
h	Plunge displacement
I_α	Airfoil section torsional inertia
i_{sp}	Number of active spoilers
k_α	Wing section pitch stiffness
k_h	Wing section plunge stiffness
K_{red},$K_{reduced}$	Reduced Stiffness for Failure simulation

m_T	Aeroelastic system total mass
m_w	Wing section mass
U	Freestream velocity
$w_G(\tau)$	Gust velocity profile per dimensionless time
x_α	Nondimensional distance from the center of mass to the elastic axis
AoA	Angle of attack
CFD	Computational Fluid Dynamics
LCO	Limit Cycle Oscillation
LTI	Linear time invariant
MIMO	multi-input multi-output
MPS	Model Positioning System
MRAC	Model Reference Adaptive Control
MRC	Model Reference Control
NATA	Nonlinear Aeroelastic Test Apparatus
PID	Proportional, Integral and Derivative control law
PPC	pole placement control
PSD	Power Spectral Density
SISO	single-input single-output

Acknowledgements

This dissertation is a report of the research work I have done during my Ph.D. studies at Politecnico di Torino and Clarkson University (NY, USA) from 2012. In these years I have worked with a number of people whose contribution made this work possible. It is a great pleasure to convey my gratitude at the beginning of this report.
First, I want to express my infinite gratitude to Professor Manuela Battipede for her guidance, support and for being of continuous inspiration and motivation, and together with Professor Piero Gili for letting me feeling like part of a great big family.
It has been my great privilege and experience to have Professor Piergiovanni Marzocca as mentor at Clarkson University. I am grateful to him for his instructions, guidance, and support. He led me into the area of aeroelastic modeling and control and inspired me with his vision and expertise during my permanence abroad. Apart from providing technical directions, he has been an invaluable sources of advices and a model to pursue on how to behave in a research work environment. Hoping this was just the beginning of a long lasting cooperation.
I would like to thank Professor Enrico Cestino for giving me the opportunity to move abroad and starts this exceptional experience as visiting researcher in the States within the A2NetTeam project, founded by EU Marie Curie program.
I also have a list of other Professors and Researchers that I had the opportunity to work with or just discuss about scientific topic of any kind: Professor Aman Behal, Professor Giacomo Frulla and Dr. Paolo Gunetti, thank you all for sharing part of your knowledge with me, your insightful words and suggestions have enlighten my research studies more then once. Moreover, three years of intense research activities performed in two different universities led me to meet and work with a lot of people, that I really esteem as co-workers and as friends. For this reason I want to apologize if somebody will be forgotten, but I have truly learned a lot from all of you and shared really good time: Matteo Vazzola, Andrea Ferrero, Angelo Lerro, Giuseppe Sirigu, Tyler Arsenault, Joushua Khes, Bruce Almstrom, Gildo Torres and Andras Nagy. Last, but certainty not least, my big family needs a huge acknowledgment for all they have always done for me. Thank you all.

Abstract

Nonlinear Aeroelastic Control has been a research topic of great interest for the past few decades. Different approaches has been attempted aiming to obtain better accuracy in the model dynamics description and better control performance. As far as the aeroelastic mathematical model is concerned, the scientific world converged in the use of a bi-dimension, two degree of freedom, plunging and pitching, wing section model, of which the bigger advantages are to be reproducible experimentally with an appropriate wind tunnel apparatus and to allow LCO (Limit Cycle Oscillation) exhibition at low values of wind speed, facilitating parametric studies of the nonlinear aeroelastic system and its control architecture. A parametric analysis of the linearized system, typical of aircraft flight dynamic studies, is employed to verify and validate the model dynamic properties dependency, focusing in particular to the effect of stiffness reduction as means of failure simulation. In fact, despite of the recent years flourishing literature on aeroelastic adaptive controls, there is a noted lack of robustness and sensitivity analysis with respect to structural proprieties degradation which might be associated with a structural failure. Structural mode frequencies and aeroelastic response, including Limit Cycle Oscillations (LCOs) characteristics, are significantly affected by changes in stiffness. This leads to a great interest in evaluating and comparing the adaptation capabilities of different control architectures subjected to large plant uncertainties and unmodeled dynamics. Motivated by the constantly increasing diffusion of the new L_1 adaptive control theory, developed for the control of uncertain non-autonomous nonlinear systems, and by the fact that its application to aeroelasticity is in its infancy, a deep investigation of this control scheme properties and performance drew our attention. The new control theory is conceptually similar to the Model Reference Adaptive Control (MRAC) theory to which has often been compared indeed for performance evaluation purpose. In this dissertation, a comprehensive analysis of the new control theory is obtained by performance evaluation and comparison of four different control schemes, two MRAC and two L_1, focusing the attention on the states and control input time response, adaptive law parameters' convergence, transient evolution and fastness, and robustness in terms of tolerance of uncertainties in off-design conditions. The objective is pursued by re-

writing the aeroelastic model nonlinear equations of motion in an amenable form to the development of the four different control laws. The control laws are then derived for the appropriate class of plant which the system belongs to, and design parameter obtained, when necessary, following the mathematical formulation of the control theories developers. A simulation model is employed to carry out the numerical analysis and to outline pros and cons of each architecture, to obtain as final result the architecture that better fits the nonlinear aeroelastic problem proposed. This methodology is used to guarantee a certain robustness in controlling a novel actuation architecture, developed for flutter suppression of slender/highly flexible wing, based on a coordinated multiple spoiler stripe, located at fifteen percent of the mean aerodynamic chord. The control actuation system design, manufacturing and experimental wind tunnel test is part of the dissertation. Two different experimental setup are developed for two different purpose. First, a six-axis force balance test is carried out to validate the numerical aerodynamic results obtained during the validation process, and to collect the aerodynamic coefficient date base useful for the development of the simulation model of the novel architecture. The second experimental apparatus, is a two degree of freedom, plunging/pitching, system on which the prototyped wing section is mounted to obtain LCO aeroelastic response during wind tunnel experiment. The nonlinear aeroelastic mathematical formulation is modified to take into account of the novel actuation architecture and, coupled with the more robust MRAC control laws derived for the previous model, serves as benchmark for properties assessment of the overall architecture, for flutter suppression. The novel control actuation architecture proposed, is successfully tested in wind tunnel experimentation confirming the validity of the proposed solution. This dissertation provides a step forward to the definition of certain MRAC control schemes properties, and together provides a novel actuation solution for flutter suppression which demonstrates to be a viable alternative to classical leading and/or trailing-edge flap architecture or to be used as redundancy to them.

Chapter 1

Introduction

1.1 Motivation

Analysis and control of aeroelastic phenomena affecting different type of slender structure has been a flourishing research topic for the past few decades. Of great interest, because of its criticality, flutter and adaptive control strategies to suppress nonlinear dynamic aeroelastic instabilities are investigated. Although flutter boundaries in most cases can be theoretically and experimentally determined, significant decays in flutter speed can suddenly occur with dramatic implications for the system structural integrity. Several passive methods used to address this problem include added structural stiffness, mass balancing, and speed restrictions [1]. However, the attempt to enlarge the operational range of any high flexible lifting structures and to enhance the aeroelastic response following these traditional methods result in significant weight penalties or in unavoidable reduction of nominal performances [2, 3]. All of these factors fully underline the necessity of the implementation of an active control capability enabling one to fulfill the two basic objectives of 1) enhanced subcritical aeroelastic response, in the sense of suppressing or even alleviating the severity of the wing oscillations in the shortest possible time, and 2) expanded flight envelope by suppressing flutter instability, thereby contributing to a significant increase in the allowable operational speed [4]. In this respect both supercritical and subcritical nonlinear response in the proximity of the flutter boundary can be controlled with beneficial results. The interest in the development and implementation of active control technology was prompted by the new and sometimes contradictory requirements imposed on the design of the new generation of the flight vehicle that mandated increasing structural flexibilities; high maneuverability; and, at the same time, the ability to operate safely in severe environmental conditions. Recently, a new L_1 adaptive control theory has been developed for the control of uncertain non-autonomous nonlinear systems [5, 6, 7, 8]. The controller is based on a state predictor

similar to indirect adaptive systems and the control input is obtained by a low-pass filtering of the estimated control signal. This should decouple robustness from fastness of adaptation and, so forth, allowing to increase the adaptive gain of the adaptive law to very high values to improve transient performance. The application of L_1 adaptive theory to aeroelasticity is in his infancy, [9, 10], and investigations of the performances for several flight conditions are of great interest. In addiction, the development of L_1 adaptive flutter controllers and their results comparison with other model reference adaptive control (MRAC) schemes [11], are an important benchmark to assess the properties of some important modifications that L_1 control theory introduces with respect to the standard MRAC. The type of aeroelastic model selected for the implementation and verification of the different control strategies bi-dimensional, two degree of freedom, plunging/pitching, structurally nonlinear lifting surface in a quasi-steady flow, which has been traditionally used for the theoretical as well as experimental analysis of flutter and post-flutter dynamics. The model has pitch polynomial type structural nonlinearities and uses a single moving surface, a trailing-edge flap, for the purpose of control. It is assumed that all of the system parameters, except the sign of a single control input coefficient, are unknown. It was assumed a quasi-steady linear aerodynamic, a relatively acceptable assumptions for the purpose of comparison; needless to say, it is possible to extend this approach to account for linear/nonlinear unsteady aerodynamic models more suitable for reduced frequencies sufficiently large, $k = \omega b/U > 0.04$, where ω is the oscillatory frequency, b is the semi-chord, and U is the flow speed, and in the presence of dynamic stall and flow separation. Below 0.04, a quasi-steady approximation is usually sufficient to predict accurate loads on thin airfoils. However, it is worth mentioning, although the mechanism of flutter is usually correctly identified, a quasi-steady approximation might not always provide the correct flutter speed. The proposed aeroelastic model exhibits a supercritical Hopf-bifurcation behavior, that is at free-stream velocity exceeding the critical flutter value, a stable Limit Cycle Oscillations (LCO) occurs. The investigation proposed is moreover intended to be used to critically select a robust adaptive control scheme to be applied to a novel control actuation architecture for flutter suppression. The amount of uncertainties, unknowns and unmodeled dynamics of the novel aeroservoelastic system dynamics jointly with the future, real-world, hardware-in-the-loop application of the system itself justify the need to research for the Model Reference Adaptive Control scheme that demonstrates better performance in terms of robustness and adaptation capabilities.

1.2 Preliminaries

The dictionary definition of "to adapt" is: to change (oneself) so that one's behavior will conform to new or changed circumstances. [12, 13] testify that the words "adaptive systems" and "adaptive control" have been used as early as 1950. The main motivation, that pushed the scientist to design control law with adaptive capabilities, was the need of autopilots for high-performance aircraft in the early 1950s. The nonlinear, time varying dynamics of the aircraft and the fact that the boundaries of the flight envelope started to become really wide, represented criticality very difficult to overtake with classical linear control system. The most common solution, that has been widely used in aircraft control design, from the 70's [14] to nowadays [15], consists of linearizing the aircraft mathematical model for a given flight condition, defined by flight speed (Mach number), altitude, weight, center of gravity position and external body configuration (flap and gear extraction). State-space formulation very well suits the linearization problem control designer had to face. In general:

$$\begin{aligned} \dot{x} &= A_i x + B_i u, \qquad x(0) = x_0 \\ y &= C_i^T x + D_i u \end{aligned} \tag{1.1}$$

where A_i, B_i, C_i and D_i are functions of the operating point i. This means that, as the aircraft changes flight condition, the operating point changes as well, leading to different system matrices. An extensive aircraft dynamic analysis of a B747-100, containing state-space LTI approximation of the aircraft model for the entire flight envelope can be found in [16]. This kind of analysis have been used, as in the past and current aircraft era, to design gain scheduling based control law able to guarantee robustness and required performances. However, the amount of work that is behind an aircraft controller optimization process, and the possibility to encounter unpredicted flight condition lead to the idea that a sophisticated feedback controller should be able to learn about parameter changes by processing the system output $y(t)$ and use the appropriate gains to accommodate them. This approach led to the control structure, on which adaptive control is based, that consists of a feedback loop where a block-set is dedicated to dynamically adjust the control loop gains. The internal mathematical formulation, and consequently the algorithm, of the adjustable mechanism classifies the adaptive control scheme. Finally, an adaptive controller is defined as an algorithm able to alter or modify the dynamic response of an unknown plant to meet certain performance requirements. Where, by plant is intended any dynamic process characterized by a certain number of inputs, usually defined as u, and outputs, referred to as y. The control objective is so to choose the input u so that the output$y$ satisfies certain given performance requirements (e.g. tracking error, regulation error, time rise, boundedness).

1.2.1 Direct and Indirect Adaptive Control

In general there are two main categories of adaptive controllers, based on the loop features. They are both formed by combining an on-line parameter estimator, which provides estimates of unknown parameters at each instant, with a control law that is motivated from the known parameter case. The way the parameter estimator, also referred to as *adaptive law*, is combined with the control law defines the to two main approaches. In the first approach, referred to as *indirect adaptive control*, the plant parameters are estimated on-line and used to calculate the controller parameters. This approach has also been referred to as *explicit adaptive control*, because the design is based on an explicit plant model. The second approach, referred to as *direct adaptive control*, the plant model is parameterized in terms of the controller parameters that are estimated directly without intermediate calculations involving plant parameter estimates. This approach has also been referred to as *implicit adaptive control* because the design is based on the estimation of an implicit plant model. In indirect adaptive control, the plant model is parameterized with respect to some unknown parameter vector. For example, for a linear time invariant (LTI) single-input single-output (SISO) plant model, may represent the unknown coefficients of the numerator and denominator of the plant model transfer function. An on-line parameter estimator generates an estimate at each time t by processing the plant input $u(t)$ and output $y(t)$. The unknown parameter estimate specifies an estimated plant model, that for control design purposes is treated as the "true" plant model and is used to calculate the controller parameter or gain vector by solving a certain algebraic equation at each time t. It is, therefore, clear that with this approach, the control law is designed at each time t to satisfy the performance requirements for the estimated plant model, which may differ from the unknown plant model. Therefore, the principal problem in indirect adaptive control is to choose the class of control laws and the class of parameter estimators as well as the algebraic equation that relates the unknown parameter estimation to the control law parameter so to meet the performance requirements for the plant model with unknowns. In direct adaptive control, the plant model itself is parameterized in terms of the unknown controller parameter vector estimation, for which the controller meets the performance requirements, to obtain the plant model with unknowns to behave exactly with the same input/output characteristics of the nominal plant. The on-line parameter estimator is designed based on the desired plant dynamics to provide the estimation of the unknown parameters at each time t by processing the plant input $u(t)$ and output $y(t)$. The estimate of the unknowns is then used to update the controller parameter vector without intermediate calculations. The properties of the nominal plant model are crucial in obtaining the parameterized plant model that is convenient for on-line estimation. As a result, direct adaptive control is re-

stricted to a certain class of plant models, in particular as it will be proven in Chapter 2, the class of plant suitable for direct adaptive control consists of SISO LTI plant models that is minimum-phase, i.e., the zeros are located in $Re[s] < 0$. The principle behind the design of direct and indirect adaptive control is conceptually simple. The design of the control law treats the estimates of the plant unknown parameters (in the case of direct adaptive control) or the estimates of certain parameters from which the unknown are computed after (in the case of indirect adaptive control) as if they were the true parameters. This design approach is called *certainty equivalence* and can be used to generate a wide class of adaptive control schemes by combining different on-line parameter estimators with different control laws. The idea behind the certainty equivalence approach is that as the variable/ unknown parameter estimates converge to the true ones the performance of the adaptive controller tends to that achieved in the case of known parameters. The distinction between direct and indirect adaptive control may be confusing for the following reasons: the direct adaptive control structure can be made identical to that of the indirect adaptive control by including a block for calculations with an identity transformation between updated parameters and controller parameters. In general, for a given plant model the distinction between the direct and indirect approach becomes clear if we go into the details of design and analysis. For example, direct adaptive control can be shown to meet the performance requirements, which involve stability and asymptotic tracking, for a minimum-phase plant. It is still not clear how to design direct schemes for nonminimum-phase plants. The difficulty arises from the fact that, in general, a convenient (for the purpose of estimation) parameterization of the plant model in terms of the desired controller parameters is not possible for nonminimum-phase plant models. Indirect adaptive control, on the other hand, is applicable to both minimum- and nonminimum-phase plants. In general, however, the mapping between the updated parameters and the controller parameters cannot be guaranteed to exist at each time t giving rise to the so-called *stabilizability* problem. Solutions to the stabilizability problem are possible at the expense of additional complexity. Efforts to relax the minimum-phase assumption in direct adaptive control and resolve the stabilizability problem in indirect adaptive control led to adaptive control schemes where both the controller and plant parameters are estimated on-line, leading to combined direct/indirect schemes that are usually more complex.

1.2.2 Model Reference Adaptive Control

Model reference adaptive control (MRAC) is derived from the model following problem or model reference control (MRC) problem, where the idea is to let the plant behave as a desired model by properly closing the loop. The objective of MRC is to find the feedback control law, so that the closed-loop

dynamics of the plant, that is its I/O properties, are exactly the same as those of a reference model. Where the reference model is a dynamic system, with prescribed characteristics, that the designer wants the plant to follow. In MRC, the plant parameters and its dynamic properties must be known, so to allow the design a proper reference model. The structure of an MRC scheme for a LTI, SISO plant is shown inFigure 1.1. The transfer function $W_m(s)$, is the expression of the reference model dynamic in the s domain. It is designed so that for a given reference input signal $r(t)$ the output $y_m(t)$ of the reference model $W_m(s)$ represents the desired response the plant output $y(t)$ should follow. The feedback control law, denoted by $C(\theta_c^*$, is designed so that all signals are bounded and the closed-loop plant transfer function from r to y is equal to $W_m(s)$. Is this transfer function matching is guaranteed, than for any given reference input $r(t)$, the tracking error $e_1 \triangleq y - y_m$, which represents the deviation of the plant output from the desired trajectory y_m, converges to zero with time. The transfer function matching is obtained by canceling the zeros of the plant transfer function $G(s)$ and replacing them with those of $W_m(s)$. This goal can be accomplished by using the feedback controller $C(\theta_c^*$ to generate a control signal that nullify the effect of the unwanted dynamics, or by pole placement which works directly by poles-zeros superposition, as known as pole placement control (PPC). Hence, in the first case, the plant needs to be minimum-phase, all the zeros located in the left hand side of the complex plane, and so stable, counteracting the effect of unstable zeros may easily lead to unbounded signals. In the PPC, this last assumption does not stand, because no matter where the zeros are located, superimposed poles cancel out their effect. Without any adaptation law, the PPC requires knowledge of the exact location of the plant zeros and poles. Whereas, in the MRC scheme Figure 1.1, the design of $C(\theta_c^*$ requires the full knowledge of the coefficients of the plant transfer function $G(s)$. Defining θ^* as a vector containing all the coefficients of $G(s) = G(s, \theta^*$, then the parameter vector θ_c^* may be computed by solving an algebraic equation of the form

$$\theta_c^* = F(\theta^*) \tag{1.2}$$

Unknown θ^* implies that θ_c^* cannot be calculated using (1.2), thus the MRC scheme cannot be implemented. The adaptive version of MRC, referred to as model reference adatpive control (MRAC), overtake this problem by the use of the certainty equivalence approach to replace the unknown θ_c^* in the control law with its estimate θ_c obtained using the direct or the indirect approach. The resulting control schemes can be classified as indirect MRAC shown in Figure 1.2 and direct MRAC shown in Figure 1.3. MRAC scheme are then further classified by the different choices of on-line parameter estimators.

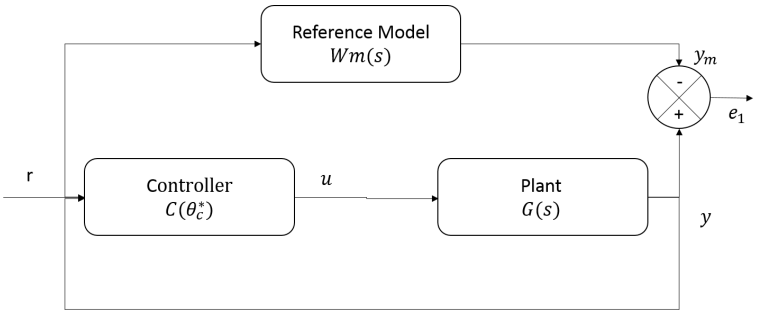

Figure 1.1: Model Reference Control

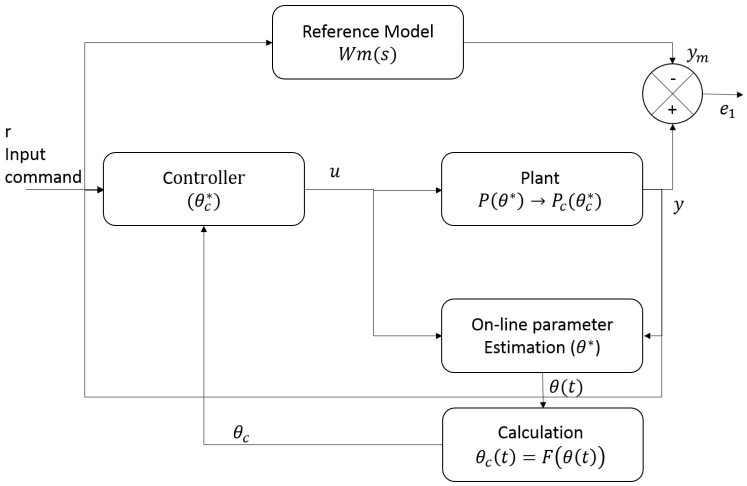

Figure 1.2: Indirect MRAC

In practice, the general problem formulation for a direct MRAC control law design is expressed in time domain, with a state-space formulation, where the states dynamic, of the plant $G(s)$, are described as follows, where the unknowns are separated form the known stable part of the system:

$$\dot{x}(t) = A_m x(t) + B\theta^{*^T} x(t) + Bu(t) \tag{1.3}$$

where $x \in \mathbb{R}^n$ is the state vector, assumed to be measurable ($n = 2$), $u \in \mathbb{R}$ is the control input, $\theta^* \in \mathbb{R}^n$ is an unknown parameter vector belonging to a known compact convex set $\Omega \in \mathbb{R}^n$, $A_m \in \mathbb{R}^{n \times n}$ is Hurwitz [89] and with $B \in \mathbb{R}^n$ are known, and the pair $(A_m; B)$ is controllable (if the eigenvalues of Am are not in desired locations, they can be arbitrarily assigned by a simple state feedback gain). The objective is to choose $u(t)$ such that all signals in the closed-loop system are uniformly bounded and $x(t)$ tracks the

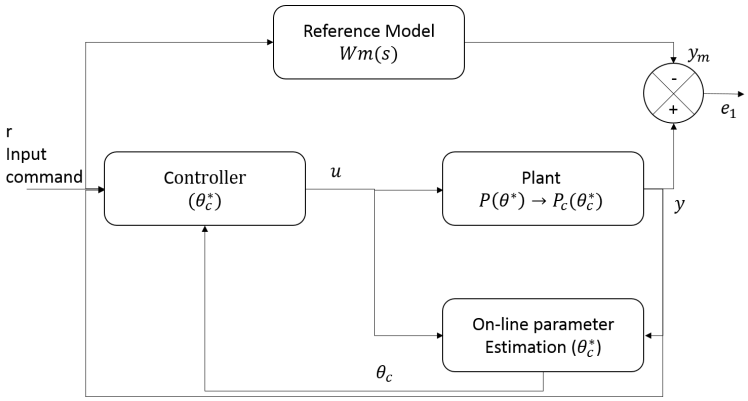

Figure 1.3: Direct MRAC

state vector of the desired reference model

$$\dot{x}_m(t) = A_m x_m(t) + B_m r(t), \qquad x_m(0) = x_0 \tag{1.4}$$

both in transient and in steady-state for any bounded reference signal $r(t)$, where $B_m = k_0 B$, for some $k_0 \in \mathbb{R}$. To this end, it is clear that the dynamics that has to go to zero is referred to the state tracking error, defined as

$$e(t) = x(t) - x_m(t) \tag{1.5}$$

The solution for $u(t)$ and the different adaptive law to compute $\hat{\theta}(t)$ the estimate of $\theta^*(t)$ defines the different type of MRAC scheme. The stability proofs can be found in [87].

1.2.3 Historical Overview

The early 50s, when the design of autopilots for high-performance aircraft motivated the need for controller able to operate in a wider range of flight conditions, have seen the development of an intense research activity in adaptive control. Constant-gain feedback controller were not able any more to satisfy the more demanding requirements, for the always increasing aircraft performances. The idea of a sophisticated controller, such as an adaptive controller, that could modify its own behavior learning and accommodating environmental and changes in the aircraft dynamics started to be investigated. Whitaker et al. in [17, 18] suggested Model reference adaptive control to solve the autopilot control problem. The sensitivity method and the MIT rule was used to design the adaptive laws of the various proposed adaptive control schemes. Kalman in [19] proposed an adaptive pole placement scheme based on the optimal linear quadratic problem. The early age of adaptive flight control was characterized by “a lot of enthusiasm,

bad hardware and non-existing theory" [20]. However, the lack of stability proofs and the lack of understanding of the properties of the proposed adaptive control schemes, coupled with a disaster in a flight test [21], caused the interest in adaptive control to diminish.

The most flourishing period, for the adaptive control and the development of control theory in general, have been the 60's. It has been at that time that new techniques, based for example on the state-space formulation and the famous Lyapunov stability theory, have been introduced. A key role in the reformulation and redesign of adaptive control have been played by the developments in dynamic programming [22, 23], dual control [24] and stochastic control in general, and in system identification and parameter estimation [25, 26]. By '66 the Lyapunov design approach has been used by Parks and others to redesigned the MIT rule-based adaptive laws used in the MRAC schemes of the 50s. Their work, even applicable only to a special class of LTI plants, pave the way for further rigorous stability proofs in adaptive control for more general classes of plant models. The improved understanding of adaptive control architectures, due to the advances in stability theory and the progress in control theory in the 60s, contributes to a new impulse of interest in the field in the 70s. This went together with the rising interest in the applications of adaptive control, made possible by the simultaneous development and progress in computers and electronics that made the implementation of complex controllers feasible. Several breakthrough results in the design of adaptive control theory have been presented in the 70s. MRAC schemes using the Lyapunov stability based design approach were designed and analyzed in [27, 28, 29]. Other mathematical tools, such as the concepts of positivity and hyperstability were used in [30] to develop a wide class of MRAC schemes with well-established stability properties. In the same ages, parallel efforts for discrete-time plants in a deterministic and stochastic environment lead to the development of several classes of adaptive control schemes with rigorous stability proofs [31, 32]. The excitement of the 70s and the development of a wide class of adaptive control schemes with well established stability properties have been also accompanied by several successful applications [33, 34, 35]. The successes of the 70s, however, were soon followed by controversies over the practicality of adaptive control. Robustness investigations, in 1979, have pointed out that the adaptive schemes of the 70s could easily go unstable in the presence of small disturbances [27]. This has been followed by a significant number of publication about the non-robust behavior of adaptive control schemes, which has become very controversial in the early 80s when more examples of instabilities demonstrates lack of robustness in the presence of unmodeled dynamics or bounded disturbances [36, 37]. This acted as a new stimulus for the researcher world, where scientist's objective was to understand the mechanisms of instabilities and find ways to counteract them. By the mid 80s, other modifications and redesigned architectures have been proposed

and analyzed, leading to what is known as robust adaptive control. The robustness definition for an adaptive controller is: "an adaptive controller is defined to be robust if it guarantees signal boundedness in the presence of "reasonable" classes of unmodeled dynamics and bounded disturbances as well as performance error bounds that are of the order of the modeling error". Several modification have been introduced later on, during the 80s, to improve control scheme's robustness. This implied the understanding of the various robustness modifications and their unification and classification under a more general framework [27, 38, 39]. The solution of the long-standing problem of controlling a linear plant whose parameters are unknown and changing with time can be considered achieved by the solution of the robustness problem in adaptive control. Other breakthrough results have been published in the area of adaptive control for linear time-varying plants by the end of the 80s several [40]. At this end, the adaptive control research has been focused on the performance properties definition and their improvement as objective, in the late 80s to early 90s, and on extending the results of the 80s to certain classes of nonlinear plants with unknown parameters. Consequently, new classes of adaptive schemes have been derived and implemented in the past decades, such as adaptive control schemes with improved transient and steady-state performance [43, 44], and motivated from nonlinear system theory [41, 42]. In the recent year, one of the most discussed adaptive control law theory, known as L_1 *adaptive control* has born and risen very quickly. This novel architecture should be able of arbitrary tracking error performance and "separation of performance improvement from robustness" achieved by filtering the plant input and boosting the adaptive gain of the estimated parameters to very large values [7, 45, 46, 8, 6, 5]. Adaptive control has a rich literature full with different techniques for design, analysis, performance, and applications. Several survey papers, and books and monographs have already been published. Despite the vast literature on the subject, there is still a general feeling that adaptive control is a collection of unrelated technical tools and tricks.

1.2.4 L1 Adaptive Control

The major issues that have been encountered in the application of MRAC schemes concerns several aspects among which the high-frequency or large amplitudes control signals, large transient errors or slow convergence rate of tracking errors, are cases in point. With L_1 adaptive control architectures, it is stated that fast adaptation appears to be beneficial both for performance and robustness, while the trade-off between the two is resolved via the selection of a filter, referred to as $C(s)$, placed in a particular point of the control loop, acting on the control law output as shown in Figure 1.4.

The problem formulation consists of considering the plant with following

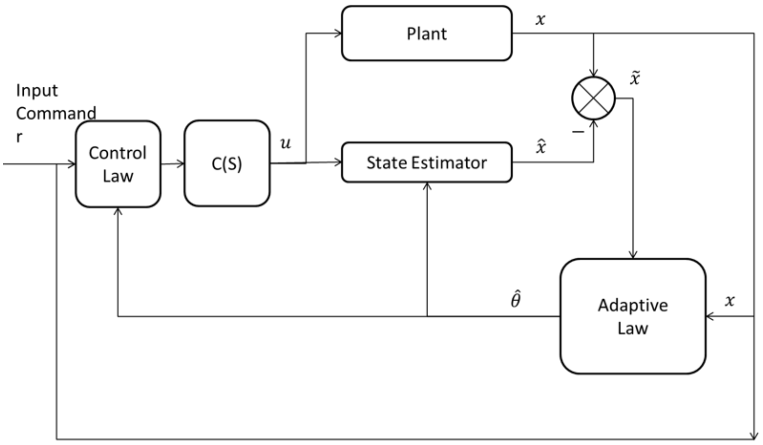

Figure 1.4: L1 Adaptive Control Architecture

dynamics:

$$\dot{x}(t) = Ax(t) + Bu(t), \qquad u(t) = [C(u)](t) \tag{1.6}$$

where $x \in \mathbb{R}^n$ is always the system state vector. $A \in \mathbb{R}^{n\times n}$ may be unknown or unstable, or even change in time in function of external factors. The L_1 control theory assumes that there exist a known and stable matrix $A_m \in \mathbb{R}^{n\times n}$ and a vector of ideal parameters $\theta \in \mathbb{R}^n$, such that the pair $(A_m; B)$ is controllable and $A - A_m = B\theta^T$. The time-varying unknown parameter vector θ belongs to a given compact convex set Θ. The input control signal pass through the filter $C(s)$ before acting on the plant. The architecture is then based on a state predictor which is written as

$$\dot{\hat{x}}(t) = A_m\hat{x}(t) + B(\hat{\theta}^T x(t) + u(t)), \quad \hat{x}(0) = x_0 \tag{1.7}$$

where A_m is the same Hurwitz matrix of the MRAC achitecture, $\hat{x}(t)$ are the predicted states, $x(t)$ are the actual sytsem states, $u(t)$ is the filtered control signal and $\hat{\theta}$ is again the estimate of the unknown parameters computed by the adaptive law. In this case the convergence is obtained for the tracking error, computed between the state and its prediction, as:

$$\tilde{x}(t) = x(t) - \hat{x}(t). \tag{1.8}$$

Recent studies,[91], have claimed that none advantages are derived from the different problem formulation and proposed solution of the L_1 control theory with respect to the MRAC architecture. A deep analysis of different MRAC and L_1 control schemes' pros and cons is reported in this work, with numerical proofs to support the several findings.

1.3 Contribution of the Dissertation

1.3.1 Aeroelastic Nonlinear Adaptive Control: Derivation, Implementation and Performance Analysis

The emphasis in this dissertation focuses on the derivation, implementation and performance analysis of four different model reference control schemes: a Standard MRAC; a MRAC modified for performance improvement both in transient and steady tracking error, also called in the discussion *Modified MRAC*; a L_1 for systems with unknown constant parameters, called *Standard* L_1; and a L_1 for systems with uncertain system input gain, also called *Modified* L_1. None of this adaptive control schemes has never been derived or implemented for the bi-dimensional nonlinear aeroelastic model proposed, to the best of the author knowledge. Moreover, despite of the recent years flourishing literature on aeroelastic adaptive controls, there is a noted lack of robustness and sensitivity analysis with respect to structural proprieties degradation which might be associated with a structural failure. Structural mode frequencies and aeroelastic response, including Limit Cycle Oscillations (LCOs) characteristics, are significantly affected by changes in stiffness. This leads to a great interest in evaluating and comparing the adaptation capabilities of different control architectures subjected to large plant uncertainties and unmodeled dynamics. In this way, this investigation aims to be a starting point, and a benchmark, for the future evaluation of other additional modifications to the standard model reference adaptive control laws.

1.3.2 Novel Flutter Suppression Actuation Architecture: Design, Prototyping, Simulation and Testing

Part of the research reported in this dissertation has been spent in the design and investigation of the effectiveness of an original actuation architecture, which could represent a possible alternative or redundant system to support the trailing-edge action. Specifically, a novel coordinated multiple spoiler actuation strategy for flutter suppression, is evaluated. A cross simulation/experimental approach is used to obtain the final configuration of the actuation system. The innovative test article consists of a wing section equipped with multiple-spoilers installed on a strip, located at the 15% of the chord length, with a predefined and coordinated actuation strategy. The proposed architecture, optimized through computational fluid dynamics (CFD) analysis, is fabricated and tested in the wind tunnel to validate the aerodynamic properties of the wing section. The experimentally obtained nonlinear aerodynamic database is used in conjunction with a classical nonlinear plunging/pitching structural model, implemented in a simulation environment, to investigate the dynamic response of the proposed

wing configuration aeroelastic model. The resulting aeroelastic model exhibits a supercritical Hopf-bifurcation behavior, that is a stable Limit Cycle Oscillations (LCOs) past the flutter speed. The open and closed loop responses of the system are investigated and compared to a trailing-edge flap solution of the same wing section. The regulation problem is obtained for *Modified MRAC* scheme, which validates the robustness and the adaptation capabilities demonstrated in the classic wing configuration, on which it was previously tested. Proves of the efficacy and solidity of the overall architecture investigated are provided. Experimental test campaign supports the new concept idea as a viable solution for future light unmanned aircraft applications that possibly will be patented.

1.4 Organization of the Dissertation

In Chapter 2 a detailed description of the aeroelastic mathematical models implemented in the simulation environment is provided with particular attention on the wing section properties to ensure correct application of the several control laws applied. The four different model reference adaptive controller are accurately described in Chapter 3. Controller architecture, mathematical formulation and design parameters' values are provided for completeness, making the proposed scheme reproducible to the reader. Chapter 4 provides simulation results and discussions, particularly focused on finding explanations about the correlation between the changes in the closed-loop dynamic response and the scheme modifications that imply them. In Chapter 5 the novel actuation architecture for flutter suppression is presented. In particular the discussion is focused on the description of the design process, the realization of the prototype and the description of the two experimental setup used respectively to validate the CFD simulation results first, and to verify the effectiveness of the actuation solution in a closed-loop hardware-in-the -loop configuration. Chapter 6 provides the experimental tests results and an exhaustive discussion on the major outcomes of the exploratory campaign. Conclusions are provided in Chapter 7.

Chapter 2

Aeroelastic Nonlinear Dynamic Models

Aeroelasticity is the phenomena resulting from the interaction of structural, inertial, and aerodynamic forces. Initially, the aeroelastic behavior investigation relied on a linear approximation of the flow field and structure governing equations. Conversely, aerospace systems are inherently nonlinear from both structural and aerodynamic point of view [1, 47, 48]. Unsteady aerodynamic, large strain-displacement conditions, or the partial loss of structural or control integrity, all of them are sources of nonlinearities as far as slender wing are concerned. The consequent system nonlinear dynamic response exhibits characteristics such as limit cycle oscillations (LCOs), internal resonances, and chaotic motion. Deep analyses about the inaccuracy of the linearized model are reported in [49, 50], where discrepancy between linear approximation predictions and real applications are analyzed for a two degrees-of-freedom spring-pendulum system and a spoiler-wing wind-tunnel test configuration. All this reasons, brought the scientists to investigate for decades all the possible causes of nonlinearities and finally, to build extremely accurate mathematical model to describe the nonlinear dynamic response [51, 52, 53, 54, 55]. The historical process that lead to write the aeroelastic model equation as presented in this dissertation is out of the bound of the proposed research. Nonetheless, an accurate description of the mathematical models, used as they were or modified to account for novel actuation system, will be given in this chapter. Sections are organized so to describe the two actuation solutions investigated separately, as well as the structural and aerodynamic equation components. A deepening will be done on the experimental derivation of the aerodynamic model for the novel control actuation architecture proposed. It is organized as follow: in Section 2.1, the mathematical model for a wing flap configuration is derived, described in detail and the equations of motion rewritten in an amenable form for control law development purpose. An entire Subsection is dedicated to

report the free response properties of the proposed aeroelastic system so to identify its stability region. A parametric study is carried out, so to define a new conditions dataset that can serve as benchmark for the verification and validation of the robustness and performance of adaptive control algorithms applied to aeroelastic plant. In Section 2.2 the mathematical model for the novel wing-spoiler designed configuration is presented. The different formulation of the aerodynamic model is obtained and described, leading to the comprehensive aeroelastic equations of motion by coupling it with the same structural model of the wing-flap configuration. Also in this case the free response properties of the dynamic system are analyzed as well as the parametric study for consistency.

2.1 Wing-Flap Configuration

The bi-dimensional pitching/plunging aeroelastic system configuration used in this research as benchmark for adaptive control algorithm testing purpose, is a well assessed configuration, the study of which is due to O'Neil and Strganac at the end of the nineties [56, 57, 58]. After several investigation experimentally examined nonlinear aeroelastic behavior, addressing the effect of freeplay, deadband, and/or piecewise structural nonlinearities [59, 60], more analytical studies have examined continuous structural nonlinearities [61],comparing predictions with measurements for a system with continuous nonlinear stiffness behavior in the pitch mode. Among the outcomes, it was found that the system was experiencing LCO behavior rather then aeroelastic flutter. These LCOs were dependent upon freestream velocity and nonlinear stiffness parameters, both in pitching than in plunging. It was shown for the case of continuous nonlinearities that the LCO behavior possessed harmonic components of the dominant flutter frequency.

Experiments with piecewise stiffness nonlinearities showed an increase in LCO amplitude for increased freestream velocity. Experiments with freeplay nonlinearities showed LCOs at freestream velocities less than the linear flutter velocity. The LCO amplitude grew with an increase in freestream velocity until the flutter occurred at the linear flutter velocity. Further investigations showed two LCO amplitudes that depended upon the initial condition at the same freestream velocity. This LCO centered about an offset from the static equilibrium position. For all these reasons, studying LCOs behaviors of systems like the one reported in Figure 2.1 became a milestone in aeroelastic phenomena analysis and control algorithm testing. O'Neil, Gilliatt and Strganac have the merit to formulate first in [58, 56] the mathematical model of the Figure 2.1 model, and, in collaboration with other authors, the experimental campaign based on the NATA setup validated their theory [62]. They have modeled the aeroelastic system consisting of a wing limited to motion in two degrees of freedom, plunge and pitching, in the

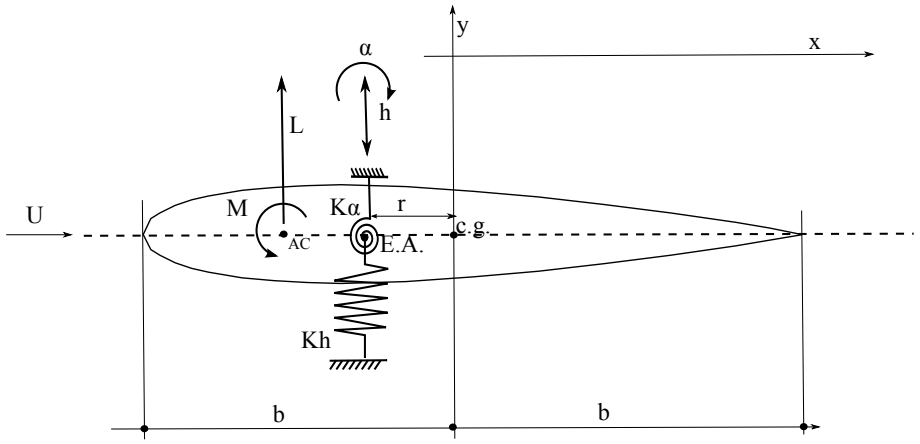

Figure 2.1: 2D Aeroelastic system, modeled by a rigid wing section attached to a flexible support that permits pitch and plunge motion.

successful attempt of reproducing the dynamic behavior obtained with the experimental setup which has been designed with nonlinear spring support to introduce nonlinearities. Tailored experiments established that nonlinear responses, such as limit cycle oscillations, are predicted with the analytical model hereafter reported. The general set of equation, containing the entire set of nonlinearities for sake of generality, follows considering the displacement and velocity of the *c.g.*, with respect to a coordinate system associated with the elastic axis:

$$\bar{r} = r\cos(\alpha+\theta)\hat{i} + [h + r\sin(\alpha+\theta)]\hat{j} \tag{2.1}$$

$$\dot{\bar{r}} = -r\dot{\alpha}\sin(\alpha+\theta)\hat{i} + [\dot{h} + r\dot{\alpha}(\alpha+\theta)]\hat{j} \tag{2.2}$$

Writing the kinetic energy for the system as

$$T = \frac{1}{2}m(\dot{\bar{r}}\cdot\dot{\bar{r}}) + \frac{I_\alpha\dot{\alpha}^2}{2} = \frac{m}{2}[\dot{h}^2 + \dot{\alpha}^2r^2 + 2\dot{h}\dot{\alpha}r\cos(\alpha+\theta)] + \frac{I_\alpha\dot{\alpha}^2}{2} \tag{2.3}$$

where kinetic energy because of planar rotational motion of the rigid wing is included. Higher-order terms because of kinematic nonlinearities are present in the system, and these components are found from (the kinetic energy terms of) Lagranges equations [63] as

$$\frac{\partial\left(\frac{\partial T}{\partial\dot{h}}\right)}{\partial t} = m[\ddot{h} + \ddot{\alpha}r\cos(\alpha+\theta) - \dot{\alpha}^2 r sin(\alpha+\theta)] \tag{2.4}$$

$$\frac{\partial\left(\frac{\partial T}{\partial\dot{\alpha}}\right)}{\partial t} = m[r\ddot{h}\cos(\alpha+\theta) - r\dot{h}\dot{\alpha}\sin(\alpha+\theta) + r^2\ddot{\alpha}] + I_\alpha\ddot{\alpha} \tag{2.5}$$

The equations of motion are derived from these kinetic energy contributions, as well as the potential energy and the work resulting from the internal damping and external aerodynamic forces. The equations of motion are expressed as

$$\begin{aligned} m_T\ddot{h} + m_w r\cos(\alpha+\theta)\ddot{\alpha} - m_w r sin(\alpha+\theta)\dot{\alpha}^2 + c_h\dot{h} \\ +\mu_h g m_T(|\dot{h}|/\dot{h}) + k_h(h+\xi h^3) = -L \end{aligned} \tag{2.6}$$

$$m_w r\cos(\alpha+\theta)\ddot{h} + I_e\ddot{\alpha} + c_\alpha + m\mu_\alpha g r_b(|\dot{\alpha}|/\dot{\alpha}) + k_\alpha(\alpha+\zeta\alpha^3) = M \tag{2.7}$$

where the overdots represent time derivatives, and L and M represent the unsteady aerodynamic lift and moment, respectively. Although θ may be present, it is not used for the studies herein. As will be discussed in the next section, the experiment test apparatus consists of a translating (plunge degree-of-freedom) carriage to which the wing is attached to a rotating (pitch degree-of-freedom) bearing system. Thus, in equations (2.6) and (2.7) m_T denotes the total system mass that translates; m_w denotes the wing mass that rotates; and $I_e = r^2 m_w + I_\alpha$, where I_α is the mass moment of inertia of the wing about its c.g. Both viscous and Coulomb-type damping may be present in the experiments; thus, c_h and c_α terms are included to account for viscous damping forces, and μ_h and μ_α terms are included to account for Coulomb damping forces. Nonlinear stiffness characteristics for pitch and plunge are represented by the parameters ζ and ξ. Higher-order terms, including the centripetal acceleration term $r\dot{\alpha}$ and stiffness nonlinearities, as well as the transcendental terms are retained to capture those sources of dynamic coupling. Typically, these terms are assumed negligible and it is noted that the linear form of equation (2.6) and Eq.(2.7) are identical to the classical pitch and plunge equations found in numerous publications [47, 64]. These equations appear to be uncoupled for the case of $r = 0$; yet, it is important to note that the unsteady aerodynamic loads are dependent upon the motion of the wing, thus,

$$L = L(\dot{h}, \ddot{h}, \alpha, \dot{\alpha}, \ddot{\alpha}, U, \rho, time) \tag{2.8}$$

$$M = M(\dot{h}, \ddot{h}, \alpha, \dot{\alpha}, \ddot{\alpha}, U, \rho, time) \tag{2.9}$$

and, as such, provide an additional source of coupling for the system.

Albeit the model serves to investigate the nonlinear aeroelastic response, the aerodynamic lift and moment is found to be linear (an assumption validated by the experiments discussed in [58]) for the range of motion of the system. Only kinematic and structural nonlinearities are considered first. Thus, a linear unsteady aerodynamic model is appropriate. The aerodynamic lift and moment are modeled by the unsteady aerodynamic theory of

Theodorsen [64]

$$L = \pi\rho b^2(\ddot{h} + U\dot{\alpha} - ba\ddot{\alpha}) + 2\pi\rho UCb(\dot{h} + U\alpha + b(1/2 - \alpha)\dot{\alpha}) \tag{2.10}$$

$$\begin{aligned} M = &-\pi\rho b^3(-a\ddot{h} + (1/2 - a)U\dot{\alpha} + (1/8 - a^2)b\ddot{\alpha}) \\ &+2\pi\rho UCb^2(1/2 + \alpha(\dot{h} + U\alpha + b(1/2 - \alpha))) \end{aligned} \tag{2.11}$$

where C is Theodorsens function that depends on the reduced frequency, $k = b\omega/U$. It is noted that equations (2.10) and (2.11)represent incompressible, small disturbance unsteady flow.

As can be notice in Figure 2.1, the aeroelastic sytem described does not embed any kind of control surface to damp aeroelastic oscillation. This mathematical model has been written, and subsequently built and testes in an experimental apparatus, to investigate how model parameters variation affects the wing flutter properties in terms of LCOs stability region, amplitude and frequencies, as reported in [56, 57, 58]. Figure 2.2is an example of the outcomes from this investigation.

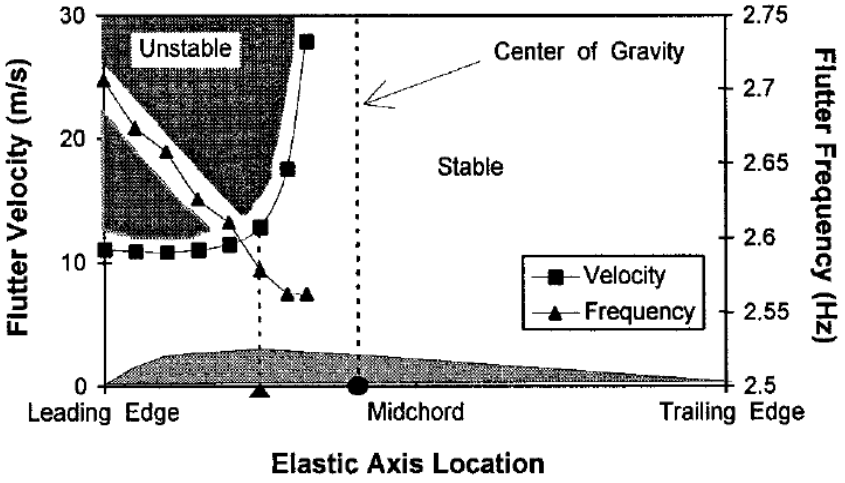

Figure 2.2: Flutter velocities and associated aeroelastic frequencies function of the elastic axis location. Constant stiffness is present [58].

The aeroelastic model described above has unique features and capabilities, since it can incorporate variable location of the elastic axis and various types of stiffness for the pitching and plunging motion. Obviously, the listed parameters, jointly with the freestream velocity value, play a critical roles in the system stability. For these reasons, this type of model has become traditional for the experimental and theoretical analyses of two-dimensional

aeroelastic system behavior. When flutter control is concerned, the system needs to be modified to account for the control surface action. A trailing-edge flap is therefore introduced and considered without mass and stiffness, but only as aerodynamic effect. Consequently, it does not represent an additional degree of freedom for the structural model, which, in fact, continues to be a pitching and plunging 2 DoF aeroelastic system. The schematic of the system changes as in Figure 2.3, which also implies the modification of the aerodynamic equations, accounting for the additional terms introduced.

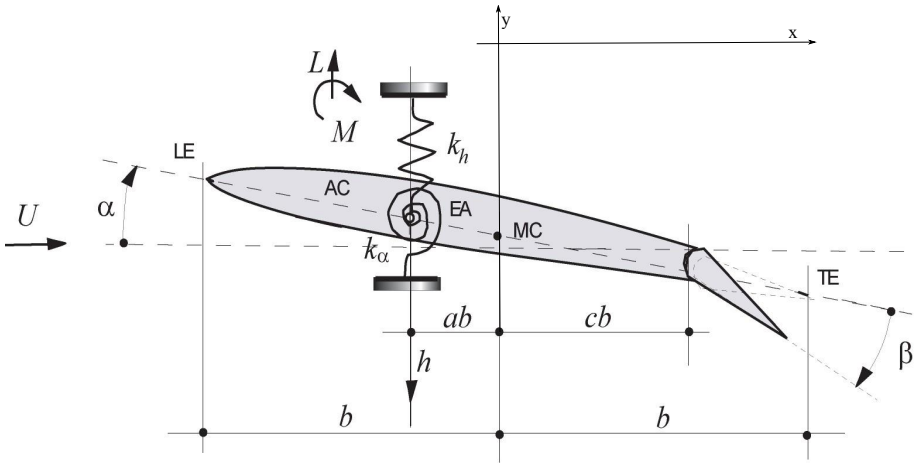

Figure 2.3: 2D Aeroelastic sysytem, wing-flap configuration

From a mathematical point of view is more adequate to express equations (2.6) and (2.7) in a compact form, more suitable for a state-space analysis when control law equations will be written. In addition, a small-perturbations regime is considered in the following analysis, justified by the range of variation of the pitch angle ($\alpha < 10(deg)$) and of the plunge displacement ($h = o(10^{-3})$). This approximation allows to neglect the higher order terms on the model equations, such as $r\dot{\alpha}^2$, ξh^3 and $\zeta\alpha^3$, and to approximate $sin(\alpha) \approx \alpha$ and $cos(\alpha) \approx 1$. It follows that the governing equation of motion of the nonlinear system are derived to be:

$$\begin{bmatrix} m & mx_\alpha b \\ mx_\alpha b & I_\alpha \end{bmatrix} \begin{bmatrix} \ddot{h} \\ \ddot{\alpha} \end{bmatrix} + \begin{bmatrix} c_h & 0 \\ 0 & c_\alpha \end{bmatrix} \begin{bmatrix} \dot{h} \\ \dot{\alpha} \end{bmatrix} + \begin{bmatrix} k_h(h) & 0 \\ 0 & k_\alpha(\alpha) \end{bmatrix} \begin{bmatrix} h \\ \alpha \end{bmatrix} = \begin{bmatrix} -L \\ M \end{bmatrix} \quad (2.12)$$

where all the parameters inside have been already described. What needs to be modified from equations (2.10) and (2.11) is the formulation of the aerodynamic control forces and moment. Assuming a quasi-steady aerodynamic model [47], that fit the small-perturbations assumption and the main purpose of the proposed research of testing adaptive control algorithms, it follows:

$$L = \rho U^2 b C_{L_\alpha}[\alpha + \dot{h}/U + \big(\frac{1}{2} - a\big)b(\dot{\alpha}/U)] + \rho U^2 b C_{L_\beta}\beta \tag{2.13}$$

$$M = \rho U^2 b^2 C_{m_\alpha}[\alpha + \dot{h}/U + \big(\frac{1}{2} - a\big)b(\dot{\alpha}/U)] + \rho U^2 b^2 C_{m_\beta}\beta \tag{2.14}$$

where C_{L_α} and C_{m_α} are the wing lift and moment coefficients per angle of attack, whereas C_{L_β} and C_{m_β} are the lift and moment coefficient per control surface deflection, β indeed. The relatively simple choice done on the description of the aerodynamic forces, adopting the quasi-steady aerodynamic, is justified by the main objective of the theoretical development reported in the present dissertation, that is the closed-loop performance analysis of model reference adaptive control algorithms, rather than a pure aerodynamic analysis. Furthermore, the proposed aeroelastic model refers to an experiments of which the reduced frequency associated validates the use of the quasi-steady model, [65, 66]. Several classes of nonlinear stiffness contributions such as $k_\alpha(\alpha)$ and $k_h(h)$ can be analyzed to modify the open-loop dynamics of aeroelastic systems. A general way, commonly used to express structural nonlinearities, is the polynomial formulation, where pitching and plunging stiffness might be expressed as follows:

$$k_\alpha(\alpha) = k_{\alpha_0} + k_{\alpha_1}\alpha + k_{\alpha_2}\alpha^2 + k_{\alpha_3}\alpha^3 + k_{\alpha_4}\alpha^4 \cdots$$

$$k_h(h) = k_{h_0} + k_{h_1}h + k_{h_2}h^2 + k_{h_3}h^3 + k_{h_4}h^4 \cdots \tag{2.15}$$

Equations (2.1) and (2.15), are only a general polynomial formulation where the presence of odd-terms can lead to think to an incorrect non-symmetric stiffness representation. However, these terms have been added to emphasize that the spring coefficients obtained from measured data fitting, as for the model under analysis, may actually be non-symmetric. In the proposed model, the plunge stiffness will be constant and the pitching stiffness will be a fifth order polynomial. Combining Eq.(2.12) with equations (2.13) and (2.14), the following can be obtained:

$$\begin{bmatrix} m & mx_\alpha b \\ mx_\alpha b & I_\alpha \end{bmatrix}\begin{bmatrix} \ddot{h} \\ \ddot{\alpha} \end{bmatrix} + \begin{bmatrix} c_h + \rho U b C_{L_\alpha} & \rho U b^2 C_{L_\alpha}(1/2 - a) \\ \rho U b^2 C_{m_\alpha} & c_\alpha - \rho U b^3 C_{m_\alpha}(1/2 - a) \end{bmatrix}\begin{bmatrix} \dot{h} \\ \dot{\alpha} \end{bmatrix} + \begin{bmatrix} k_h(h) & \rho U^2 b C_{L_\alpha} \\ 0 & -\rho U^2 b^2 C_{m_\alpha} + k_\alpha(\alpha) \end{bmatrix}\begin{bmatrix} h \\ \alpha \end{bmatrix} = \begin{bmatrix} -\rho b C_{L_\beta} \\ \rho b^2 C_{m_\beta} \end{bmatrix} U^2 \beta \tag{2.16}$$

For the analyses to follow, it is useful to convert this equation into a state-space formulation, where the state variable vector as

$$\bar{x} = \begin{bmatrix} x_1 \\ x_2 \\ x_3 \\ x_4 \end{bmatrix} = \begin{bmatrix} h \\ \alpha \\ \dot{h} \\ \dot{\alpha} \end{bmatrix} \tag{2.17}$$

The forthcoming transformed equations of motion become:

$$\dot{\bar{x}} = f_\mu(\bar{x}) + g(\bar{x})U^2\beta \tag{2.18}$$

where

$$f_\mu = \begin{bmatrix} x_3 \\ x_4 \\ -k_1x_1 - [k_2U^2 + p(x_2)]x_2 - c_1x_3 - c_2x_4 \\ -k_3x_1 - [k_4U^2 + q(x_2)]x_2 - c_3x_3 - c_4x_4 \end{bmatrix} \tag{2.19}$$

$$g(x) = \begin{bmatrix} 0 \\ 0 \\ g_3 \\ g_4 \end{bmatrix} \tag{2.20}$$

The simplified form takes advantage of several auxiliary variables defined in Table 2.1. It is worth to be noticed, how the equations of motion parametric dependency on the freestream velocity U and also on the elastic axis location a, is gather and highlighted in the conventional notation$f_\mu(x)$, Eq.(2.19) . Strictly speaking, the subscript μ should be replaced by the vector of the parameters $[U \quad a]$. However, in this occasion the simpler notation is adopted, keeping in mind that the solutions are in fact a two-parameter family of solutions.
For control robustness evaluation purpose, the aeroelastic system is modified to account for external aerodynamic forces and moments due to gust application. The right hand side of Equation (2.12) is modified as follows:

$$\begin{bmatrix} m & mx_\alpha b \\ mx_\alpha b & I_\alpha \end{bmatrix} \begin{bmatrix} \ddot{h} \\ \ddot{\alpha} \end{bmatrix} + \begin{bmatrix} c_h & 0 \\ 0 & c_\alpha \end{bmatrix} \begin{bmatrix} \dot{h} \\ \dot{\alpha} \end{bmatrix} + \begin{bmatrix} k_h(h) & 0 \\ 0 & k_\alpha(\alpha) \end{bmatrix} \begin{bmatrix} h \\ \alpha \end{bmatrix} = \begin{bmatrix} -L - L_g \\ M + M_g \end{bmatrix} \tag{2.21}$$

where the lift and moment gust component summed up with their proper sign are expressed as:

$$L_g = \rho U^2 b C_{L_\alpha} w_g(\tau)/U = \rho U b C_{L_\alpha} w_g(\tau) \tag{2.22}$$

$$M_g = (0.5 - a) b L_g \tag{2.23}$$

Table 2.1: System Variables. Wing-Flap Configuration

Parameter	Definition
d	$m(I_\alpha - mx_\alpha^2)b^2$
k_1	$I_\alpha k_h/d$
k_2	$(I_\alpha \rho b C_{L_\alpha} + mx_\alpha b^3 \rho C_{m_\alpha})/d$
k_3	$-mx_\alpha b k_h/d$
k_4	$(-mx_\alpha b^2 \rho C_{L_\alpha} - m\rho b^2 C_{m_\alpha})/d$
$p(x_2)$	$(-mx_\alpha b/d)k_\alpha(x_2)$
$q(x_2)$	$(m/d)k_\alpha(x_2)$
c_1	$[I_\alpha(c_h + \rho U b C_{L_\alpha}) + mx_\alpha \rho U b^3 C_{m_\alpha}]/d$
c_2	$[I_\alpha \rho U b^2 C_{L_\alpha}(1/2 - a) - mx_\alpha b c_\alpha + mx_\alpha \rho U b^4 C_{m_\alpha}(1/2 - a)]/d$
c_3	$(-mx_\alpha b c_h - mx_\alpha \rho U b^2 C_{L_\alpha} - m\rho U b^2 C_{m_\alpha})/d$
c_4	$[mc_\alpha - mx_\alpha \rho U b^3 C_{L_\alpha}(1/2 - a) - m\rho U b^3 C_{m_\alpha}(1/2 - a)]/d$
g_3	$(1/d)(-I_\alpha b \rho C_{L_\beta} + mx_\alpha \rho b^3 C_{m_\beta})$
g_4	$(1/d)(mx_\alpha b^2 \rho C_{L_\beta} + m\rho b^2 C_{m_\beta})$

and $w_g(\tau)$ denotes the disturbance velocity while τ is a dimensionless time variable defined as $\tau = Ut/b$. The three different type of gust, applied to the proposed model, are described in detail in section 2.2.3, and results shown in section 4.2.

2.1.1 Nonlinear Aeroelastic System Properties: Wing-Flap Model

The mathematical models, used in the present research to describe the aeroelastic system dynamics and to test model reference adaptive control algorithms robustness and performance, are those reported in Equation (2.12) and Equation (2.21) in presence of gust. The dynamic properties of the two-dimensional aeroelastic plant, reported in Figure 2.3, depend on the structural parameters that, in this research, were set as in Table 2.4, [65, 76]. In detail: a is the dimensionless distance from the midchord to the elastic axis; b is the semichord of the wing; C_{L_α} and C_{m_α} are respectively lift and moment curve slopes per angle of attack; C_{L_β} and C_{m_β} are respectively lift and moment curve slopes per control surface deflection; x_α is the distance from elastic axis to the center of gravity, made dimensionless being divided by the semichord and positive rearward, since the reference frame is considered as in Figure 2.3; the couples k_h, k_α and c_h, c_α are respectively the stiffness and damping plunging/pitching coefficients of the system, all constants exception done for the continuous nonlinear restoring moment in

Table 2.2: Free Response Analysis: Plant without Failure

	Case (a)	**Case (b)**	**Case (c)**	**Case (d)**
$\bar{x}(0)$	$[0, 0.1, 0, 0]$	$[0, 0.1, 0, 0]$	$[0, 0.1, 0, 0]$	$[0, 0.1, 0, 0]$
Stiffness	K_{nom}	K_{nom}	K_{nom}	K_{nom}
Wind Speed	$5(m/s)$	$7(m/s)$	$9(m/s)$	$15(m/s)$
Response	Damped	LCO	LCO	Divergent
Proper Freq.	—	$2.93(Hz)$	$3.418(Hz)$	—
Pitch Amp.	—	$5.91(deg)$	$7.79(deg)$	—
Plunge Amp.	—	$2.13e^{-3}(m)$	$2.56e^{-3}(m)$	—
Condition Name	Pre-Flutter	Flutter	Post-Flutter	Divergence

the pitch degree of freedom, of τ_i are the coefficients of the polynomial formulation; ρ is the air density, m_w is the wing gross weight, in this application considered equal to the total mass m_T; and finally I_α is the torsional moment of inertia. Such continuous nonlinear models for stiffness result from a thin wing or propeller being subjected to large torsional amplitudes [1, 67]. Considering the settings chosen, in particular the nonlinearity in torsional stiffness, it does not surprise that the system shows an LCO dynamic behavior passed a certain wind speed, commonly interpreted as flutter for nonlinear systems, from the scientific community. For this reason, *flutter* subscription will be used to indicate the critical wind speed at which LCOs' can be firstly appreciated. Any dynamic response happening at higher or lower wind speed will be indicated as *post-flutter* and *pre-flutter* conditions respectively. With this settings the aeroelastic plant shows a LCO behavior at the critical wind speed $U_{flutter} = 7(m/s)$ in nominal condition. The oscillatory response is obtained by exciting the system with an initial pitch angle state perturbation of 0.1 radians, $\bar{x} = [h \quad \alpha \quad \dot{h} \quad \dot{\alpha}] = [0 \quad 0.1 \quad 0 \quad 0]$. Figure 2.4 and Figure 2.5 demonstrate how for slower wind speed the behavior is damped. Then there is a range of speed in which the LCO oscillations are maintained with amplitude increasing proportionally with the wind speed. Finally, divergent behavior is reached at wind speed of $U = 15(m/s)$. It must be pointed out that in Figure 2.4 (d) and Figure 2.5 (d) the divergence is difficult to appreciate because it occurs slowly and the axes scale hide the trend somewhat. The same behavior is observable both in pitch and plunge degree of freedom. The analyzed cases and the resulting dynamic response of the proposed nonlinear aeroelastic system are summarized and reported in Table 2.2. It must be pointed out that the proper frequencies and pitching/plunging amplitudes are uniquely identifiable, and so reported, only when the dynamic response exhibits LCOs, *case (b)* and *case (c)*.

In line with the main purpose of this work, that is the adaptive control algorithm robustness testing and validation, particular attention is given

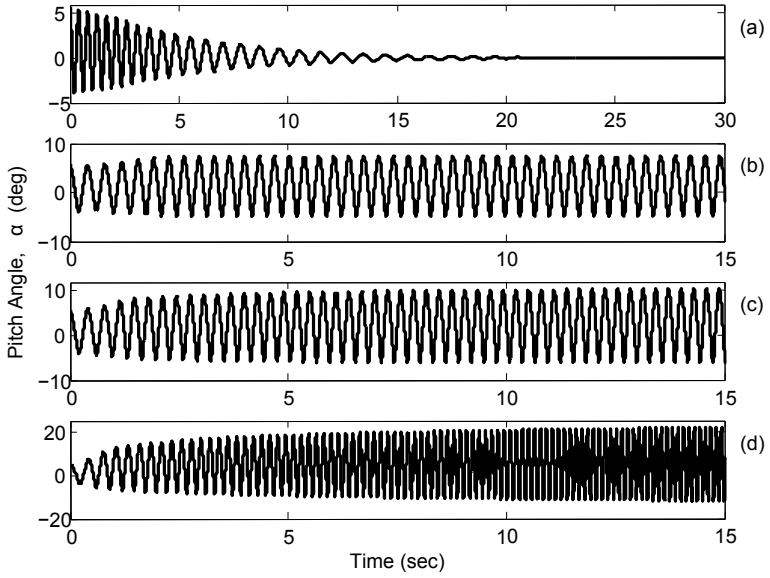

Figure 2.4: Aeroelastic System Free Response, pitch angle time histories: (a) at $U = 5(m/s) < U_{flutter}$; (b) at $U = 7(m/s) = U_{flutter}$, (c) LCO at $U = 9(m/s) > U_{flutter}$, (d) divergence at $U = 15(m/s) > U_{flutter}$.

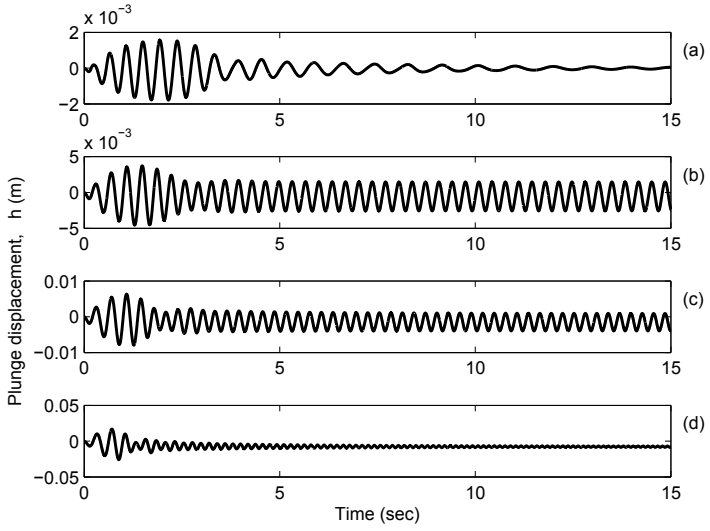

Figure 2.5: Aeroelastic System Free Response, plunge displacement time histories: (a) at $U = 5(m/s) < U_{flutter}$; (b) at $U = 7(m/s) = U_{flutter}$, (c) LCO at $U = 9(m/s) > U_{flutter}$, (d) divergence at $U = 15(m/s) > U_{flutter}$.

Table 2.3: Free Response Analysis: Plant with Failure

	Case (a)	**Case (b)**	**Case (c)**	**Case (d)**
$\bar{x}(0)$	$[0, 0.1, 0, 0]$	$[0, 0.1, 0, 0]$	$[0, 0.1, 0, 0]$	$[0, 0.1, 0, 0]$
Stiffness	K_{red}	K_{red}	K_{red}	K_{red}
Wind Speed	$3(m/s)$	$5(m/s)$	$7(m/s)$	$15(m/s)$
Response	Damped	LCO	LCO	Divergent
Proper Freq.	—	$1.92(Hz)$	$2.29(Hz)$	—
Pitch Amp.	—	$6.27(deg)$	$9.16(deg)$	—
Plunge Amp.	—	$2.53e^{-3}(m)$	$5.26e^{-3}(m)$	—
Condition Name	Pre-Flutter	Flutter	Post-Flutter	Divergence

to the off-design condition of the plant. Hence, the dynamic response of the plant has been analyzed in also under failure condition. Figure 2.6 and Figure 2.7 demostrate how a reduction of the stiffness matrix by 50%, $K_{reduced} = K_{nominal}/2$, simulating an unpredictable wing structure failure, affects the dynamic response of the system. A drift down to lower values of the significant wind speed, at which flutter occurs, can be clearly noticed from the recorded time histories. In particular, $U_{flutter}$ drops down to $5(m/s)$. The analyzed cases and the resulting dynamic response of the proposed nonlinear aeroelastic system with simulated failure are summarized and reported in Table 2.3.

In addiction, the phase diagram and the power spectra, reported in Figure 2.8 and Figure 2.9 respectively, demonstrate how the analyzed off-design conditions, *post-flutter* and *failure*, affect the proper system frequency and the correlation between the states and their derivatives. This latter evidence remark the necessity to use adaptive control scheme for this type of complex problem.

The trust region of the quasi-steady aerodynamic model stays within a range of angle of attack up to 10 degrees. For this reason, the wind speed increment and the structural failures applied to the plant are modulated so that the resulting LCOs motion is bounded inside the valid angle of attack domain. In particular, failure is simulated by a 50% reduction of the stiffness matrix K nominal value and the post-flutter velocity is 30% higher the flutter speed, $U_{post-flutter} = 9m/s$.

2.1.1.1 Parametric Analysis of the Linearized System

The aeroelastic system described is function of several parameters which affect its stability and dynamic properties. For a better understanding of the correlations between the system dynamic properties and its parameters variation, and to justify the choice of such parameters' values, a *Root-Locus* analysis has been carried out and hereafter reported for sake of complete-

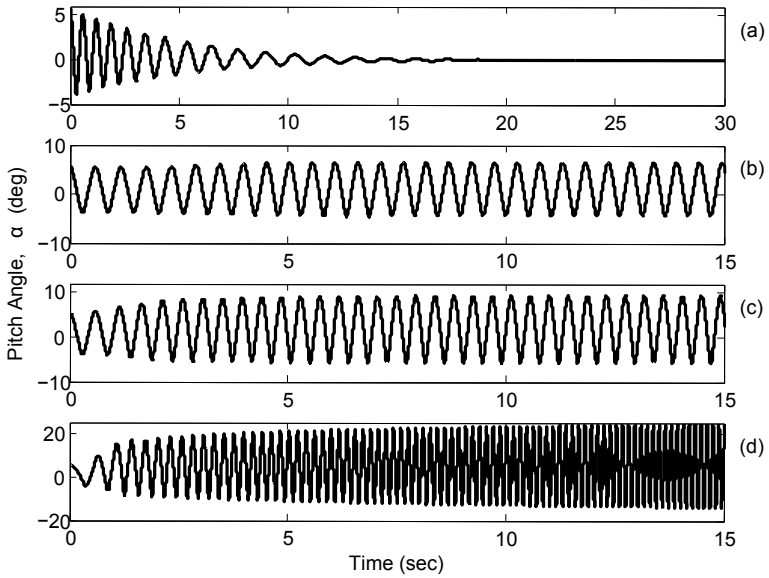

Figure 2.6: Aeroelastic System Free Response with simulated failure, pitch angle time histories: (a) at $U = 3(m/s) < U_{flutter}$; (b) at $U = 5(m/s) = U_{flutter}$, (c) LCO at $U = 7(m/s) > U_{flutter}$, divergence at $U = 15(m/s) > U_{flutter}$.

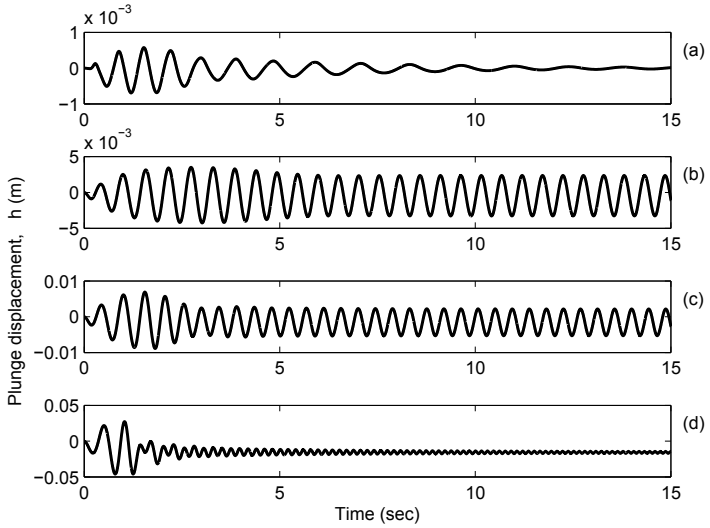

Figure 2.7: Aeroelastic System Free Response with simulated failure, plunge displacement time histories: (a) at $U = 3(m/s) < U_{flutter}$; (b) at $U = 5(m/s) = U_{flutter}$, (c) LCO at $U = 7(m/s) > U_{flutter}$, divergence at $U = 15(m/s) > U_{flutter}$.

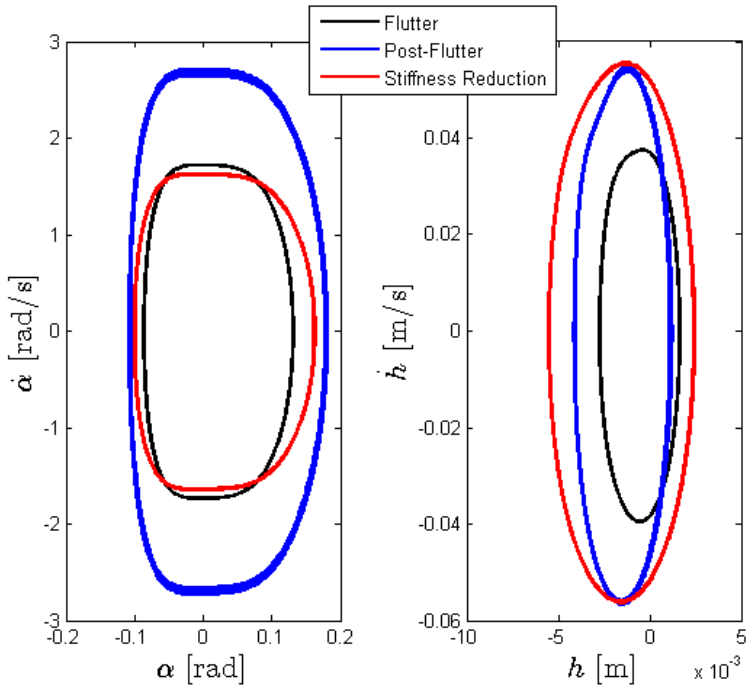

Figure 2.8: Aeroelastic system phase diagram comparison.

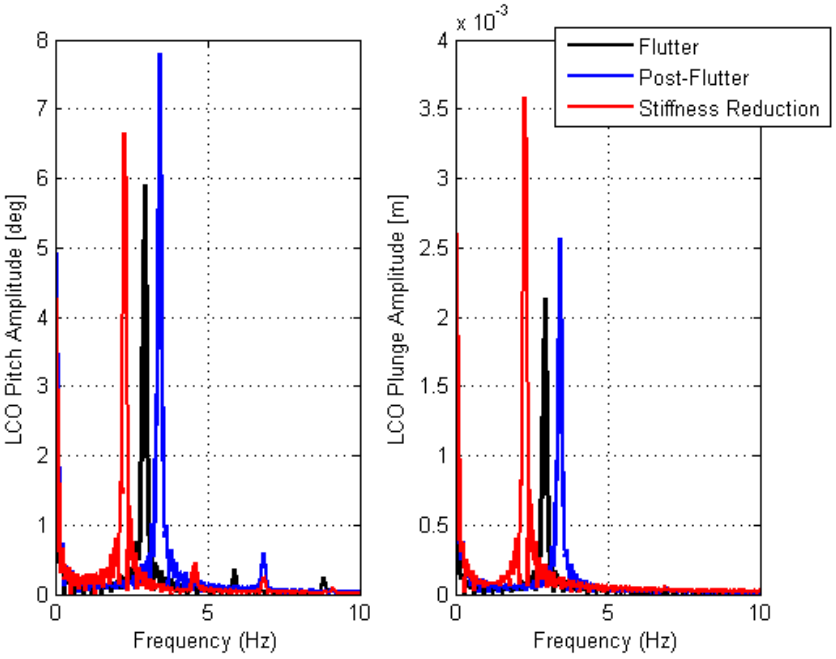

Figure 2.9: Aeroelastic system power spectra comparison.

Table 2.4: 2D Aeroelastic Plant Parameters

Parameter	**Definition**
a	-0.4
b	$0.135(m)$
C_{L_α}	6.28
C_{m_α}	$(\frac{1}{2} - a)C_{L_\alpha}$
C_{L_β}	3.35
C_{m_β}	-0.635
x_α	$[0.0873 - (b + ab)]/b$
k_α	$\sum_{i=1}^{5} \tau_i \alpha^{i-1}$
k_h	$2844.4(N \cdot m^{-1})$
ρ	$1.225(Kg/m^3)$
$m_w = m_T$	$12.387(Kg)$
τ_i	$[2.8 - 32.3 \quad 3,709.7 - 24,195.6 \quad 48,756.9]^T$
I_α	$0.065(Kg \cdot m^2)$
c_α	$0.036(N \cdot sec)$
c_h	$27.43(N \cdot m^{-1} \cdot sec^{-1})$

ness. Albeit the system is structurally nonlinear in α, fourth order polynomial stiffness in pitching, the zero-poles analysis of the linearized system, around an equilibrium condition, returns important information about the uncontrolled dynamic behavior (proper frequency range and damping) and its controllability in closed-loop (i.e. the system plant must be non-minimum phase for model reference adaptive control stability). In addiction, the state-space formulation of the plant well suites the root-loci technique. First, it must be pointed out that, since the mathematical model under analysis reproduces an aeroelastic experimental apparatus, designed and built up to obtain LCO's at low speed, the usual path of the roots [68], representative of the bending and torsional modes, will not be displayed. In fact, the two modes, usually represented by two real roots on the stable half-plane of the complex plane when below flutter speed condition, then coalesce in one single couple of conjugate complex roots, which is characteristic of a damped harmonic motion if in the left hand side of the Argand plane (negative real part), of stable, self-sustained, with a single frequency and constant amplitude LCO if $Re(\lambda_i) = 0$, and of divergent oscillations for positive real part of the eigenvalues. Because of the scientific purpose for which this aeroelastic system model has been conceived the two modes are always coupled. Consequently, the entire set of root-loci analyzed always reports a couple of conjugate complex poles, which move in function of the parame-

ters' variation imposed for analysis purpose. As shown in Figure 2.10a, the nonlinearity in the pitch degree of freedom, as in Table 2.4, affects significantly the two conjugated poles location, making the system dynamic stable or not, in function of the initial condition on which the system is linearized. In particular, in Figure 2.10a, the initial AoA is made variable between 0 and $0.1(rad)$, with step of $\Delta\alpha = 0.005(rad)$. Three different region can be identified from the poles path observation: an initial stability region from $\alpha = 0$ to $alpha = 0.06(deg)$; an unstable region within 0.06 and 0.08 of the α range; and then another stability region at higher frequency for higher α. Since $\alpha = 0.1(rad)$ is the usual perturbation imposed to excite the system to LCOs throughout the whole study, and being interested at this moment to the effect of the other parameter on the system dynamics, the initial condition of $alpha = 0.1(rad)$ is chosen as linearization point to pursue the analysis. Figure 2.10b shows the effect of the wind speed U on the aeroelastic system. As expected, increasing the wind speed the system switches from a damped stable oscillation regime to a divergent behavior, meeting stable flutter condition at the imaginary axis crossing point. In particular U is made variable from 5 to 11 (m/s) at step of $\Delta U = 1(m/s)$, crossing the Im axis at about 8.5 (m/s). This value is fairly different from the nonlinear plant stable LCO condition because of the linear approximation, which indeed can not be used for control algorithm design purpose. However, it is worth to notice that the effect of the parameter in the linearized model are exactly the same of the nonlinear model ones, with only slight approximation on the numerical values. Figure 2.12 shows the combined effect of the elastic axis variation with the wind speed increment. In this case the wind speed variation acts emphasizing the a location effect, enlarging the poles path that it causes. As can be noticed from the graph there is a unique location of minimum stability margin, otherwise instability is met, while all the other a locations cause a motion of the poles leftwards in the complex plane. In particular causing, higher frequency - less damping oscillation for closer E.A. to the c.g., and lower frequency - higher damping for further position of E.A. with respect to the c.g. location. In the linear approximation a is made variable from 0.2 to -0.4 at step of -0.1. Figure 2.12 shows the effect on the system roots of a simulated failure by means of a percentage reduction of the stiffness matrix. Figure 2.12a depicts the poles path for K reduction solely, whereas Figure 2.12b depicts the combined effect of simultaneous U increment and K reduction. In the reported investigation, the stiffness matrix is made variable from a nominal value k reported in Table 2.4 to a $K_{reduced} = 0.2K_{nom}$, reducing it by step of 10%, driving the roots rightwards to the unstable half-plane. The roots are strongly modified both in proper frequency and damping, despite the slight change in frequency produced by the wind speed variation. The combined effect of the two parameters' variation has a significant impact on the properties of the system, so to be considered of paramount importance for adaptive control algorithm

robustness testing in the rest of the performed research.

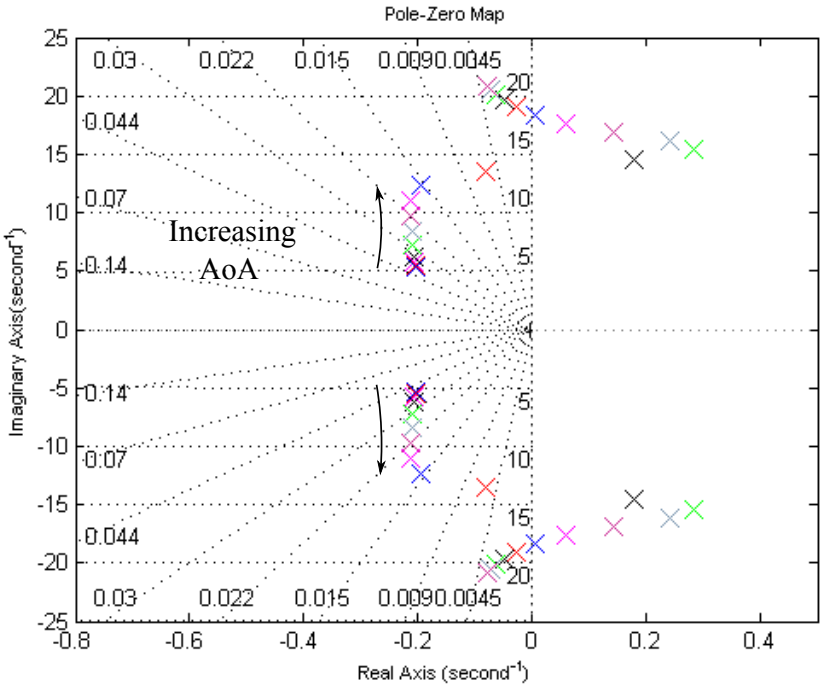

(a) $\alpha(0)$ Initial condition effect

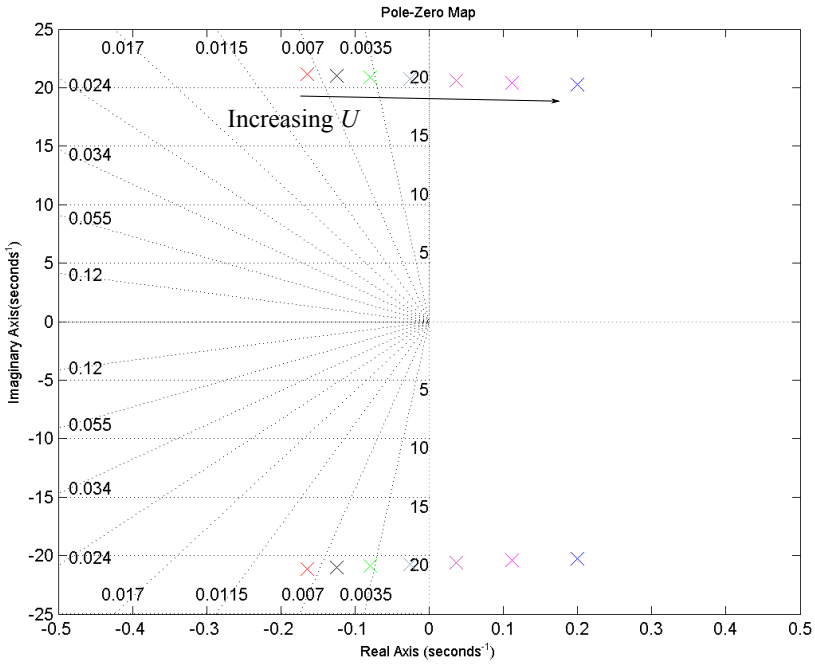

(b) U variation effect

Figure 2.10: Root-loci parametric analysis results

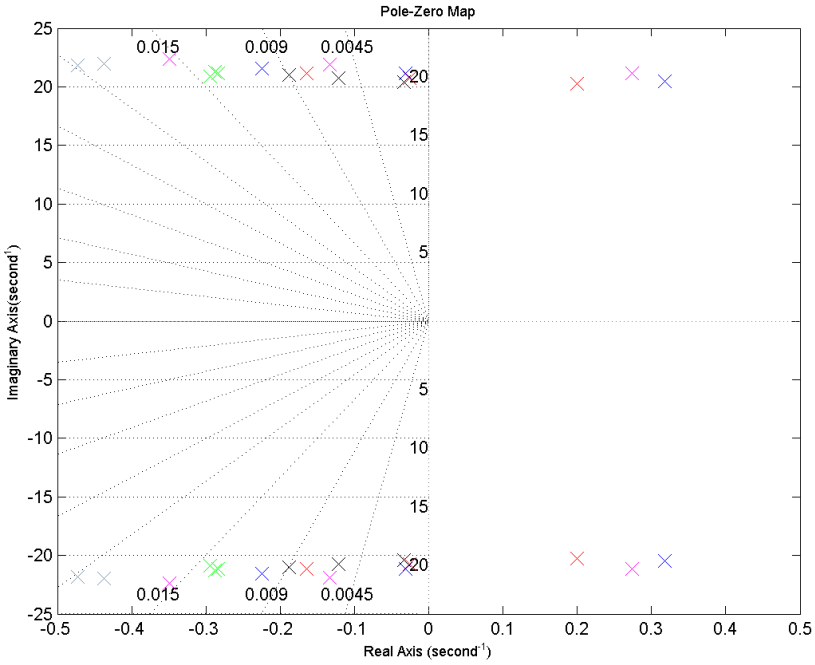

(a) a and U variation effect

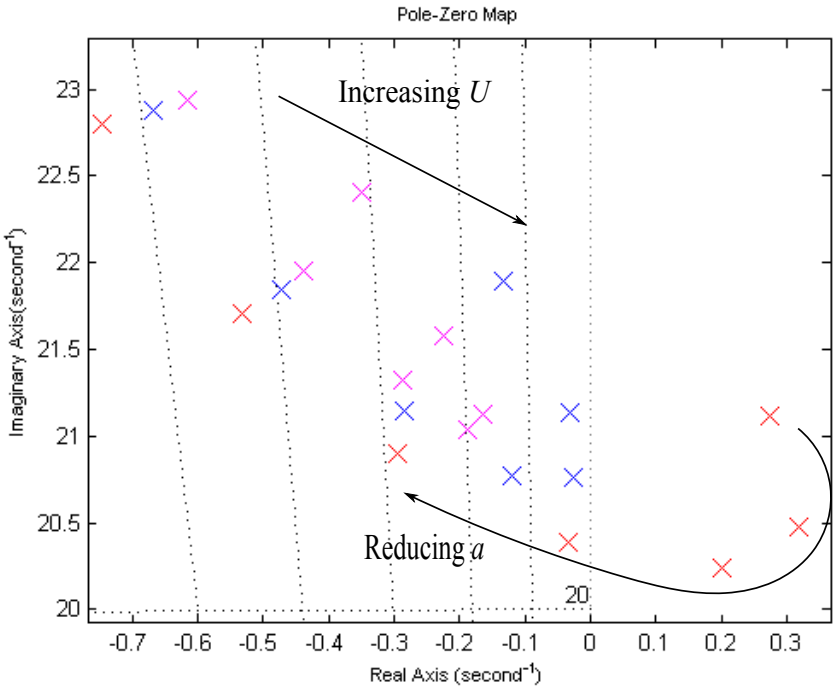

(b) a and U variation effect, magnified

Figure 2.11: Root-loci parametric analysis results

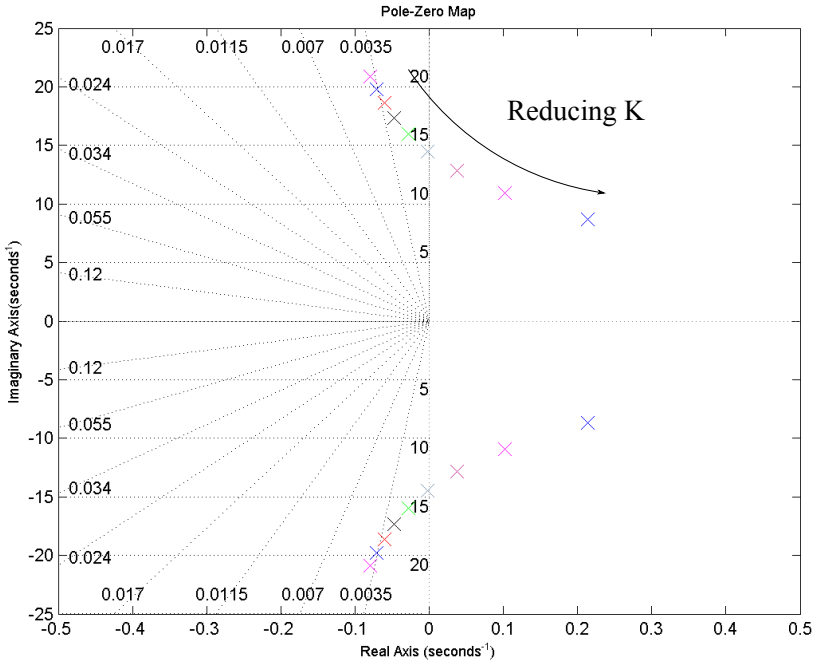

(a) Stiffness variation effect

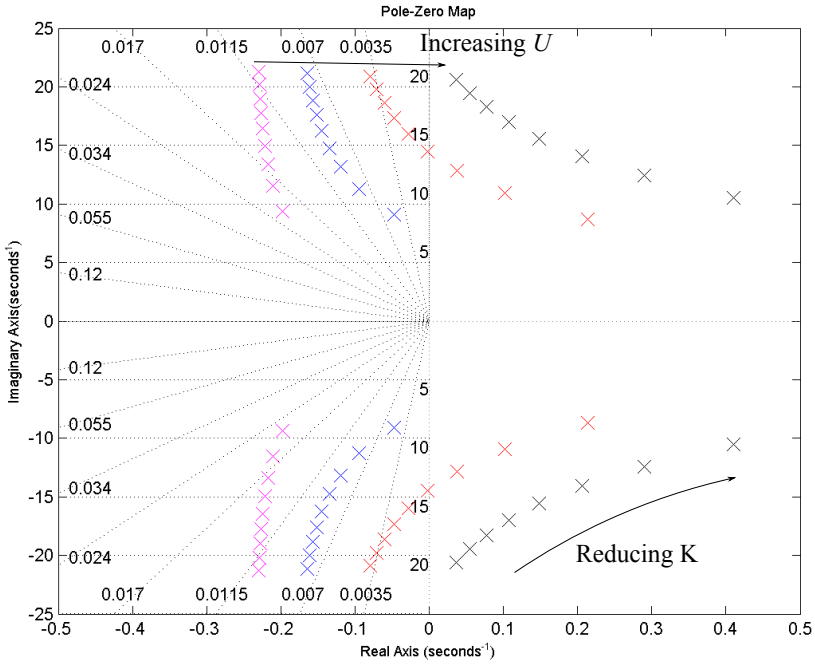

(b) K and U variation

Figure 2.12: Root-loci parametric analysis results

2.2 Wing-Spoiler Configuration

Despite scientific aerospace literature of the last decade is densely populated by several active control algorithm applications to aeroelastic dynamic systems, as reported in Chapter 1, most of them rely on standard control surface configuration as single trailing edge flap configuration or double leading/trailing edge flap configuration. Different research teams have proposed different control laws and architectures, designed and tested both numerically, in simulation environment, and experimentally, with wind tunnel trials or flight-testing. In [69, 70, 71], the authors developed and tested their control algorithms for the Benchmark Active Control Technology (BACT) Wind-Tunnel Model, while in [72, 73, 74], the authors designed and tested their control laws for the Nonlinear Aeroelastic Testbed Apparatus (NATA) [10] at Texas AM University. The control systems developed, including the most recent neural network [75], adaptive back-stepping [76] and L_1 adaptive controller [10], have been applied to wing models, in simulation or experimental setup, with either a single trailing edge control surface or a combination of leading and trailing edge control surfaces [77]. However, some issues related to these classic solutions can be highlighted, such as trailing edge flap saturation, being the flap displacement usually constrained between +/- 10 degrees, and leading edge slat actuation system complexity. In this research, a particular attention has been given to the proposal, and investigation of the effectiveness of an original control architecture, which might represent a possible alternative or redundant solution to the standard control surface architecture and to possibly resolve the previous mentioned issues.The proposed novel architecture takes advantage of studies on spoiler effect on flutter [78], and considers multiple distributed spoilers working collectively, with predefined opening strategies. Moreover, previous survey on flow control by hydrodynamics Helmholtz resonators [79], pointed out the efficacy of leading edge solution in controlling the flow field across the airfoil. Based on these findings the trailing-edge spoiler configuration has been investigated as a possible solution for flutter control purpose. The spoilers design optimization has been performed by CFD, while a combination of experimental and simulation investigations have been used to validate the configuration properties and to define the best actuation strategy, as explained in detail in Chapter 5, which the reader is invited to read before the current section, for a full comprehension purpose. Specifically, a novel coordinated multiple spoiler actuation strategy is evaluated for flutter suppression, which to the best of the author knowledge, was not attempted before. The nonlinear aerodynamic database, experimentally obtained, is coupled with the nonlinear plunging/pitching structural model described in section 2.1. The implemented model, so designed and built, exhibits a supercritical Hopf-bifurcation behavior that is a stable Limit Cycle Oscillations (LCOs) past the flutter speed $U_{flutter} = 7.5(m/s)$.

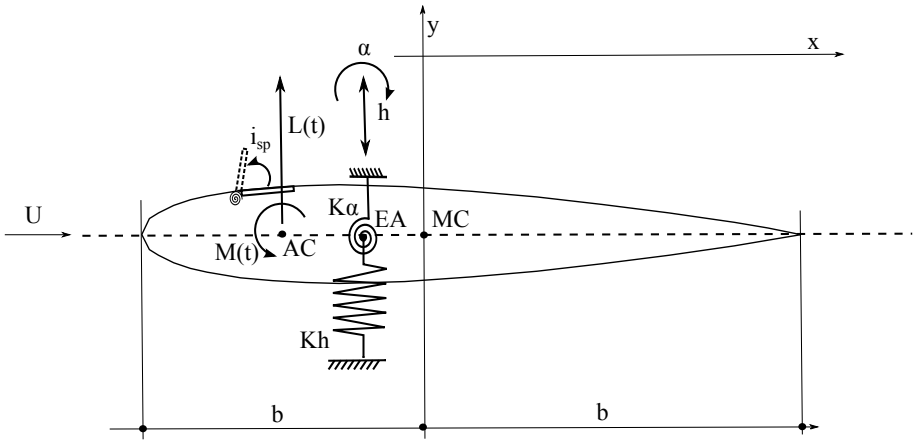

Figure 2.13: Wing-Spoiler configuration, 2D aeroelastic system schematic.

2.2.1 Aerodynamic Mathematical Model

Once manufactured and tested, the wing-spoiler configuration aerodynamic data, collected by means of the six axes force balance, has been used to build up the aerodynamic model suitable to be coupled with the structural model described in section 2.1, so to implement the novel aeroelastic dynamic system to be controlled by active and adaptive control algorithms and obtain results on the overall architecture efficacy.

The schematic view of the aeroelastic configuration described is reported in Figure 2.13, where the i_{sp} parameter is the number of active spoiler. As explained afterward, the deduction and incremental values of lift and pitching moment are functionally related to the i_{sp} parameter and the spoiler effectiveness factor (k_{sp}), which takes into account the selected spoiler opening sequence. Additionally, it should be noticed that the actuator working frequencies are one order of magnitude faster than the aeroelastic properties of the model analyzed and for this reason the actuator dynamics will be neglected in the model dynamic equations. As an existing wing section experimental test article is used, it was chosen not to describe the aerodynamic force and moment by any preexisting analytical unsteady or quasi-steady form, as in [64, 80], but rather, using an approach common in flight simulation [81], by the use of an aerodynamic database experimentally obtained by wind tunnel testing. This approach allows the nonlinearities, given by stall and the actual contribution of the spoiler activation strategy to the aerodynamic loads, to be included into the model formulation. The equations describing the aeroelastic model of Figure 2.13 are the same of the wing-trailing edge flap configuration, Section 2.1 equation 2.12, exception done for the formulation of the external aerodynamic forces' contributions. These latter are written as a function of the lift and pitching aerodynamic moment coefficients and are written by the classical formulation per unit of

length:

$$\begin{aligned} L &= \rho U^2 b C_L(\alpha, Re, i_{sp}, w_G(\tau)) \\ M &= \rho U^2 b^2 C_m(\alpha, Re, i_{sp}, w_G(\tau)) \end{aligned} \tag{2.24}$$

The experimental aerodynamic coefficients are reported in Figure 2.14, Figure 2.15 and Figure 2.16. The measured AoA domain is 18 deg. In all these figures, the lines represent configurations going from 0 (clean) up to all 5 spoiler active. As it can be noticed, according to this approach, nonlinear stall region of the wing and the nonlinear effect of the spoiler activation are implicitly included in the formulation. The wing section in post-flutter conditions exhibits LCOs, hence it is assumed that the aerodynamic angle of attack used to interpolate the data can be written as:

$$\alpha = \big[\theta + \frac{\dot{h}}{U}(\frac{1}{2} - a)b\big(\frac{\dot{\theta}}{U}\big)\big] \tag{2.25}$$

where θ is the geometrical static pitch angle, and the contributions of the plunge and pitching velocities are taken into account. The analytical expressions of the lift and aerodynamic moment factoring the experimentally evaluated coefficients are:

$$\begin{aligned} L &= \rho U^2 b C_{L_\alpha}\big[\theta + \frac{\dot{h}}{U}(\frac{1}{2} - a)b\big(\frac{\dot{\theta}}{U}\big)\big] - \rho U^2 b \Delta C_{L_{sp}} \\ M &= \rho U^2 b^2 C_{m_\alpha}\big[\theta + \frac{\dot{h}}{U}(\frac{1}{2} - a)b\big(\frac{\dot{\theta}}{U}\big)\big] - \rho U^2 b^2 \Delta C_{m_{sp}} \end{aligned} \tag{2.26}$$

Herein, the contribution to lift and pitching aerodynamic moment of the spoiler is written as a function of the wing angle of attack, flight speed and number of spoiler opened. The general formulation describing the spoiler effect on lift coefficient is:

$$\Delta C_{L_{isp}} = \sum_{i=\#sp} \big(k_{\delta_{sp}}\big)_i \big(\Delta C_{L_{isp}}(\alpha)\big)_{\delta_{max}} \cdot \frac{(C_L)_M}{(C_L)_{M=0}} \big(\frac{L_E}{L_R}\big)_{i_{sp}} \tag{2.27}$$

where $\big(k_{\delta_{sp}}\big)$ is the single spoiler lift effectiveness factor, $\big(\Delta C_{L_{isp}}(\alpha)_{\delta_{max}}$ is the single spoiler lift increment at maximum deflection for given AoA, $\frac{(C_L)_M}{(C_L)_{M=0}}$ accounts for the compressibility, $\big(\frac{L_E}{L_R}\big)_{sp}$ accounts for the flexibility of the wing section. The summation is extended to the number of operating spoiler panels, $\#sp$. In the prototyped wing configuration the spoiler works in a binary on/off mode, with maximum and unique deflection allowed at $85(deg)$. The airflow is incompressible and the wing properties are lumped in a single 2D section, which is by rigid definition. Therefore, equation 2.27 reduces to

$$\Delta C_{L_{i_{sp}}} = \sum_{i=\#sp} \left(k_{\delta_{sp}}\right)_i \left(\Delta C_{L_{i_{sp}}}(\alpha)\right)_{\delta_{max}} \tag{2.28}$$

Analogous considerations are applied to the pitching moment coefficient, which final equation has exactly the same form:

$$\Delta C_{m_{i_{sp}}} = \sum_{i=\#sp} \left(k_{\delta_{sp}}\right)_i \left(\Delta C_{m_{i_{sp}}}(\alpha)\right)_{\delta_{max}} \tag{2.29}$$

The nonlinear trend of the spoiler aerodynamic increments is attributed to the nonlinearity of the effectiveness factor, which varies with the number of the open spoilers, their location and consequently with the predefined opening strategy.

2.2.2 Aeroelastic System: Equations of Motion

The governing equations of motion of the complete nonlinear aeroelastic system can be written in the standard compact form as:

$$\begin{bmatrix} m & mx_\theta b \\ mx_\theta b & I_\theta \end{bmatrix} \begin{bmatrix} \ddot{h} \\ \ddot{\theta} \end{bmatrix} + \begin{bmatrix} c_h & 0 \\ 0 & c_\theta \end{bmatrix} \begin{bmatrix} \dot{h} \\ \dot{\theta} \end{bmatrix} + \begin{bmatrix} k_h(h) & 0 \\ 0 & k_\theta(\theta) \end{bmatrix} \begin{bmatrix} h \\ \theta \end{bmatrix} = \begin{bmatrix} -L \\ M \end{bmatrix} \tag{2.30}$$

where the relevant parameters have already been described in Section 2.1. Substituting the external aerodynamic loads formulation derived in Section 2.2.1, Equation (2.30) can be explicitly expressed as:

$$\begin{bmatrix} m & mx_\theta b \\ mx_\theta b & I_\theta \end{bmatrix} \begin{bmatrix} \ddot{h} \\ \ddot{\theta} \end{bmatrix} + \begin{bmatrix} c_h + \rho U b C_{L_\alpha} & \rho U b^2 C_{L_\alpha}(1/2 - a) \\ \rho U b^2 C_{m_\alpha} & c_\theta - \rho U b^3 C_{m_\alpha}(1/2 - a) \end{bmatrix} \begin{bmatrix} \dot{h} \\ \dot{\theta} \end{bmatrix} + \begin{bmatrix} k_h(h) & \rho U^2 b C_{L_\alpha} \\ 0 & -\rho U^2 b^2 C_{m_\alpha} + k_\theta(\theta) \end{bmatrix} \begin{bmatrix} h \\ \theta \end{bmatrix} = \begin{bmatrix} -\rho b \Delta C_L(i_{sp}) \\ \rho b^2 \Delta C_m(i_{sp}) \end{bmatrix} U^2 i_{sp}. \tag{2.31}$$

For control law design purpose, it is useful to convert the system to a state-space formulation, with state variable vector:

$$\bar{x} = \begin{bmatrix} x_1 \\ x_2 \\ x_3 \\ x_4 \end{bmatrix} = \begin{bmatrix} h \\ \theta \\ \dot{h} \\ \dot{\theta} \end{bmatrix} \tag{2.32}$$

The forthcoming transformed equations of motion can be written as:

$$\dot{\bar{x}} = f_\mu(\bar{x}) + g(\bar{x}) U^2 i_{sp} \tag{2.33}$$

with

Table 2.5: System variables for the wing-spoiler configuration.

Parameter	**Definition**
d	$m(I_\theta - mx_\theta^2)b^2$
k_1	$I_\theta k_h/d$
k_2	$(I_\theta \rho b C_{L_\alpha} + mx_\theta b^3 \rho C_{m_\alpha})/d$
k_3	$-mx_\theta b k_h/d$
k_4	$(-mx_\theta b^2 \rho C_{L_\alpha} - m\rho b^2 C_{m_\alpha})/d$
$p(x_2)$	$(-mx_\theta b/d)k_\theta(x_2)$
$q(x_2)$	$(m/d)k_\theta(x_2)$
c_1	$[I_\theta(c_h + \rho U b C_{L_\alpha}) + mx_\theta \rho U b^3 C_{m_\alpha}]/d$
c_2	$[I_\theta \rho U b^2 C_{L_\alpha}(1/2 - a) - mx_\theta b c_\theta + mx_\theta \rho U b^4 C_{m_\theta}(1/2 - a)]/d$
c_3	$(-mx_\theta b c_h - mx_\theta \rho U b^2 C_{L_\theta} - m\rho U b^2 C_{m_\theta})/d$
c_4	$[mc_\theta - mx_\theta \rho U b^3 C_{L_\theta}(1/2 - a) - m\rho U b^3 C_{m_\theta}(1/2 - a)]/d$
g_3	$(1/d)(-I_\theta b \rho \Delta C_L(i_{sp}) + mx_\theta \rho b^3 \Delta C_m(i_{sp})$
g_4	$(1/d)(mx_\theta b^2 \rho \Delta C_L(i_{sp}) + m\rho b^2 \Delta C_m(i_{sp})$

$$f_\mu = \begin{bmatrix} x_3 \\ x_4 \\ -k_1 x_1 - [k_2 U^2 + p(x_2)]x_2 - c_1 x_3 - c_2 x_4 \\ -k_3 x_1 - [k_4 U^2 + q(x_2)]x_2 - c_3 x_3 - c_4 x_4 \end{bmatrix} \tag{2.34}$$

$$g(x) = \begin{bmatrix} 0 \\ 0 \\ g_3 \\ g_4 \end{bmatrix} \tag{2.35}$$

The auxiliary variables defined in Table 2.5 serve to reduce the state-space formulation into the compact form of Equation (2.33). Again, the system parametric dependency on the freestream velocity U and also on the elastic axis location a is gathered and highlighted in the conventional notation $f_\mu(x)$ of Eq.(2.34) . Strictly speaking, the subscript μ should be replaced by the vector of the parameters $[U \quad a]$. However, in this occasion the simplified notation is adopted, keeping in mind that the solutions are in fact a two-parameter family of solutions.

The mathematical formulation used to account for external wind disturbances is slightly different from the wing-flap configuration described in Section 2.1. In this formulation the aeroelastic system equations do not need to be modified with an additive term to account for gusts acting on the wing section. In fact, external gust disturbances are applied simply by adding the contribution given by the gust velocity profile to the aerodynamic angle of

attack computation, used to interpolate the coefficients database, which in a two dimensional problem it means to consider $\Delta\alpha_{gust} = atan(w_G(\tau)/U)$. Herein $w_G(\tau)$ denotes the vertical component of the disturbance velocity and τ is a dimensionless time defined as $\tau = Ut/b$. Consequently, the effective angle of attack formulation, adopted in the actual lift and aerodynamic moment expressions, is given by:

$$\alpha = \Big[\theta + \frac{\dot{h}}{U}\Big(\frac{1}{2} - a\Big)b\Big(\frac{\dot{\theta}}{U}\Big) + \Delta\alpha_{gust}\Big]. \tag{2.36}$$

For sake of consistency with the aeroelastic system control literature, three different gust distributions are applied to the aeroelastic model, similarly to [64, 82, 83, 84], as described in section 2.2.3.

2.2.3 External Gust Disturbances

The different gust disturbances, applied to the aeroelastic models with two different solutions, are hereafter mathematically expressed and their profiles shown in Figure 2.17.

- Exponential graded gust

$$w_G(\tau) = H(\tau)w_0\big(1 - e^{-\frac{0.75\tau}{3}}\big)$$

- Combined sinusoidal and random gust

$$w_G(\tau) = w_0 \sin(6\pi b\tau/U) + d_n H(\tau)$$

- Triangular gust of finite duration

$$\begin{aligned} w_G(\tau) = 2w_0\tfrac{\tau}{\tau_G}\big(H(\tau) - H(\tau - \tfrac{\tau_G}{2})\big) \\ +2\ \mathrm{w}_0(\tfrac{\tau}{\tau_G} - 1)\big(H(\tau - \tau_G) - H(\tau - \tfrac{\tau_G}{2})\big) \end{aligned}$$

where $H(\cdot)$ is the Heaviside function, commonly defined as:

$$H(x) = \begin{cases} 0 & \text{if } x > 0 \\ \frac{1}{2} & \text{if } x = 0 \\ 1 & \text{if } x < 0 \end{cases} \tag{2.37}$$

and $\tau_G = Ut_g/b$, $t_g = 0.5(sec)$ is the dimensionless time of the gust. Referring to Figure 2.17, $w_0 = 0.07$ for cases (a) and (b), whereas in case (c) $w_0 = 0.7$. The random component in case (b), $d_n H(\tau)$, is obtained by filtering white noise with unit variance through a transfer function defined as $F_d(s) = 10^{-5}/(s + 5)$.

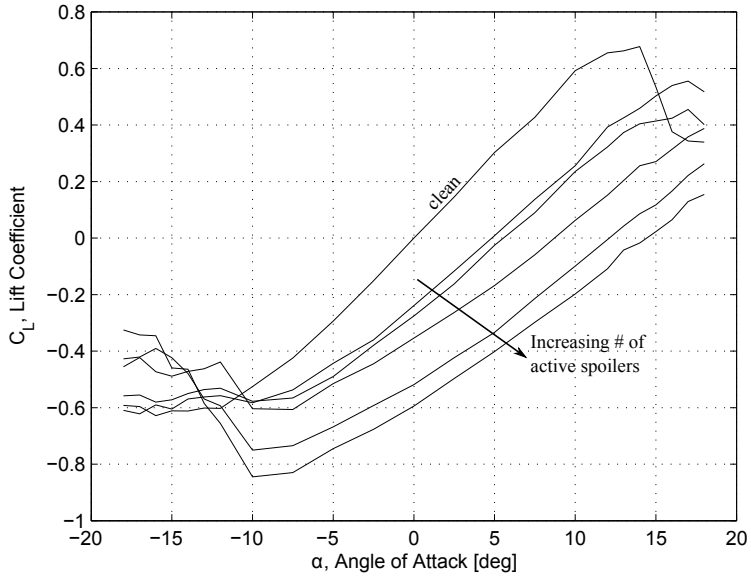

Figure 2.14: Wing-Spoiler configuration Aerodynamic Database, lift coefficient experimental values. Transition from clean to 5 open spoiler configuration is specified by the arrows

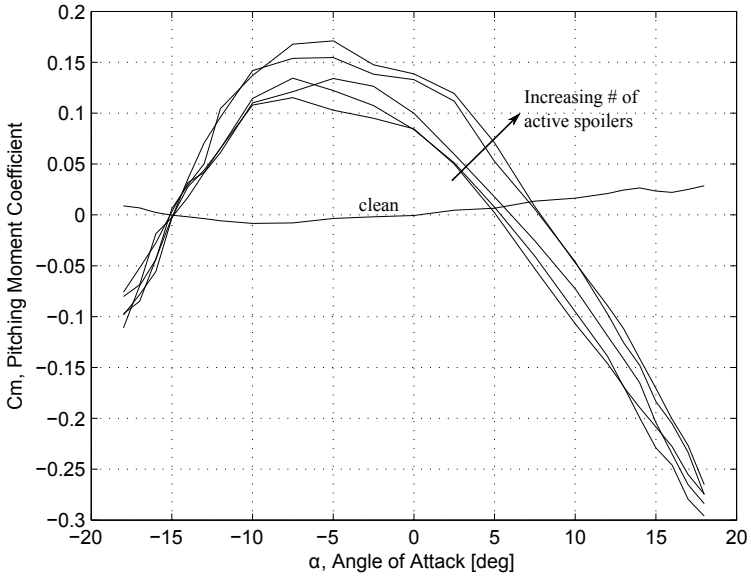

Figure 2.15: Wing-Spoiler configuration Aerodynamic Database, pitching moment coefficient experimental values. Transition from clean to 5 open spoiler configuration is specified by the arrows

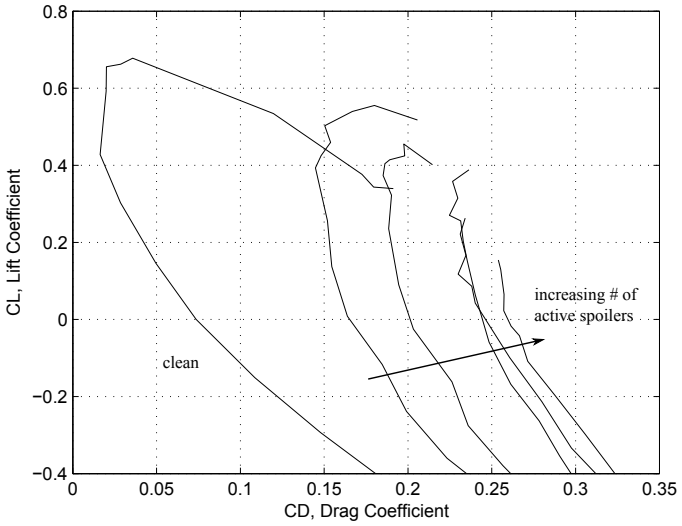

Figure 2.16: Wing-Spoiler configuration Aerodynamic Database, Polar. Transition from clean to 5 open spoiler configuration is specified by the arrows

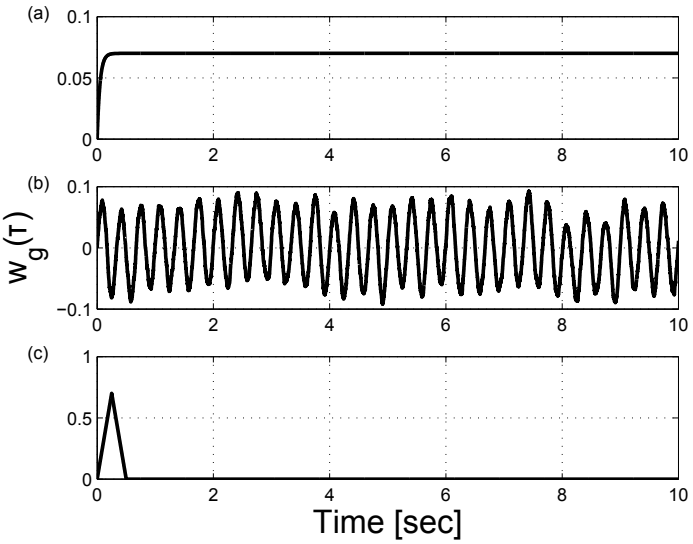

Figure 2.17: External disturbance velocity $w_G(\tau)$, (a) exponential graded gust, (b) combined sinusoidal and random gust, (c) triangular gust

2.2.4 Nonlinear Aeroelastic System Properties: Wing-Spoiler Model

The aerodynamic model, experimentally obtained from the prototype wind tunnel testing, and coupled to the same structural model of the wing-flap configuration, has been set up with the same parameters reported in Table 2.4, for research consistency purpose. This choice has been made for the sake of consistency in comparing the two different aerodynamic models and control surfaces solutions and to allow coherent evaluation of the dynamic response in time domain of the wing section with the novel actuation system. Moreover, the same type of analysis at flutter, post-flutter and simulated failure conditions has been done and hereafter reported. The wing section schematic of the configuration under analysis is reported in Figure 2.13. First, the time histories of the wing section free response are reported Figure 2.18, Figure 2.19, Figure 2.20 and Figure 2.21. The pitch and plunge phase diagram and power spectral density, always referred to the free uncontrolled response of the wing section, are reported in Figure 2.22 and Figure 2.23. Albeit the structural model is maintained unaltered, the resulting aeroelastic model exhibits small differences in their dynamic properties because of the different nature of the two aerodynamic models: linear and analytic for the wing-flap solution; experimental and fully nonlinear for the wing-spoiler architecture. In addition, differences in the aerodynamic loads are introduced by the employment of different airfoils in the two models: flat plate for the wing-flap solution and NACA 0024 for the prototyped wing-spoiler configuration. With the settings of Table 2.4 the aeroelastic model of the prototyped wing section shows a LCO behavior at the critical wind speed $U_{flutter} = 7.5(m/s)$ in nominal condition, which is $0.5(m/s)$ higher than the other wing. The oscillatory response is always obtained by exciting the system with an initial pitch angle state perturbation of 0.1 radians ($5.73(deg)$), namely $\bar{x}(0) = [h \quad \alpha \quad \dot{h} \quad \dot{\alpha}] = [0 \quad 0.1 \quad 0 \quad 0]$. Figure 2.18 and Figure 2.19 demonstrate how for slower wind speed the behavior is damped, in contrast with the the results of the previous wing model implemented in Equations (2.13) and (2.14), the wing-spoiler plant does not show any divergent behavior beyond a certain wind speed. Precisely, a proportional relation between the oscillations' amplitude and the wind speed is detected instead. The same behavior is observable both in pitch and plunge degrees of freedom. The analyzed cases and the resulting dynamic response of the proposed nonlinear aeroelastic system are summarized and reported in Table 2.6. Moreover, even if for nominal structural condition the flutter speed has an higher value, when a failure is simulated it remains unchanged with respect to the quasi-steady aerodynamic model. As for the previous configuration, a reduction of the stiffness matrix by 50%, $K_{reduced} = K_{nominal}/2$ has been applied, leading to a modification of the system proper frequencies and phase, as shown in Figure 2.23 and

Table 2.6: Free Response Analysis: Spoiler-Plant without Failure

	Case (a)	**Case (b)**	**Case (c)**	**Case (d)**
$\bar{x}(0)$	$[0, 0.1, 0, 0]$	$[0, 0.1, 0, 0]$	$[0, 0.1, 0, 0]$	$[0, 0.1, 0, 0]$
Stiffness	K_{nom}	K_{nom}	K_{nom}	K_{nom}
Wind Speed	$5(m/s)$	$7.5(m/s)$	$9(m/s)$	$15(m/s)$
Response	Damped	LCO	LCO	Divergent
Proper Freq.	—	$3.296(Hz)$	$3.662(Hz)$	—
Pitch Amp.	—	$6.12(deg)$	$7.66(deg)$	—
Plunge Amp.	—	$1.91e^{-3}(m)$	$1.87e^{-3}(m)$	—
Condition Name	Pre-Flutter	Flutter	Post-Flutter	Divergence

Table 2.7: Free Response Analysis: Spoiler-Plant with Failure

	Case (a)	**Case (b)**	**Case (c)**	**Case (d)**
$\bar{x}(0)$	$[0, 0.1, 0, 0]$	$[0, 0.1, 0, 0]$	$[0, 0.1, 0, 0]$	$[0, 0.1, 0, 0]$
Stiffness	K_{red}	K_{red}	K_{red}	K_{red}
Wind Speed	$5(m/s)$	$7(m/s)$	$9(m/s)$	$15(m/s)$
Response	Damped	LCO	LCO	Divergent
Proper Freq.	—	$2.319(Hz)$	$2.686(Hz)$	—
Pitch Amp.	—	$6.07(deg)$	$8.914(deg)$	—
Plunge Amp.	—	$2.79e^{-3}(m)$	$2.88e^{-3}(m)$	—
Condition Name	Pre-Flutter	Flutter	Post-Flutter	Divergence

Figure 2.22. However, despite the unchanged critical velocity $U_{flutter}$, an adaptive control algorithm must be used to accommodate the modification in the correlation between the states and their derivatives. The analyzed cases and the resulting dynamic response of the proposed nonlinear aeroelastic system with simulated failure are summarized and reported in Table 2.7.

2.2.4.1 Parametric Analysis of the Linearized Wing-Spoiler Plant

To study the effect of the aerodynamic model experimentally obtained and implemented on the wing-spoiler configuration aeroelastic system the same parametric analysis, presented for the wing-flap configuration, has been carried out. It consists of a *Root-Locus* analysis of the linearized model for different values of the parameters that significantly affect the dynamic features of the wing LCO motion, with the objective of identifying the stability margin of the plant. The same considerations, discussed in Section 2.1.1.1 can be drawn about the validity and interest of the current analysis. The outcomes of the analysis confirm what has been observed for the previous

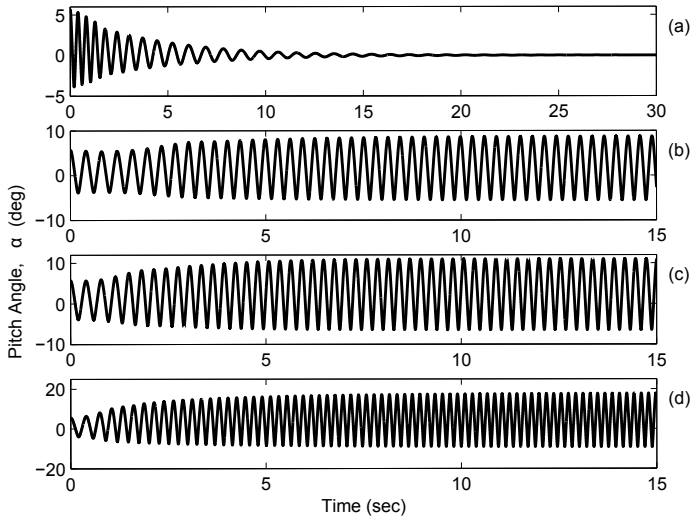

Figure 2.18: Prototyped aeroelastic System Free Response, pitch angle time histories: (a) at $U = 5(m/s) < U_{flutter}$; (b) at $U = 7.5(m/s) = U_{flutter}$, (c) at $U = 9(m/s) > U_{flutter}$, at $U = 15(m/s) > U_{flutter}$.

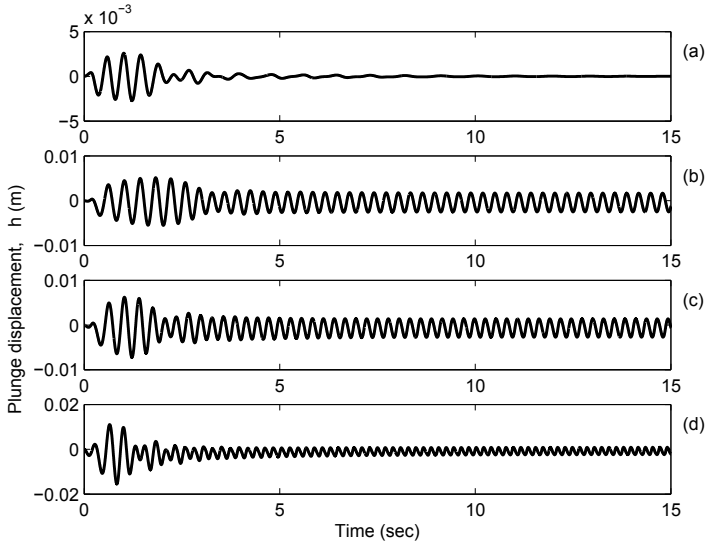

Figure 2.19: Prototyped aeroelastic System Free Response, plunge displacementtime histories: (a) at $U = 5(m/s) < U_{flutter}$; (b) at $U = 7.5(m/s) = U_{flutter}$, (c) at $U = 9(m/s) > U_{flutter}$, at $U = 15(m/s) > U_{flutter}$.

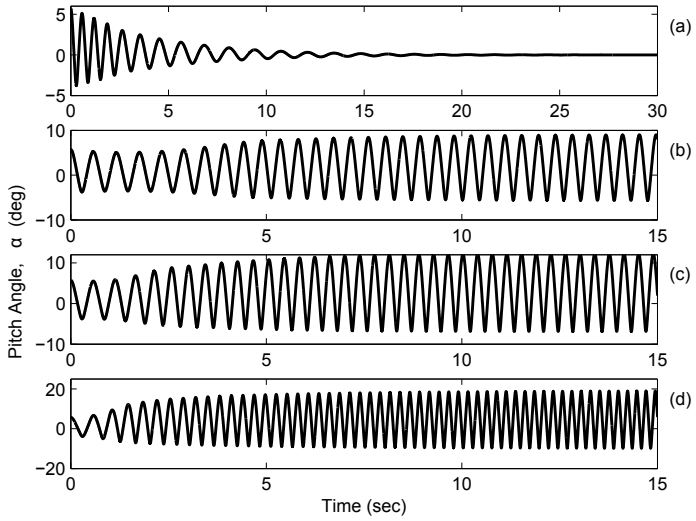

Figure 2.20: Prototyped aeroelastic system free response with simulated failure, pitch angle time histories: (a) at $U = 5(m/s) < U_{flutter}$; (b) at $U = 7(m/s) = U_{flutter}$, (c) at $U = 9(m/s) > U_{flutter}$, at $U = 15(m/s) > U_{flutter}$.

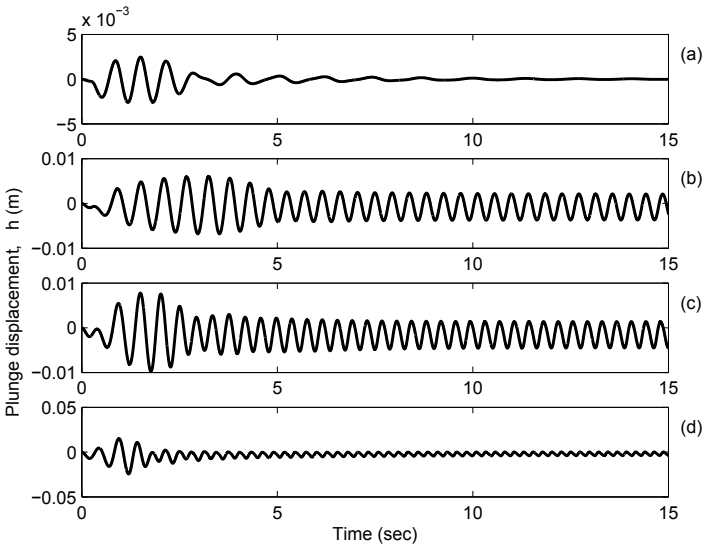

Figure 2.21: Prototyped aeroelastic system free response with simulated failure, plunge displacement time histories: (a) at $U = 5(m/s) < U_{flutter}$; (b) at $U = 7(m/s) = U_{flutter}$, (c) at $U = 9(m/s) > U_{flutter}$, at $U = 15(m/s) > U_{flutter}$.

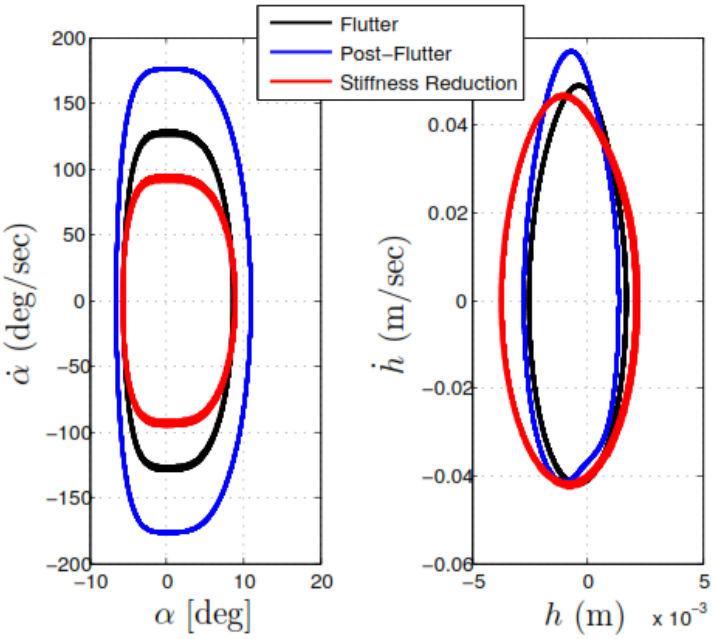

Figure 2.22: Prototype aeroelastic system phase diagram comparison.

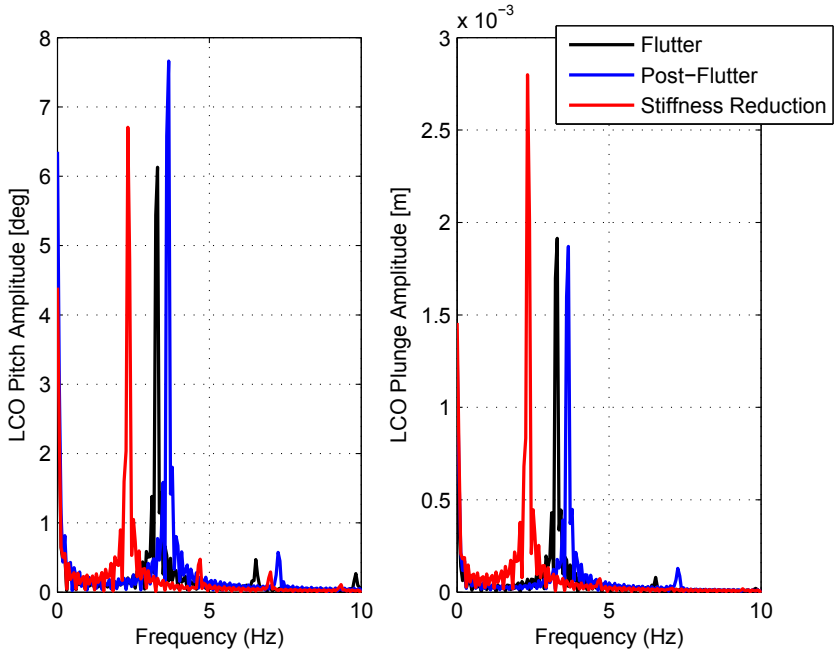

Figure 2.23: Prototype aeroelastic system power spectra comparison.

configuration, with some differences in the pole values due to the different airfoil used in the two configurations. In Figure 2.24a shows the effects of the initial angle of attack on the two conjugated poles location. The discontinuity of the root path can be attributed to the nonlinearity in the pitch degree of freedom (Table 2.4). In particular, the initial pitch angle is made variable between 0 and $0.1(rad)$, with steps of $\Delta\alpha = 0.005(rad)$. Three different regions can be identified from the poles path observation: an initial stability region from $\alpha = 0$ to $alpha = 0.065(deg)$; an unstable region within 0.065 and 0.075 of the α range; and then another stability region at higher frequency for higher α. As $\alpha = 0.1(rad)$ is the usual perturbation imposed to excite the system to LCOs throughout the whole study, this condition is chosen as linearization point to pursue the rest of the analysis. Figure 2.24b shows the effect of the wind speed U on the aeroelastic system. As expected, the wind speed increment causes the system transition from stable to unstable. The stable flutter condition, not damped nor excited, would have been met at the imaginary axis crossing point, if the model were intrinsically linear. In fact, U is varied from 5 to 11 (m/s) with steps of $\Delta U = 1(m/s)$, crossing the Im axis at about $6.5(m/s)$. This value is $1(m/s)$ lower than the nonlinear plant stable LCO condition because of the linear approximation. However, this discrepancy does not invalidate the results of the root-locus analysis which is not performed for control algorithm design purpose, but merely to reproduces qualitatively the impact of the several plant parameters on the plant dynamics. Figure 2.25 shows the combined effect of the elastic axis variation with the wind speed increment. In this case the wind speed variation acts emphasizing the a location effect, stretching the relevant the poles path. As it can be noticed from the same plot there is a unique location of minimum a below which instability is met. This can be seen as a stability margin for the wing section, as all the other a values move the poles leftwards in the stable complex half-plane. In particular, it can be noticed that as the E.A. approaches the c.g. the oscillations occurs at higher frequency and lower damping. The opposite behavior is detected when the E.A. moves further from c.g. In the linear approximation a is varied from 0.2 to -0.4 with steps of -0.1, and a trend inversion occurs when $a = 0$ is crossed. Figure 2.26 shows the effect on the system roots for a failure simulated by means of a percentage reduction of the stiffness matrix. Figure 2.26a concerns a K reduction solely, whereas Figure 2.26b shows the combined effect of simultaneous U increment and K reduction. In this case, the stiffness matrix is varied from the nominal K value, reported in Table 2.4, to a value of $K_{reduced} = 0.2K_{nom}$, with steps of 10%. The primarily effect is to drive the roots rightwards, towards the unstable half-plane. Again, the analysis on the combined effect emphasize the importance of considering the variation of both parameters to test the robustness of adaptive control algorithm.

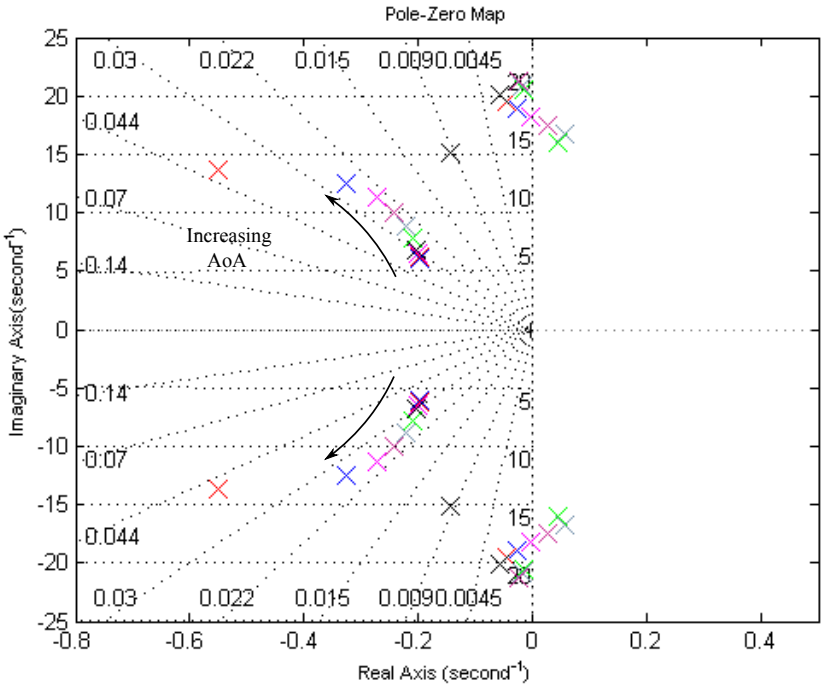

(a) $\alpha(0)$ Initial condition effect

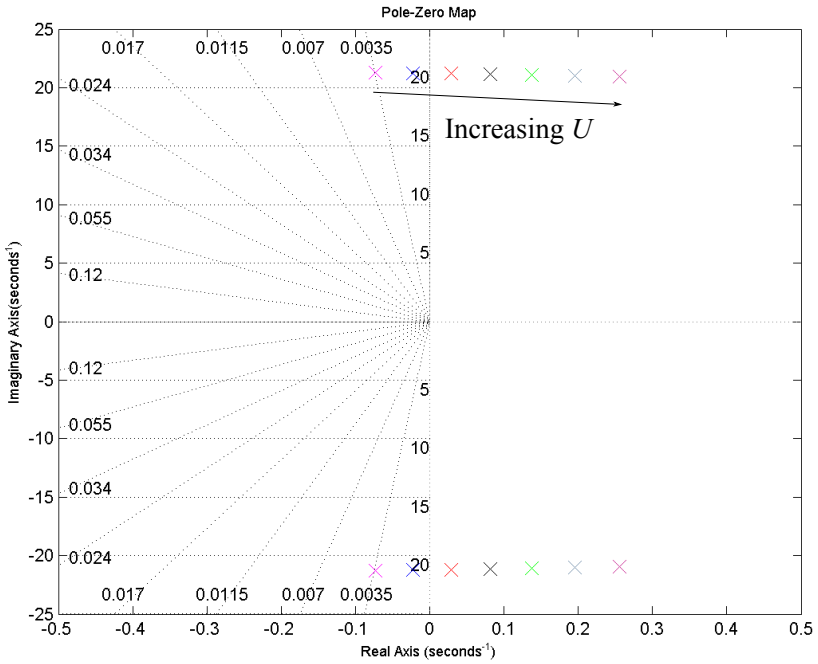

(b) U variation effect

Figure 2.24: Spoiler plant root-loci parametric analysis results

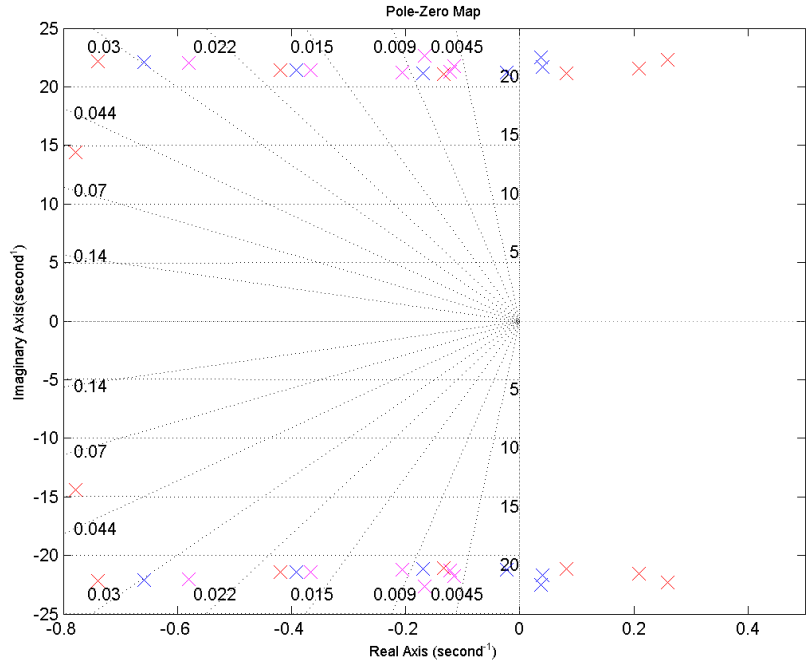

(a) a and U variation effect

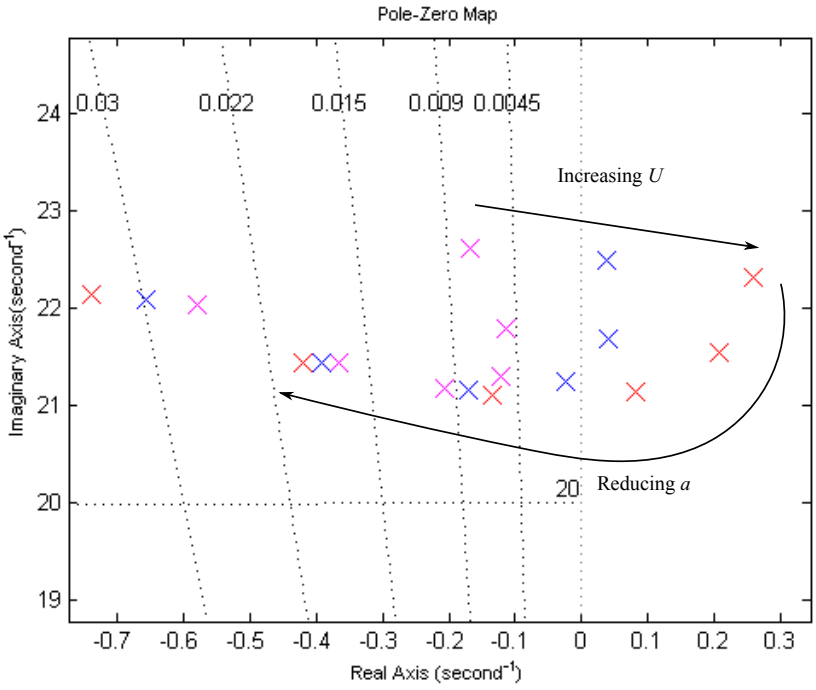

(b) a and U variation effect, magnified

Figure 2.25: Spoiler plant root-loci parametric analysis results

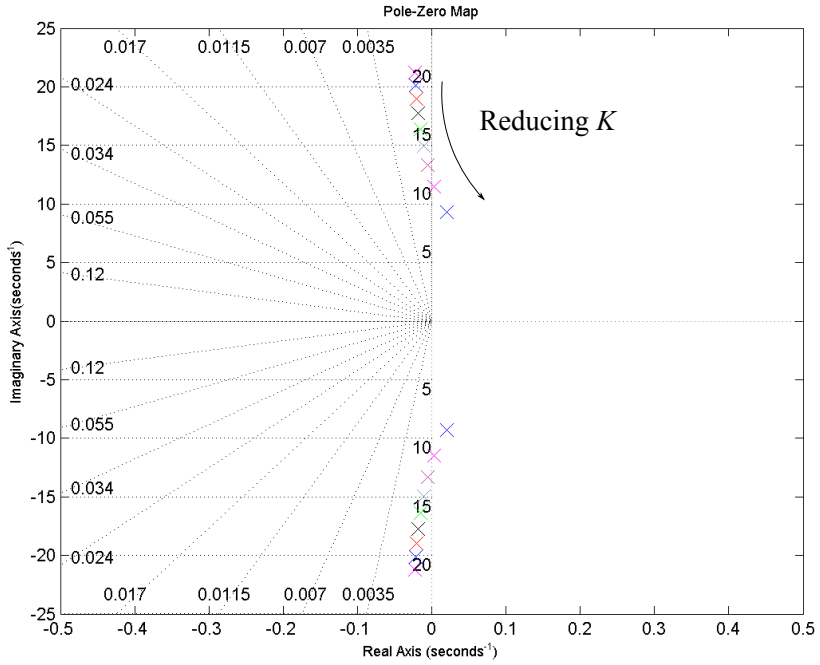

(a) Stiffness variation effect

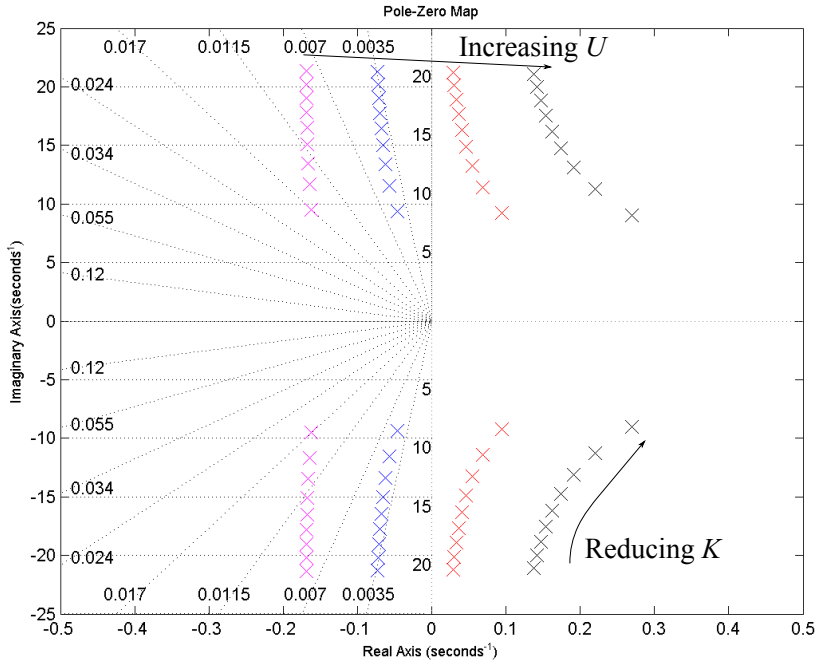

(b) K and U variation

Figure 2.26: Spoiler plant root-loci parametric analysis results

Chapter 3

Model Reference Adaptive Control Algorithms

Flutter instability of nonlinear aeroelastic systems (structurally and/or aerodynamically speaking) represents a critical condition to test and validate control algorithm, [85, 66, 76] are case in point. On the benchmark 2D aeroelastic model, described in Section 2.1, several linear and nonlinear active controllers [86, 72, 69] as well as various adaptive control schemes [75, 10] have been tested. In spite of the recent years flourishing literature on aeroelastic adaptive controls, there is a noted lack of robustness and sensitivity analysis with respect to structural proprieties degradation which might be associated with a structural failure. Structural mode frequencies and aeroelastic response, including Limit Cycle Oscillations (LCOs) characteristics, are significantly affected by changes in stiffness. This leads to a great interest in evaluating and comparing the adaptation capabilities of different control architectures subjected to large plant uncertainties and unmodeled dynamics.
The classical wing-flap configuration used as benchmark for flutter suppression active controller testing and performance evaluation has been illustrated and discussed in detail in Section 2.1.

The contribution of this Chapter lies in the derivation and implementation of several output feedback *Model Reference Adaptive Control* (MRAC) and L_1 *adaptive control* solutions for the wing-flap configuration of the 2D aeroelastic nonlinear systems first, and in evaluating the robustness of different control strategies to damage leading to the deterioration of the structural stiffness characteristics. The more robust control algorithm is also implemented to control the wing-spoiler configuration design, manufactured and mathematically modeled in this work, Section 2.2. The Standard MRAC, a Modified MRAC for transient and tracking performance improvement, a basic L_1 adaptive controller and a modified L_1 are the four model-reference adaptive control solutions analyzed. The standard direct MRAC solution

[87] serves as threshold to assess whether or not the more complex algorithms are an effective improvement to it. Both Modified Model Reference [87] and the two L_1 adaptive controllers [5], which embody different modifications to the standard scheme with the intent to improve robustness and performance at the same time, are proposed in this work. For consistency of the analysis, all the adaptive scheme solutions are derived for the same control objective, [76, 74, 73, 75, 10], and are applied to the same aeroelastic plant, which equation of motion are from Eq. 2.18, 2.19 and 2.20. The model has pitch polynomial type structural nonlinearities and uses a single trailing-edge control surface.

3.1 Control Objective

The control objective is to suppress the aeroelastic oscillatory motion of the system by driving the pitch angle α to a constant set point, typically zero degrees, while adaptively compensating for uncertainties in all parameters of the model and the nonlinearities. In this particular research, it is assumed that the only available states for feedback are $x_{observable} = \begin{bmatrix} \alpha & \dot{\alpha} \end{bmatrix}$. Whether the pitch regulation is achieved, the plunging motion is consequently damped-out, as proven in literature multiple times, thus, the system is fully controllable [88], $x_{controllable} = \begin{bmatrix} h & \alpha & \dot{h} & \dot{\alpha} \end{bmatrix}$. The aeroelastic system equations are rewritten into amenable form as to fit the problem formulation for each control scheme. A detailed description of the various architectures, control, and adaptive laws is supplied next to highlight all the differences between them.

3.2 Standard MRAC

Equation (2.18), which represent the state-space formulation of the wing-flap non linear aeroelastic system, can be rewritten in amenable form for a standard MRAC formulation. Considering that $g(x)$ consists of constants, and partitioning $f_\mu(x)$ in the constant and variable part, the nonlinear aeroelastic system to be controlled belongs to a class of plant described by

$$\dot{x}(t) = Af(x,t) + Bu(t) \tag{3.1}$$

where A and B are constant matrix, $f(x,t)$ is a nonlinear function and $u(t)$ is the control signal. For control law design purpose, the unknown component of the state matrix and nonlinear function can be decomposed from the known part as follow:

$$\begin{aligned} A &= A^* + \Delta A \\ f(x,t) &= f^* + \Delta f(x,t) \\ B &= B^* + \Delta B \end{aligned} \tag{3.2}$$

where the superscript $(\cdot)^*$ denotes the nominal values and ΔA, $\Delta f(x,t)$ and ΔB denote the uncertainties of A, $f(x,t)$ and B, respectively. Hence, the system equation dynamic can be expressed as

$$\dot{x}(t) = A^* f^*(x,t) + \big(A^* \Delta f(x,t) + f^*(x,t)\Delta A + \Delta A \Delta f(x,t)\big) + \big(B^* + \Delta B\big)u(t). \tag{3.3}$$

The previous equation, Eq. (3.3), is usually re-written in the following form amenable to model reference control law formulation:

$$\dot{x}(t) = A_m x(t) + B{\theta^*}^T x(t) + Bu(t) \tag{3.4}$$

where $x \in \mathbb{R}^n$ is the state vector, assumed to be measurable ($n = 2$), $u \in \mathbb{R}$ is the control input, $\theta^* \in \mathbb{R}^n$ is an unknown parameter vector belonging to a known compact convex set $\Omega \in \mathbb{R}^n$, $A_m \in \mathbb{R}^{n \times n}$ is Hurwitz [89] and with $B \in \mathbb{R}^n$ are known, and the pair $(A_m; B)$ is controllable. As proven in [87], the fact that the parameter θ^* appears linearly does not mean that the dynamic are linear, [87]. For a standard MRAC scheme, the control problem lies in choosing $u(t)$ such that all the states $x(t)$ in the closed-loop system are uniformly bounded and track the state vector of a desired reference model, described as follows

$$\dot{x}_m(t) = A_m x_m(t) + B_m r(t), \qquad x_m(0) = x_0 \tag{3.5}$$

both in transient and in steady-state for any bounded reference signal $r(t)$. The standard MRAC solution to this problem is based on the states error between the plant and the reference model [87] defined as

$$e(t) = x(t) - x_m(t) \tag{3.6}$$

from which the unknown parameter vector $\theta^*(t)$ is estimated by

$$\dot{\hat{\theta}}(t) = proj\Big(\Gamma e^T(t) P B(t)\Big), \qquad \hat{\theta}(0) = \hat{\theta}_0 \in \Omega \tag{3.7}$$

and the associated control law is

$$u(t) = -\hat{\theta}^T x(t) + k_0 r(t) \tag{3.8}$$

where $\hat{\theta}(t)$ is the estimate of the unknown parameters $\theta^*(t)$. $\Gamma > 0$ is the adaptive gain, e is the tracking error, and $P = P^t$ is the solution of the Lyapunov equation $PA_m + A_m^T P = -I$. the projection operator is used to constrain $\hat{\theta}(t)$ inside the compact set Ω for all t and is defined in [87] and [5]. For the particular application considered, the reference signal $r(t)$ is simply a constant set point, the elastic response has to damp-out with time to zero, which reduces the system to a regulation problem. The controller design parameters for the reference model are selected as follows:

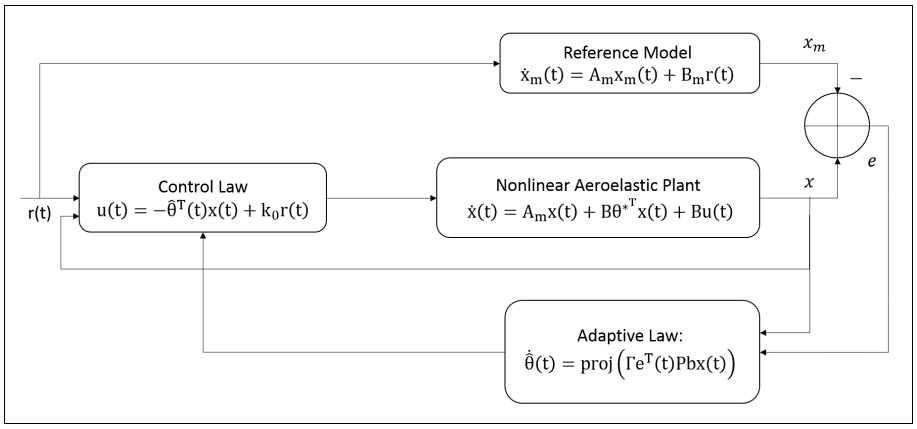

Figure 3.1: Standard MRAC scheme architecture

$$A_m = \begin{bmatrix} 0 & 1 \\ -0.3 & -1 \end{bmatrix}; B_m = \begin{bmatrix} 0 \\ 4 \end{bmatrix}; x_0 = \begin{bmatrix} 0 \\ 0.1 \end{bmatrix}; r(t) = 0; \tag{3.9}$$

while the adaptive parameters are

$$P = 500 \cdot I; \Gamma = 10; B = \begin{bmatrix} 1 \\ 0.1 \end{bmatrix}; \Omega \in [-5 \quad 5]; \hat{\theta}(0) = \begin{bmatrix} 0 \\ 0 \end{bmatrix}. \tag{3.10}$$

The block diagram of the standard MRAC scheme architecture is reported in Figure 3.1, to better identify the main elements of the described closed-loop configuration.

3.3 Modified MRAC

The control algorithm, hereafter obtained for flutter suppression purpose, is a modification of the standard MRAC scheme for transient performance and tracking error enhancement [90, 87]. For sake of simplicity it will be named as *Modified MRAC* in the rest of the discussion. It is essentially based on an enrichment of the feedback signal, by means of a signal filtering operation in a particular location of the closed-loop scheme, which differ significantly from the one proposed for the L_1 adaptive control scheme [91], obtained and described in Section 3.4. The problem formulation is still a model reference-tracking problem; however, the controller derivation is based on a parametric expression of equation (3.4) and the adaptive and control laws work on normalized signals, which increase the robustness of this scheme. Equation (3.4) can be rewritten as

$$x(t) = W_b(s)\left[\theta^{*^T} x(t)\right] + W_b(s)[u(t)] \tag{3.11}$$

where $W_b(s) = (sI - A_m)^{-1}B$. Based on $(A_m; B)$ controllability, a vector $c_0 \in \mathbb{R}^n$ is defined so that $W_m(s) \doteq c_0^T W_b(s)$ is a strictly proper minimum-phase transfer function. The parametric expression of the model is consequently written as

$$z(t) = {\theta^*}^T \phi(t) \tag{3.12}$$

where $z(t) = c_0^T x(t) - W_m(s)[u(t)]$ and $\phi(t) = W_m(s)[x(t)]$ are available for measurements. The structure and parameters of the unmodeled dynamics are assumed unknown. Performance improvement is obtained by enriching the control signal with an auxiliary input u_a, which involves the above mentioned feedback signal filtering

$$u(t) = -\hat{\theta^T}(t)x(t) + k_0 r(t) + u_a(t) \tag{3.13}$$

where

$$u_a(t) = -Q(s)[\epsilon m_s^2 + W_{c_0}(s)[W_b(s)[x^T(t)]\dot{\hat{\theta}}(t)]] \tag{3.14}$$

Herein, $W_{c_0}(s) = -c_0^T(sI - A_m)^{-1}$, $Q(s) = W_m(s)^{-1}/(\tau s + 1)^{n^*}$ and n^* is the relative degree of $W_m(s)$, while $\tau > 0$ is a design parameter. The associated adaptive law is expressed as

$$\dot{\hat{\theta}}(t) = proj\bigg(P(t)\epsilon(t)\phi(t)\bigg), \qquad \hat{\theta}(0) = \hat{\theta}_0 \in \Omega \tag{3.15}$$

$$\dot{P}(t) = -P(t)\frac{\phi(t)\phi^T(t)}{m_s^2}P(t), \qquad P(0) = P_0 \tag{3.16}$$

where ϵ is the estimation error and is defined as $\epsilon(t) = \frac{(z(t) - \hat{\theta}^T\phi(t))}{m_s^2}$. The normalizing signal is $m_s^2(t) = 1 + \phi^T(t)\phi(t)$, and it is designed to guarantee boundedness of $|\frac{\phi(t)}{m_s}(t)|$, independently whether $\phi(t)$ is bounded or not. It must be noticed that , in this formulation, P is a function of time and not a constant matrix, as in all the other model reference adaptive control laws investigated in this research work. Stability and convergence proof of this robust adaptive law are reported in [87]. For consistency, the reference model state matrix, the initial conditions, $\hat{\theta}$ convex set and $P(0)$ are set identical to the other control schemes, eq. (3.10) while the different design parameters are set as follows

$$\tau = 0.5; \qquad c_0 = [1 \quad 1]^T. \tag{3.17}$$

It can be noticed that the filter $Q(s)$ has a similar expression to the L_1 filter $C(s)$, derived in Section 3.4. However, since it appears in a different location of the control schemes and operates on different signals, the two behaviors are fundamentally different as shown in the Chapter 4.

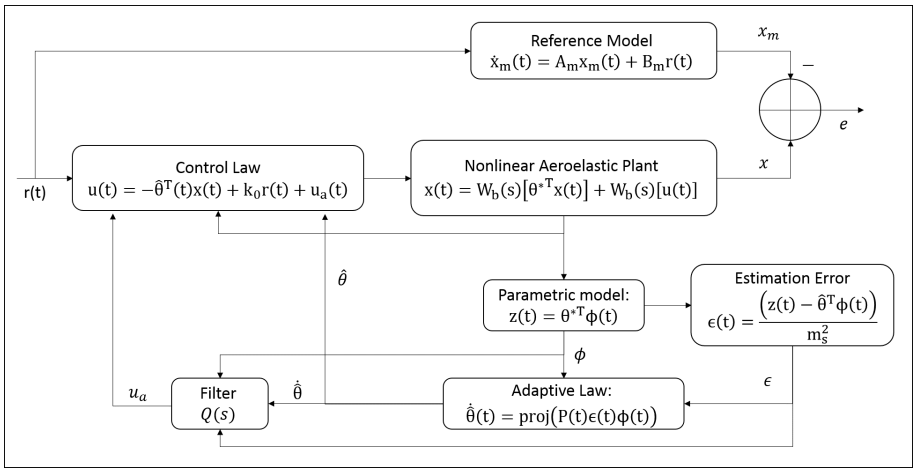

Figure 3.2: Modified MRAC scheme architecture

Figure 3.2 shows the closed-loop architecture of the MRAC scheme modified for transient and steady-state tracking error performance improvement. As noticeable, the tracking error is not feed-backed to contribute to the control command computation. This is due to the parametric formulation adopted in the control law formulation, which include the model reference dynamics, to be followed by the nonlinear aeroelastic system, implicitly in Eq. (3.11) and (3.12). Normalization, on the estimation error block, bounds the error dynamics making the closed-loop more robust. It is also worth to point out the filter location and the signals on which it operates, that is the key difference with respect the L_1 control architecture. It is placed before the control signal $u(t)$ computation and serves as enriching signal operating on the adaptive parameter derivative estimation, the actual parametric states and the actual estimated error signals.

3.4 L1 Adaptive Control

The L_1 control problem has the same formulation of the standard MRAC since it is defined as a tracking problem between the system dynamics, eq, (3.4) and the reference model dynamics, eq. (3.5). However, the solution, whose detailed derivation can be found in [5], slightly differs being based on a state predictor error

$$\tilde{x}(t) = x(t) - \hat{x}(t) \tag{3.18}$$

instead of the tracking error as in equation (3.6). The state predictor dynamics is given by

$$\dot{\hat{x}}(t) = A_m\hat{x}(t) + B(\hat{\theta}^T x(t) + u(t)), \quad \hat{x}(0) = x_0 \tag{3.19}$$

where A_m is the same Hurwitz matrix in eq. (3.5), $\hat{x}(t)$ are the predicted states, $x(t)$ are the actual sytsem states, $u(t)$ is the control signal and $\hat{\theta}$ is again the unknown parameters estimation computed by the adaptive law

$$\dot{\hat{\theta}}(t) = proj\Big(\Gamma \tilde{x}^T(t) P B x(t)\Big), \qquad \hat{\theta}(0) = \hat{\theta}_0 \in \Omega \tag{3.20}$$

The associate control law is defined as

$$u(t) = C(s)[-\hat{\theta}^T(t)x(t) + k_0 r(t)] \tag{3.21}$$

where $C(s)$ is a stable strictly proper transfer function, with $C(0) = 1$. This is a first-order low-pass filter, which assumes the form

$$C(s) = \frac{1}{ks+1} \tag{3.22}$$

with $k > 0$ being the design parameter. To guarantee stability and convergence, the condition $||W_b(s)(C(s)-1)||_1 \theta_{max} < 1$ must be respected, where $W_b(s) = (sI - A_m)^{-1}B$ and θ_{max} is an upper bound for $||\hat{\theta}||_1$. Γ and P have the same meaning as (3.7). However, contrary to the MRAC theory, the adaptive gain Γ in the L_1 *adaptive control* scheme is not subject to any stability constraint, because of the decoupling of the adaptive law dynamics from the system dynamics operated by the filter, placed in that particular location of the closed-loop architecture. This allows the designer to increase Γ to very high values for faster adaptivity, without affecting the controller robustness [5]. On these theoretical bases, the controller design parameters have been selected as follows:

$$A_m = \begin{bmatrix} 0 & 1 \\ -0.3 & -1 \end{bmatrix}; B = \begin{bmatrix} 1 \\ 0.1 \end{bmatrix}; x_0 = \begin{bmatrix} 0 \\ 0.1 \end{bmatrix}; k = 0.015; \tag{3.23}$$

$$P = 500 \cdot I; \Gamma = 10^7; \Omega \in [-5 \quad 5]; \hat{\theta}(0) = \begin{bmatrix} 0 \\ 0 \end{bmatrix}. \tag{3.24}$$

where the reference model state and control matrices, as well as the convex set boundaries for the adaptive parameters estimation and P are maintained equal to (3.10), for consistency of the analysis. Herein, the filter is tuned by trial and error and the adaptive gain is set high as suggest in [5]. Figure 3.3 shows the main element of the L_1 control architecture. The firs difference, with respect to the standard MRAC configuration, lies in the definition of a state estimator to generate the tracking error on which the adaptive law operates. However, the model reference dynamic response, to be followed by the plant, is implicitly included in its mathematical formulation, as eq. (3.19) clearly explain. The key point is the presence of the filter $C(s)$ that works on the control signal u, which has exactly the same formulation of a standard MRAC scheme. The location of the filter, justified

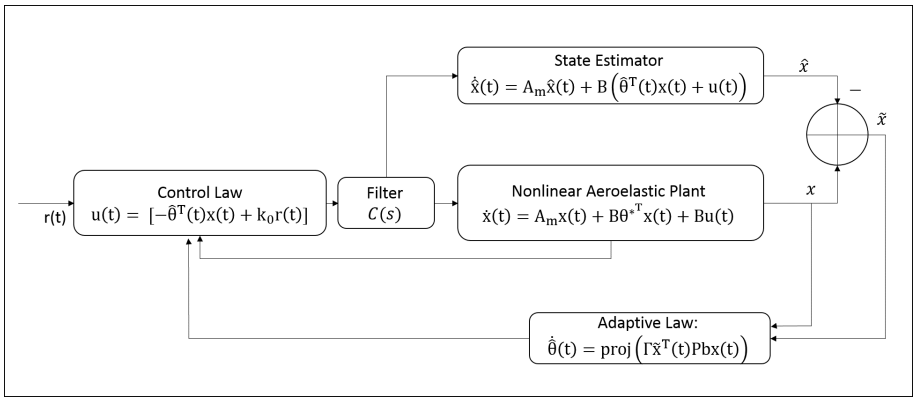

Figure 3.3: L1 scheme architecture

by the needs to cancel out the spurious oscillations of the adaptive parameters integration, caused by the extremely high gain imposed that makes the differential equation of the adaptive law too stiff, has been proven in [91] to reduce the robust stability margins, of a standard MRAC, in presence of unmodeled dynamics.

3.5 L1 Adaptive Control for Uncertain Input Gain

Even the 2D nonlinear dynamic aeroelastic system, objective of all the implemented adaptive control scheme and described by equations (2.18) and (2.12), belongs to the class of plant (3.1), as far as model reference adaptive control is concerned, though, based on the discouraging results obtained by the L_1 *adaptive control* standard scheme, another L_1 control architecture, thought for system with uncertain input gain, is implemented to improve the aeroelastic flutter suppression performances, [92]. The theory behind and the proof of stability can be found in [5]. Considering the nonlinearities of the aeroelastic system collected with the input uncertainties, it is possible to interpret eq. (2.18) as

$$\dot{x}(t) = A_m x(t) + B_m[wu + f_n(x,t)] \tag{3.25}$$

with $f_n(x,t)$ a new unknown nonlinear function and $B_m = [0 \quad b_{1_m}]$ a nominal value of the uncertain parameter $B_1 = B_{1_m} w$, where B_{1_m} is a known nominal value and w is an unknown parameter satisfying

$$0 < w_l \leq w \leq w_u \tag{3.26}$$

where are w_l and w_u are the lower and upper bounds respectively for the uncertain parameter w. If written as in eq. (3.25), the aeroelastic plant can be treated as belonging to a more general class of plant, of which the previous

considered class in eq. (3.4) is a minimization with less uncertainties, that is written as follows:

$$\begin{aligned} \dot{x}(t) &= A_m x(t) + B(\omega u(t) + \theta^T x(t) + \sigma(t)), \quad x(0) = 0; \\ y(t) &= C^T x(t); \end{aligned} \tag{3.27}$$

where $x(t) \in \mathbb{R}^n$ is the measured system state vector ($x_{measured}$), $u(t) \in \mathbb{R}$ is the control input and $y(t) \in \mathbb{R}^n$ is the regulated output in this case equal to measured states since $C = I \in \mathbb{R}^n$; $b \in \mathbb{R}^n$ is a known constant vector; $A_m \in \mathbb{R}^{n \times n}$ is the known Hurwitz martix describing the desired closed-loop dynamic; $\omega \in \mathbb{R}$ is an unknown constant with known sign; $\theta(t) \in \mathbb{R}^n$ is the vector of time varying unknown parameters; and $\sigma(t) \in \mathbb{R}$ are the model input disturbances.
As for the previous L1 control scheme the adaptation law is based on the prediction error

$$\tilde{x}(t) = x(t) - \hat{x}(t) \tag{3.28}$$

and so forth on the state prediction model, which in this case is written as:

$$\dot{\hat{x}}(t) = A_m \hat{x}(t) + B(\hat{\omega} u(t) + \hat{\theta}^T x(t) + \hat{\sigma}(t)), \quad \hat{x}(0) = 0; \tag{3.29}$$

which has obviously the same mathematical structure of the general class of plant, eq. (3.27), with the exception that the $\hat{\omega}, \hat{\theta}$ and $\hat{\sigma}$ are the adaptive estimation of the respective parameter without hat symbol. As a consequence, in this case each of the unknown parameter needs to be estimated and has its own projection based adaptive laws, as follows:

$$\begin{aligned} \dot{\hat{\theta}}(t) &= \Gamma proj(\hat{\theta}(t), -\tilde{x}^T(t) P B x(t)), \quad \hat{\theta}(0) = \hat{\theta}_0 \\ \dot{\hat{\sigma}}(t) &= \Gamma proj(\hat{\sigma}(t), -\tilde{x}^T(t) P B), \quad \hat{\sigma}(0) = \hat{\sigma}_0 \\ \dot{\hat{\omega}}(t) &= \Gamma proj(\hat{\omega}(t), -\tilde{x}^T(t) P B u(t)), \quad \hat{\omega}(0) = \hat{\omega}_0 \end{aligned} \tag{3.30}$$

where, as in Section 3.4, $\tilde{x} = \hat{x} - x$, $\Gamma \in \mathbb{R}^+$ is the adaptation gain and P is the solution of the Lyapunov equation $PA_m + A_m^T P = -Q$, with Q a chosen matrix positive definite. The projection operator contains the estimation of the each parameter inside a superimposed bounded convex set, so that $\omega \in \Omega = [\omega_l \quad \omega u]$, $\theta \in \Theta = [\theta_l \quad \theta u]$ and $\sigma \in \Delta = [\sigma_l \quad \sigma u]$. Also the control law is function itself of the estimated parameters, as follows:

$$u(s) = -kD(s)(\hat{\eta}(s) - k_g r(s)) \tag{3.31}$$

where $r(s)$ is the Laplace transform of $r(t)$, which for the regulation problem under investigation goes to zero, $k_g = -1/(C^T A_m^{-1} B)$ by definition,

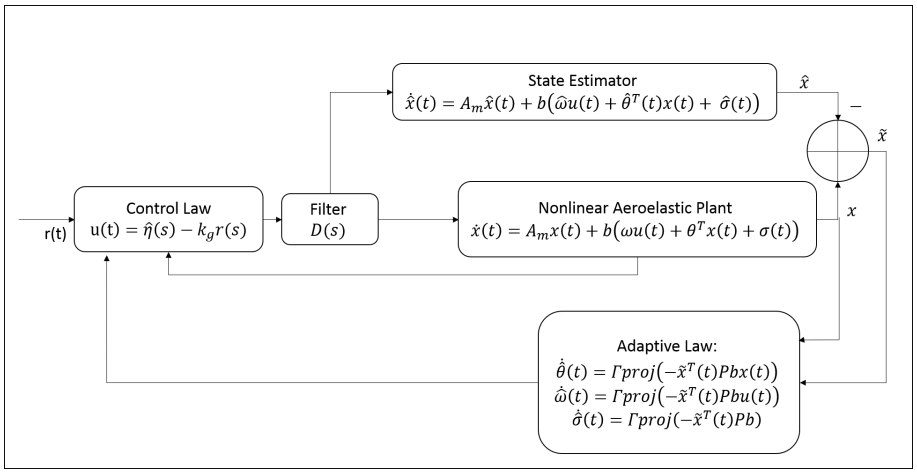

Figure 3.4: L1 for unknown input gain, scheme architecture

$\hat{\eta}(s)$ is the Laplace transform of $\hat{\eta}(t) = \hat{\omega}u(t) + \hat{\theta}^T x(t) + \hat{\sigma}$ that is the adaptive term, $k > 0$ and $D(s)$ are a feedback gain and a strictly proper transfer function, usually simply $D(s) = 1/s$. The final set of parameters is reported hereafter:

$$A_m = \begin{bmatrix} 0 & 1 \\ -4 & -7 \end{bmatrix}; Q = \begin{bmatrix} 10 & 0 \\ 0 & 10 \end{bmatrix}; k = 1; \tag{3.32}$$

$$P = \begin{bmatrix} 12.3214 & 1.25 \\ 1.25 & 0.8929 \end{bmatrix}; \Gamma = 10^7; \tag{3.33}$$

$$\Omega \in [-1.7 \quad 1.7]; \Theta \in [-1.5 \quad 1.5]; \Delta \in [-0.5 \quad 0.5]. \tag{3.34}$$

Figure 3.4 shows the closed-loop architecture for the more general L_1 control law examined. It is similar to Figure 3.3 with the exception that more unknowns are tolerated, since the adaptive parameters estimation operates on states, control input and disturbances at the same time. This control law actually perform better than the standard L_1 discussed in Section 3.4, as will be explain in the *Simulation and Results* section. However, as clearly noticeable from the design parameter values in Equation (3.33), the control law requires a more demanding tuning work aimed to narrow the domain of existence of the uncertainties estimated parameters for performance improvement, especially as far as convergence time is concerned.

Chapter 4

Simulation Results

To test and verify the control algorithm performances, their robustness and fastness in adaptation, an extensive set of simulations is carried out with the two degrees of freedom aeroelastic model, plunging and pitching, with both the actuation configurations presented in Chapter 2. First the trailing edge control surface solution is considered to assess which of the model reference adaptive control law better fits the proposed problem. The performances are assessed, through the closed-loop time-response analysis in a variety of circumstances. The verification and validation plan is defined by stressing the aeroelastic system with extreme off-design configurations in terms of external aerodynamic forces, derived from post-flutter wind speed and gust application, and in terms of modification of the internal plant parameters, such as the stiffness reduction induced by structural failures. To validated the overall control architecture effectiveness, only the more robust control law is subsequently applied to the novel designed actuation system, based on a multiple spoiler stripe located ahead of the wing aerodynamic center as described in Section 2.2.

4.1 Flutter Suppression for the Wing-Flap Configuration

The dynamic properties of the proposed wing-flap aeroelastic plant, whose parameters are reported in Table 2.1, has been deeply investigated in Chapter 2. The model shows an LCO behavior at the critical wind speed $U_{flutter} = 7(m/s)$ in nominal condition, which drops down to $5(m/s)$ when the simulated failure is applied. The trust region of the quasi-steady aerodynamic model stays within a range of angle of attack up to 10 degrees. For this reason, the wind speed increment and the structural stiffness reduction are modulated so that the resulting LCOs motion is bounded within the valid angle of attack domain. In particular, failure is simulated by a 50% reduction of the stiffness matrix $K_{nominal}$. The post-flutter velocity is imposed

Table 4.1: Simulation Cases

	Case 1-2	**Case 3-4**	**Case 5-6**	**Case 7**
$U_{C.L.}$ (m/s)	7	7	9	9
K (% of K_{nom})	100%	50%	100%	50%
t_{ON}	0-10	0-10	0-10	0
$U_{flutter}$ (m/s)	7	5	7	5

30% higher than the flutter speed, $U_{post-flutter} = 9(m/s)$. The features of the model free dynamic motion, in the design and off-design proposed conditions, are reported and discussed in Chapter 2. Testing and verification of the adaptive control schemes is carried out by perturbing the aeroelastic system with an initial pitch angle $\alpha = 0.1(rad) = 5.73(deg)$ and monitoring the controller as well as the plunging and pitching response evaluated in the simulation environment. Despite the large number of performed simulations, only the most meaningful cases are reported and discussed. They are summarized in Table 4.1, where each case is characterized by the closed-loop wind speed U_{CL}, the plant stiffness matrix value K, the controller activation time t_{ON} and the open-loop flutter speed $U_{flutter}$ of the actual configuration. The two different activation time instants serve to evaluate the controller capability of suppressing flutter from LCOs established regime ($t_{ON} = 10$) or not. It is noticed that, for the combined post-flutter and reduced stiffness condition (case 7), the system is controlled only at 0 sec to avoid unreasonable values of the pitch angle. The numerical integration in all the simulations is performed using a fourth-order Runge-Kutta with a sampling time $t_s = 0.001(sec)$.

Firstly, the overall test campaign reported in the following figures shows that the problem is well posed since all the adaptive schemes are able to control the system, independently from the activation time of the controller (LCOs established or not). The robustness and adaptive capabilities of each individual control scheme are hereafter discussed. Despite the significant variations in the aeroelastic system dynamics (in terms of LCOs frequency and amplitude) due to the imposed initial conditions, the convergence time of each control scheme remains satisfactory. However, the two *Modified* control schemes exhibit a small performance deterioration when activated from an LCO established regime. Viceversa, the standard MRAC, as expected, shows slow adaptation rate and subsequently poor performance in time domain, regulating the plant in about 10 sec, when activated at time zero (Figure 4.2a, Figure 4.3a, Figure 4.4a and Figure 4.5). On the other hand, the standard MRAC scheme exhibits a faster behavior, converging in about 1 sec, when activated at time 10 sec, with fully established LCOs (Figure 4.2b, Figure 4.3b and Figure 4.4b). This is due to the presence,

in this last condition, of a higher $\dot{\alpha}$ that enriches the feedback signal, reducing the convergence time. A quite similar response is observed for the standard L_1 control scheme, as illustrated from Figure 4.10a to Figure 4.13. The only perceivable difference, from the standard MRAC response, is the introduction of high frequency oscillations in the control signal, as clearly noticeable in Figure 4.10a, Figure 4.11a, Figure 4.12a and Figure 4.13, when the controller is active at time zero. These oscillations derive from the adaptive law computation algorithm, as shown in Figure 4.1. The cause of these oscillations is the extremely high value of the adaptive gain Γ that makes the differential equation too stiff to be solved with a reasonable discrete time integration step. Thus, the unknown parameters solution oscillates, constrained by the *proj* operator bounds, and propagates mildly damped by the filter and the system dynamic, in the observed state. The same behavior is noticeable in both the L_1 scheme, sensibly worse for the modified L_1 where convergence of the unknown parameters is never reached. However, the filter of the modified L_1 has a more narrow passing band which prevent the oscillation to propagate up to the states through the control signal command. For the standard L_1 the oscillation propagation is reduced for LCO induced conditions, when activation time is at 10 sec, always for the presence of a higher $\dot{\alpha}$ which helps the adaptation law to converge faster. In addition, it is worth pointing out that, for both the L_1 adaptive control schemes, the adaptive law needs to be constantly fed by the plant observable states, $x_{obs} = [\alpha \quad \dot{\alpha}]$, even if the control signal is not passed through the plant. On the contrary, the MRAC schemes do not need to stay connected to the plant to make the adaptive parameters evolve, as in the previous case. This is also a contributory cause to the unexpected better performance of the L_1 controller when activated at 10 seconds with LCO established. In fact, after ten seconds from the controller activation, the adaptive parameter estimation has almost reached convergence to the real solution. Figure 4.6a through Figure 4.9 report the system response and the control command time-histories when the plant is controlled by the Modified MRAC scheme. This control law shows a fast, about 1.5 sec, and robust response that does not depend on the activation time. The states' trajectory to the stationary condition depends on the states' value at the activation time instant. Smooth convergence of the adaptive parameters estimation is verified through the entire simulation test campaign; Figure 4.1 is an example. A drawback of the Modified MRAC scheme is that it has the highest overshoot among the four control methods, so that command saturation is often reached (Figure 4.6a through Figure 4.9, subplots (e)). This is caused by the adjunct control signal u_a of Equation (3.14), whose primary function is to enrich the signal for faster response and reduced tracking error. As far as the improved L_1, is concerned Figure 4.14a through Figure 4.17 must be analyzed. The response is clearly improved, in terms of time to regulate the system, with respect to the standard L_1 scheme considered. In addition,

the dynamic behavior as a function of the activation time is opposite to the standard L_1, so it deteriorates if activated at $t = 10(sec)$. Moreover, it shows an unexpected high sensitivity to wind speed and structural stiffness, with a noticeable steady state tracking error, as shown in Figure 4.17 for case 7. This behavior is due to the very narrow band of the filter which is designed and optimized for nominal plant condition. The narrowness of the filter passing band is associated, in this case, to the high order of the filter which introduces tuning issues and loss in adaptivity. However, the so designed filter is beneficial to prevent the propagation of the high frequency oscillations through the states. To conclude, the Standard MRAC and the two L_1 control schemes exhibit reduced robustness with respect to the Modified MRAC scheme, which can be faster or slower depending on the activation time, or more properly depending on the actual state values at the controller activation. This inconsistent behavior is also due to the dependency of the unknown parameters estimation law from the state error values ($e(t)$ for the MRAC schemes or $\tilde{x}(t)$ for the L_1). The closer the actual states are to the reference model or the estimated states, the faster is the response. This is a common behavior for any reference model control architecture, but it is strongly reduced in the Modified MRAC scheme by the employment of the enriching signal u_a.

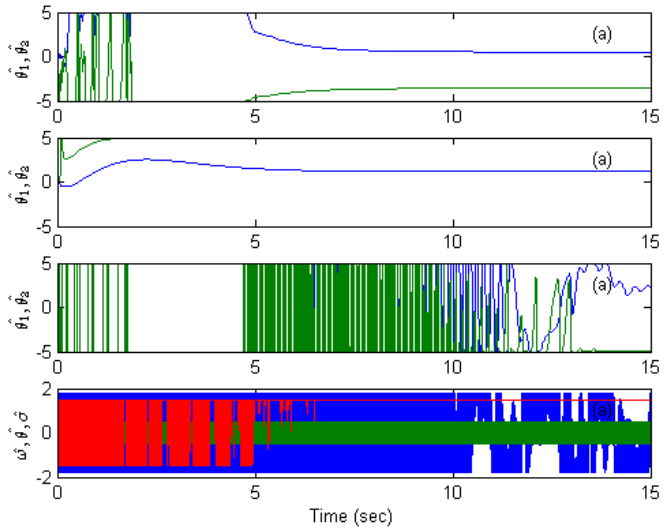

Figure 4.1: Example of unknown parameters estimation convergence. Flight condition case 1: Flutter speed and Nominal stiffness. a) Standard MRAC; b) Modified MRAC; c) Standard L_1; d) Modified L_1

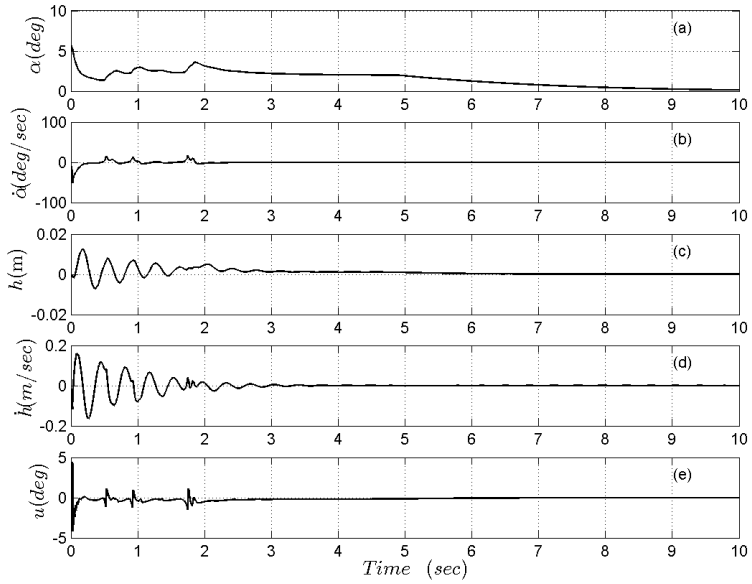

(a) Standard MRAC time response, simulation case 1

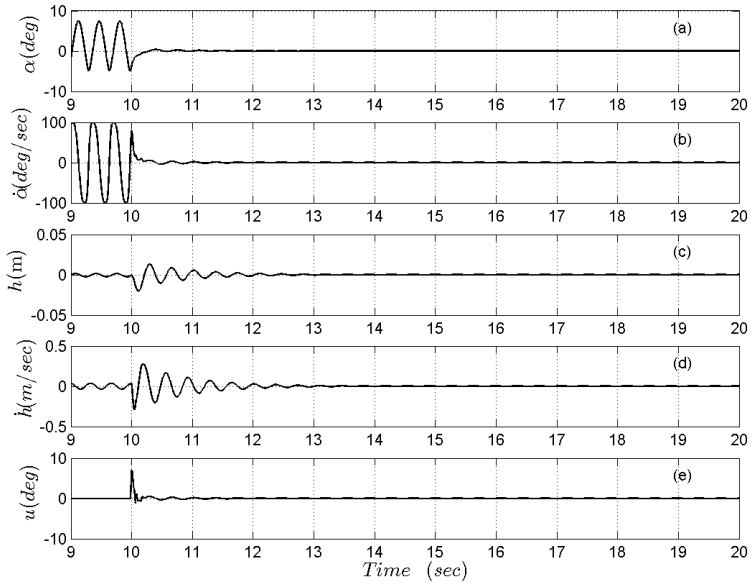

(b) Standard MRAC time response, simulation case 2

Figure 4.2: Standard MRAC time response, simulation case 1-2

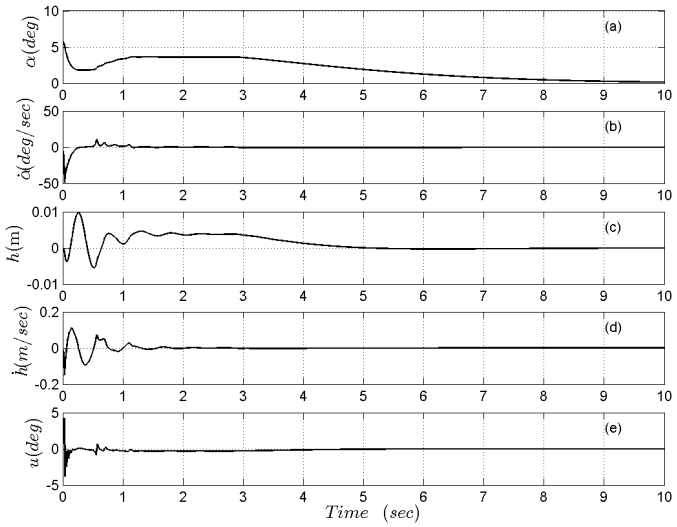

(a) Standard MRAC time response, simulation case 3

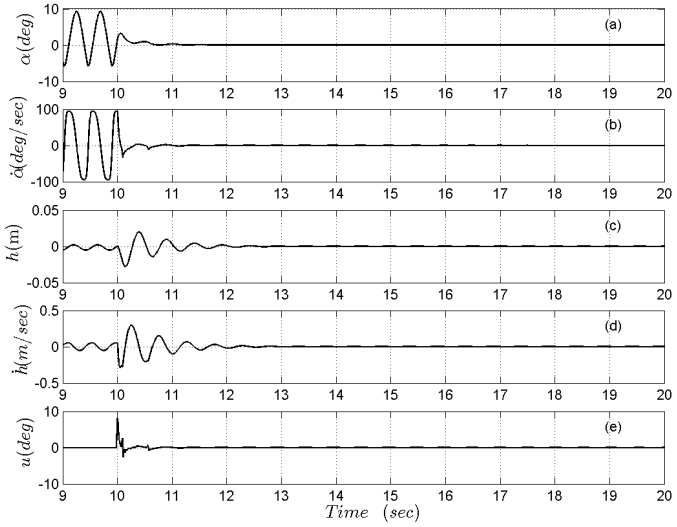

(b) Standard MRAC time response, simulation case 4

Figure 4.3: Standard MRAC time response, simulation case 3-4

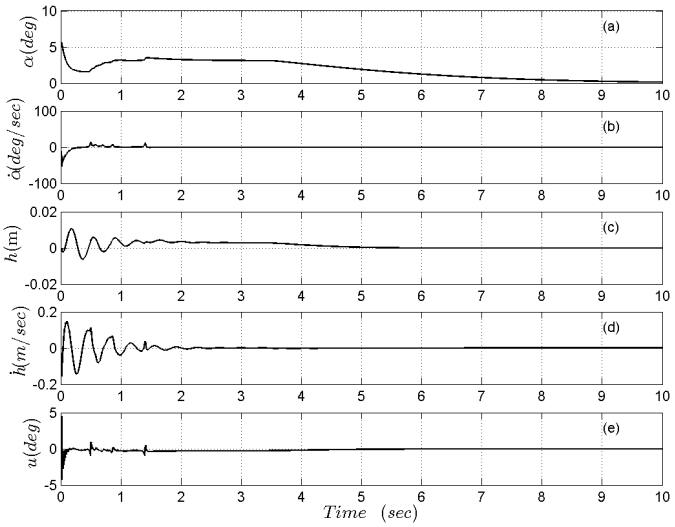

(a) Standard MRAC time response, simulation case 5

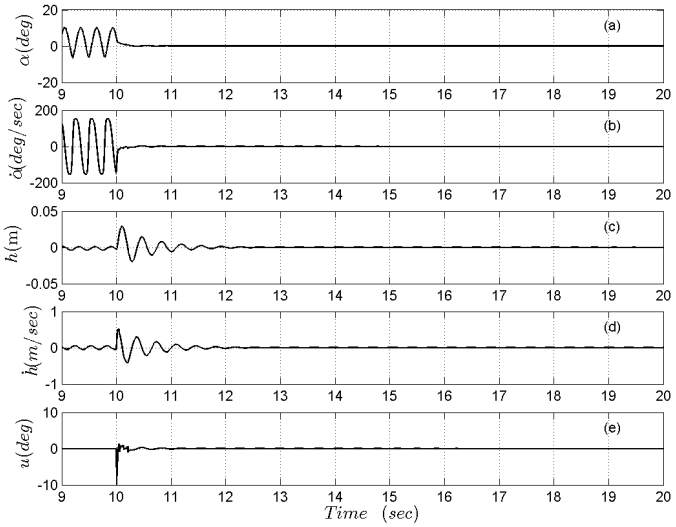

(b) Standard MRAC time response, simulation case 6

Figure 4.4: Standard MRAC time response, simulation case 5-6

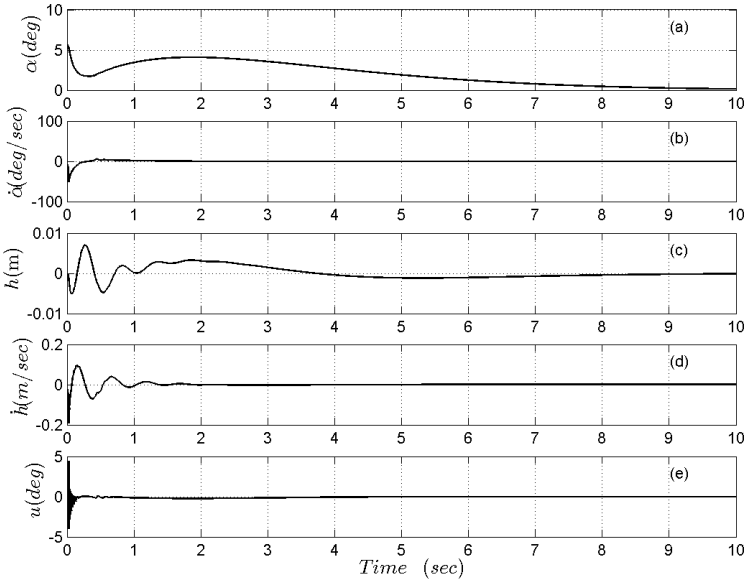

Figure 4.5: Standard MRAC time response, simulation case 7

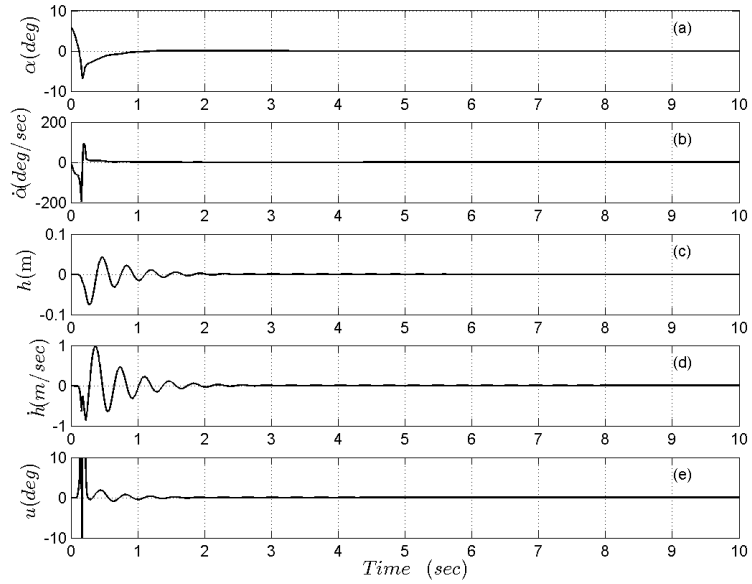

(a) Modified MRAC time response, simulation case 1

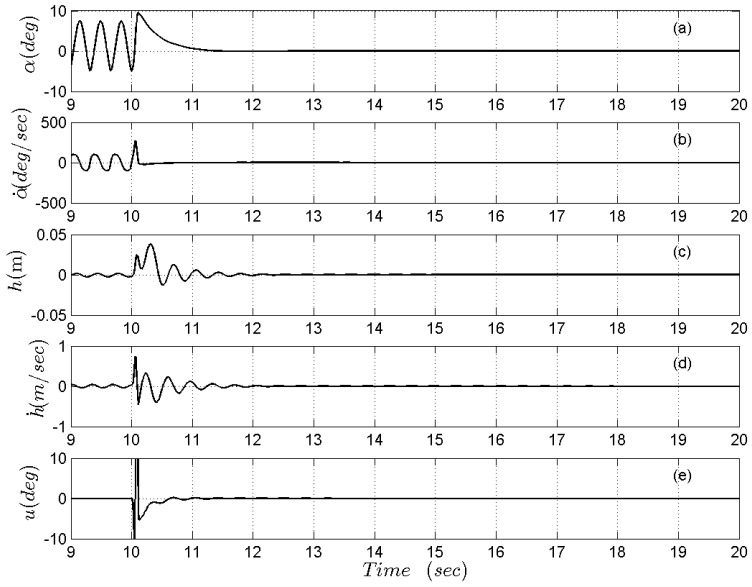

(b) Modified MRAC time response, simulation case 2

Figure 4.6: Modified MRAC time response, simulation case 1-2

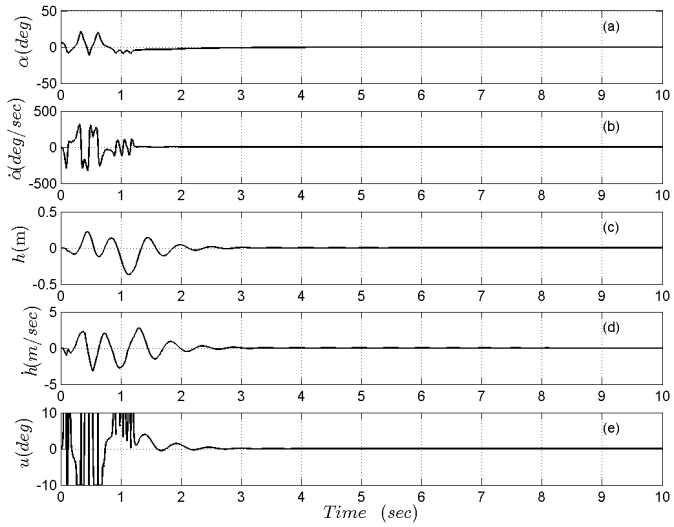

(a) Modified MRAC time response, simulation case 3

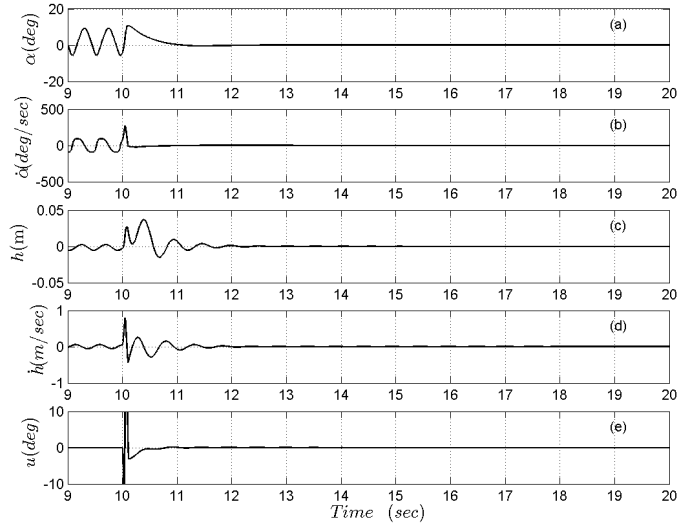

(b) Modified MRAC time response, simulation case 4

Figure 4.7: Modified MRAC time response, simulation case 3-4

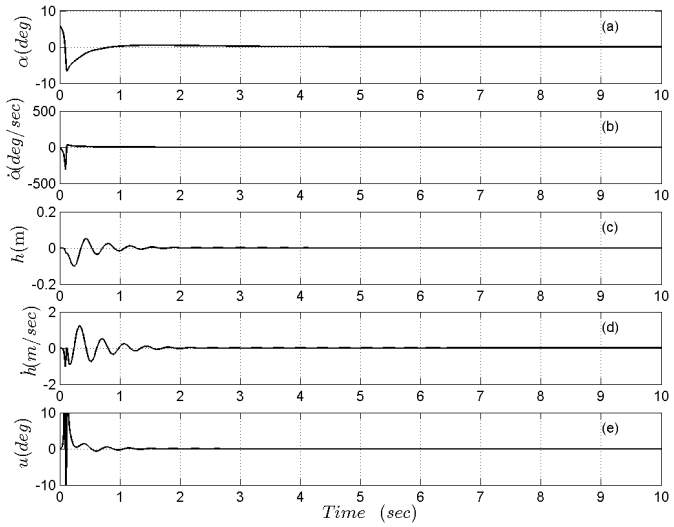

(a) Modified MRAC time response, simulation case 5

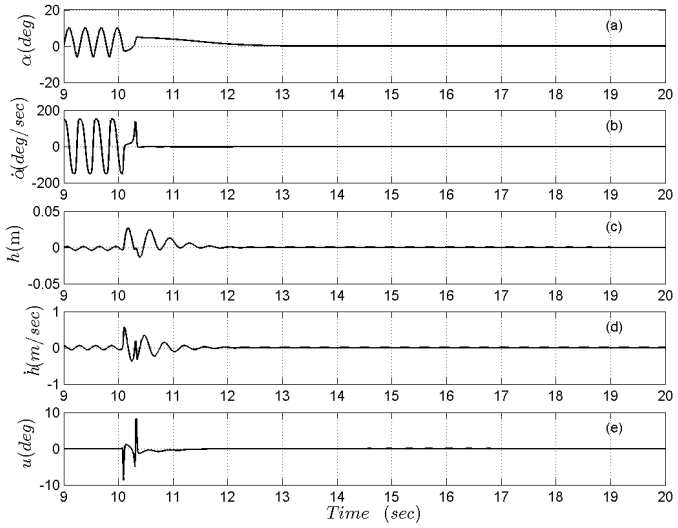

(b) Modified MRAC time response, simulation case 6

Figure 4.8: Modified MRAC time response, simulation case 5-6

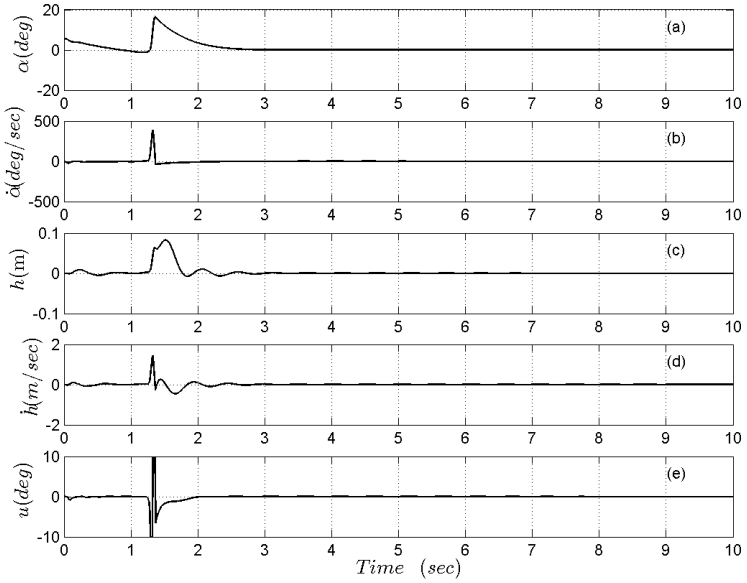

Figure 4.9: Modified MRAC time response, simulation case 7

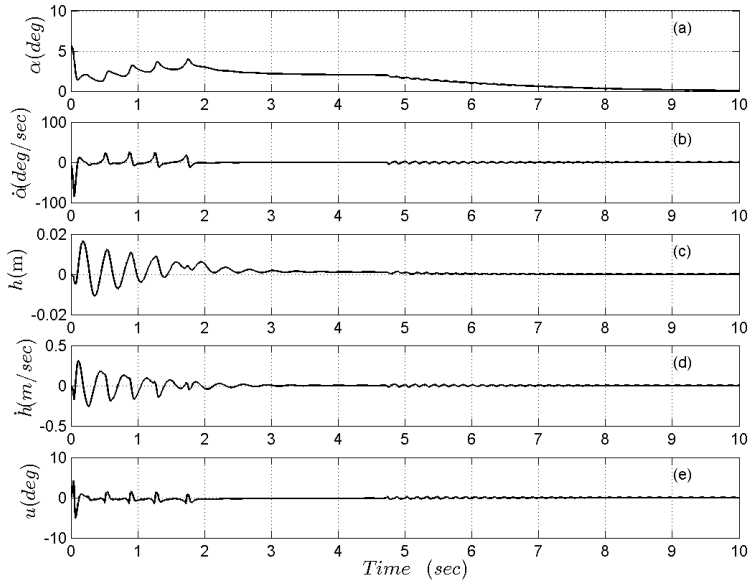

(a) Standard L1 time response, simulation case 1

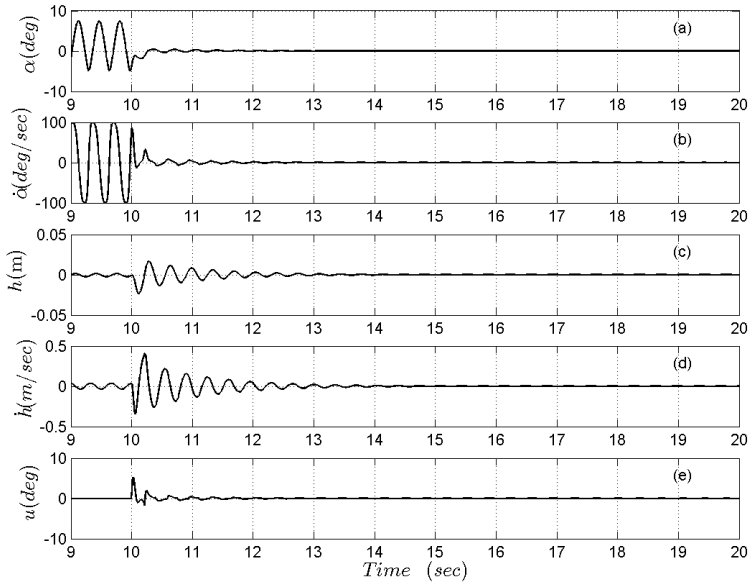

(b) Standard L1 time response, simulation case 2

Figure 4.10: Standard L1 time response, simulation case 1-2

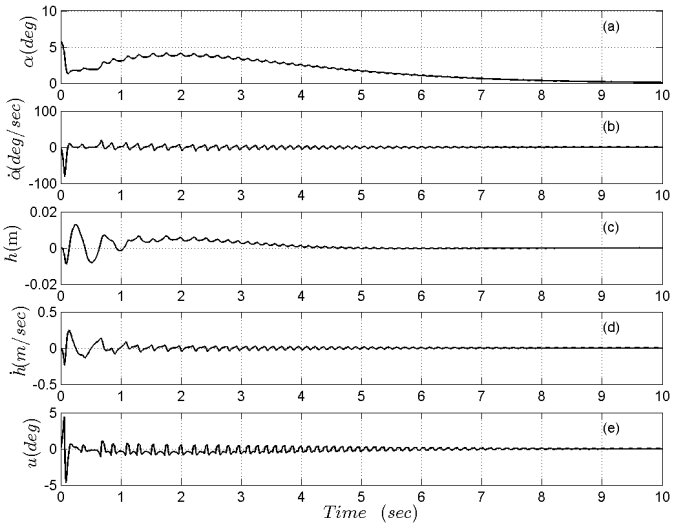

(a) Standard L1 time response, simulation case 3

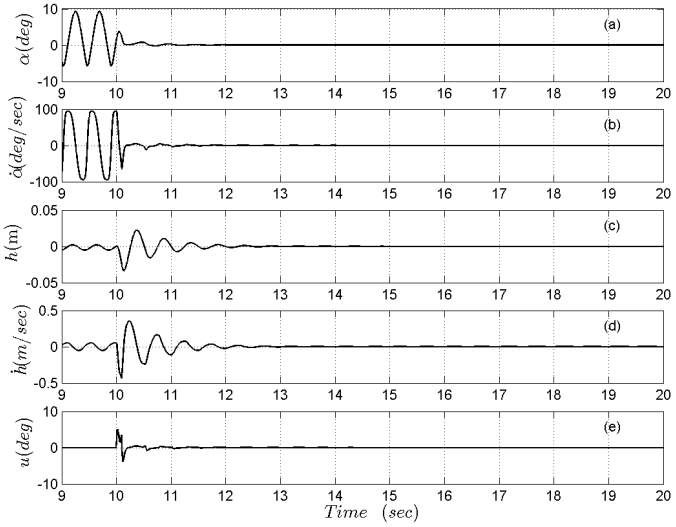

(b) Standard L1 time response, simulation case 4

Figure 4.11: Standard L1 time response, simulation case 3-4

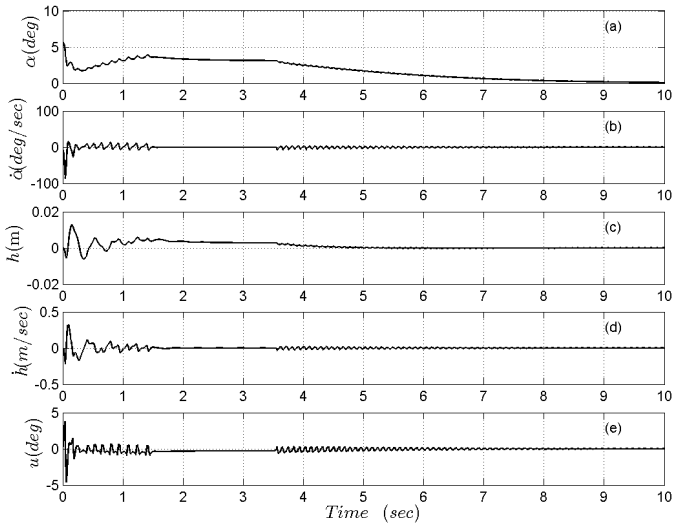

(a) Standard L1 time response, simulation case 5

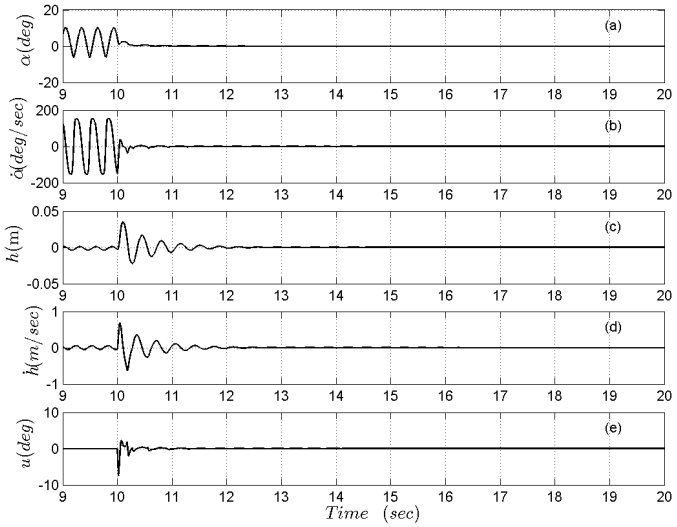

(b) Standard L1 time response, simulation case 6

Figure 4.12: Standard L1 time response, simulation case 5-6

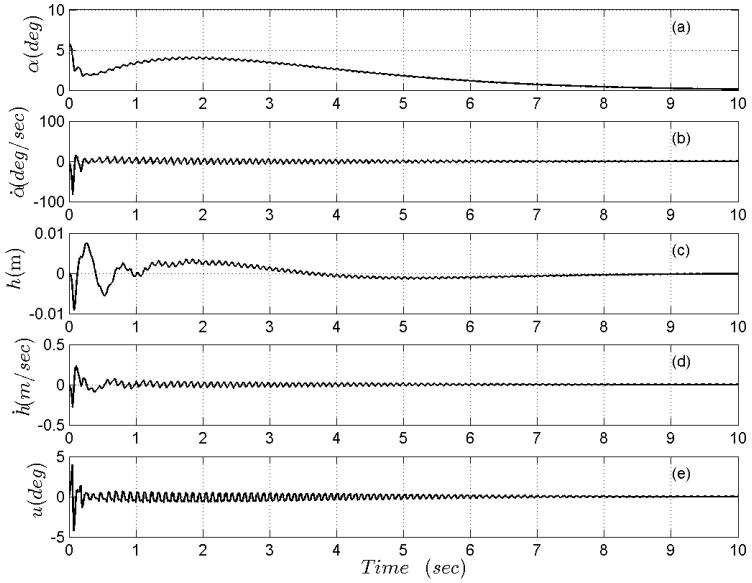

Figure 4.13: Standard L1 time response, simulation case 7

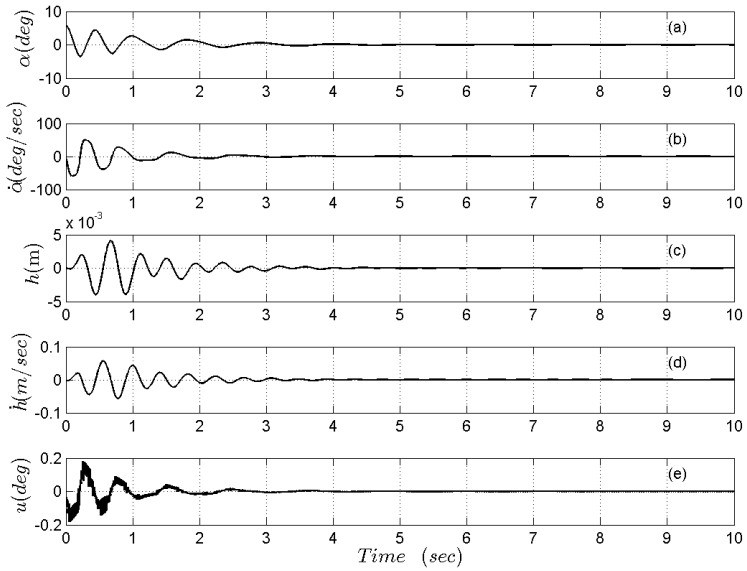

(a) Modified L1 time response, simulation case 1

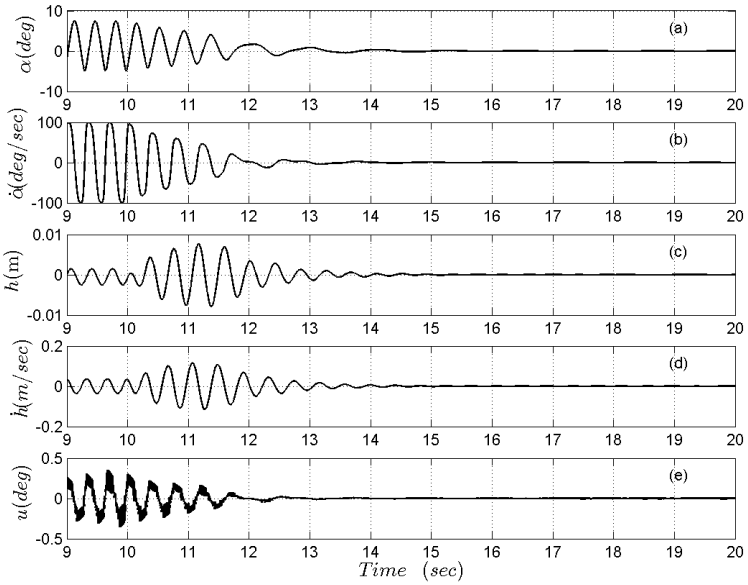

(b) Modified L1 time response, simulation case 2

Figure 4.14: Modified L1 time response, simulation case 1-2

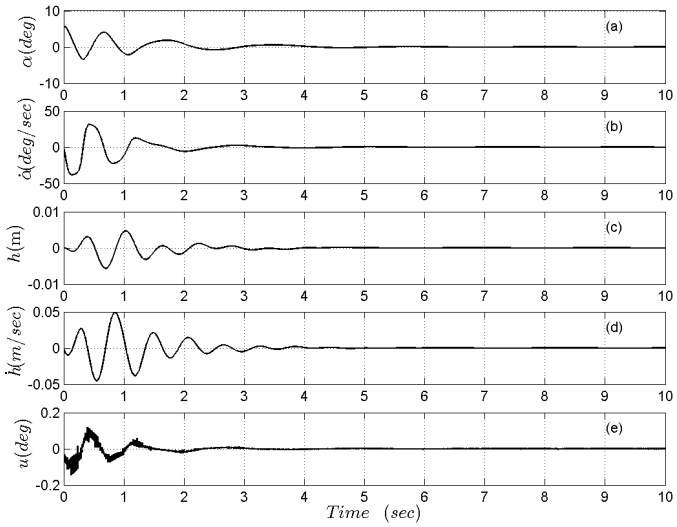

(a) Modified L1 time response, simulation case 3

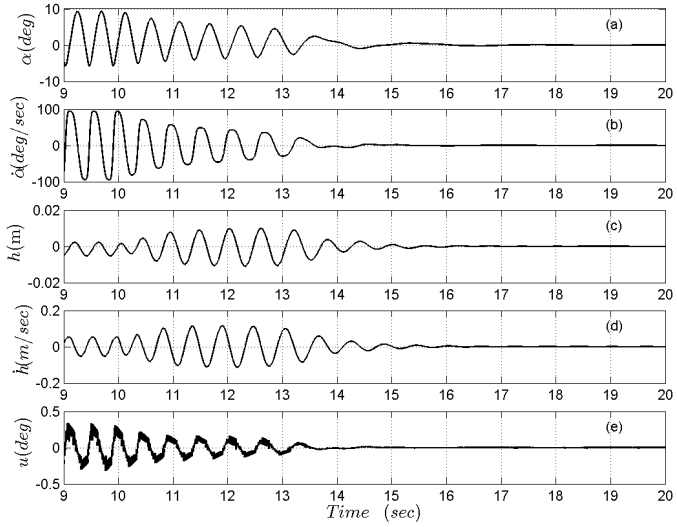

(b) Modified L1 time response, simulation case 4

Figure 4.15: Modified L1 time response, simulation case 3-4

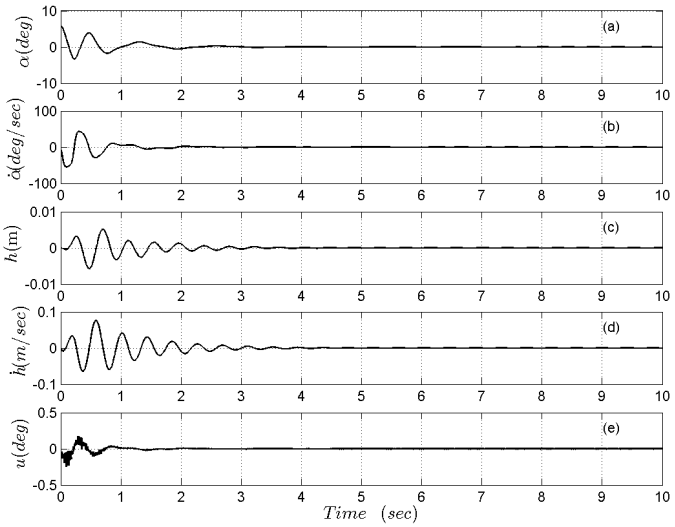

(a) Modified L1 time response, simulation case 5

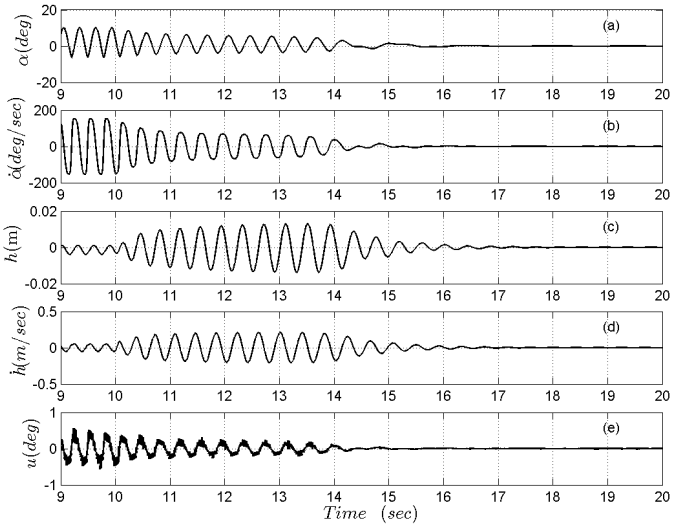

(b) Modified L1 time response, simulation case 6

Figure 4.16: Modified L1 time response, simulation case 5-6

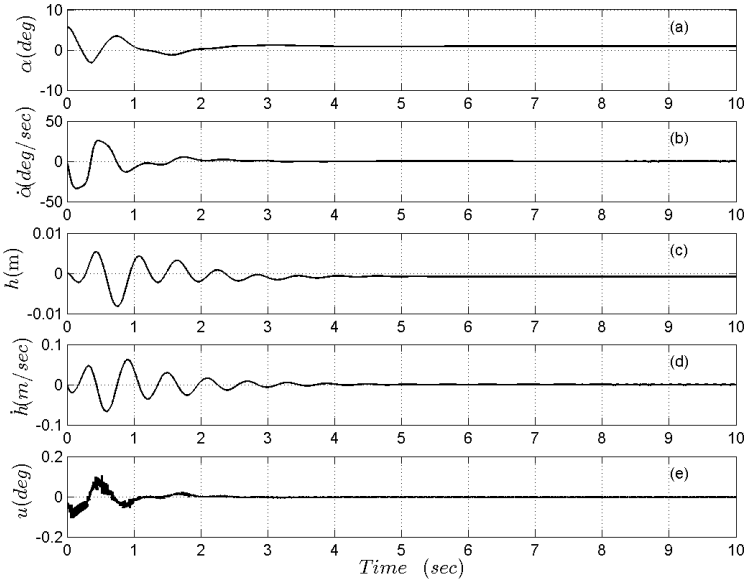

Figure 4.17: Modified L1 time response, simulation case 7

Table 4.2: Gust Analysis: Simulation Cases

	Case 1-3	**Case 4-6**	**Case 7-9**
$U_{C.L.}$ (m/s)	7	7	9
K (% of K_{nom})	100%	50%	50%
Gust type	$a), b), c)$	$a), b), c)$	$a), b), c)$

4.2 Flutter Suppression Despite Gusts Loads: Wing-Flap Configuration

To verify the disturbance rejection capabilities of the implemented control schemes, numerical simulations are repeated to include external gusts. As previously described in Section 2.2.3, and shown in Figure 2.17, the applied gusts have the following trend: a) exponential, b) combined random and sinusoidal and c) triangular gusts. The closed-loop system response is monitored by observing the time histories of the angle of attack, that is the controlled state as well as the variable on which the disturbance is primarily acting. The presented results are gathered for control scheme typology. Hence, first the response of the standard and modified MRAC schemes are collected and reported, followed by the standard and modified L_1. For a comprehensive analysis, the aeroelastic model has been tested at three critical conditions: nominal, reduced stiffness solely and post-flutter combined with reduced stiffness. This makes a total amount of nine test cases reported as in Table 4.2. Controller activation is always triggered at time zero. Figure 4.18 and Figure 4.19a first demonstrate the higher robustness and fastness of the modified MRAC scheme w.r.t. the standard one. Analyzing the different subplots for each condition, it can be noticed how the modified scheme is less sensitive to the gust typology applied. On the contrary, the standard MRAC scheme reflects the gust trend, exhibiting residual oscillations when combined sinusoidal and random gust is applied (case b), or an higher peak when triangular gust is active (case c)) and a longer convergence time for exponential gust (case a)). What impacts more the modified scheme response is the variation of the flight condition, making the regulation slightly slower going from Figure 4.18a to Figure 4.19a. As far as the two L_1 schemes are concerned, Figure 4.20 and Figure 4.20b, the same consideration can be drawn. The residual oscillation effect is even more noticeable, because amplified by the intrinsic oscillation propagation phenomenon discussed in Section 4.1. On the other hand, the modified L_1 scheme, while better absorbing the gust action, in terms of residual oscillation, responds with a steady-state error of about $1(deg)$, as shown in Figure 4.20b. This effect must be related to the already discussed filter position in the control scheme, located exactly after the control signal computation.

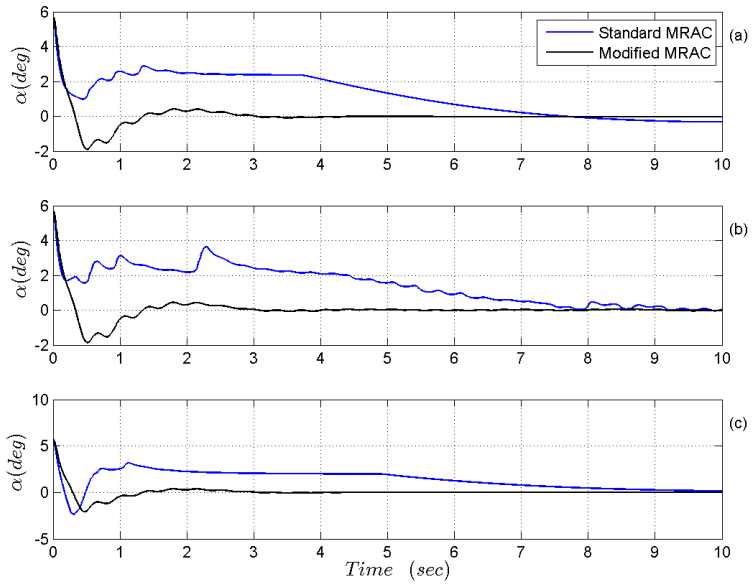

(a) MRAC schemes response to gust at flutter speed and nominal stiffness, angle of attack time histories: a) exponential gust applied; b) random and sinusoidal gust applied; c) triangular gust applied.

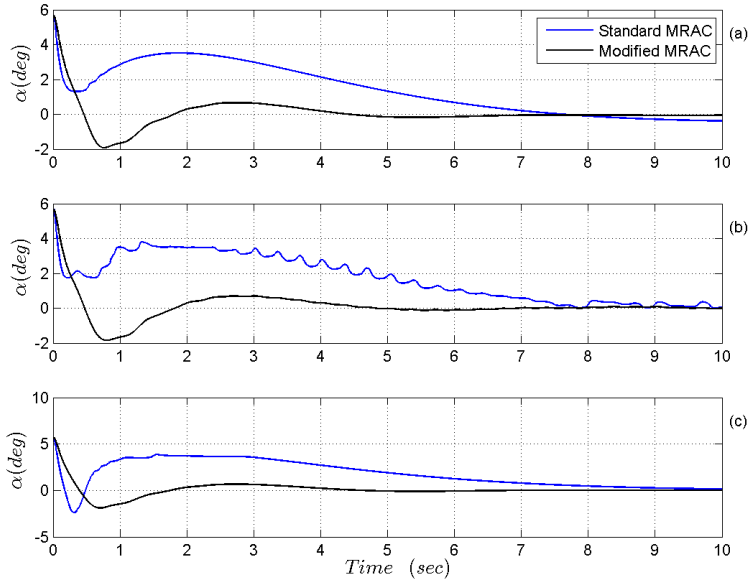

(b) MRAC schemes response to gust at flutter speed with reduced stiffness, angle of attack time histories: a) exponential gust applied; b) random and sinusoidal gust applied; c) triangular gust applied.

Figure 4.18: MRAC schemes response to gust, cases 1-6

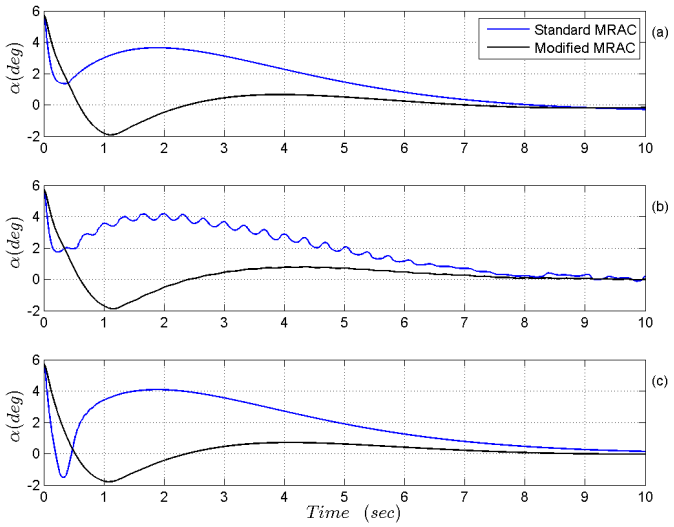

(a) MRAC schemes response to gust at post flutter speed with reduced stiffness, angle of attack time histories: a) exponential gust applied; b) random and sinusoidal gust applied; c) triangular gust applied.

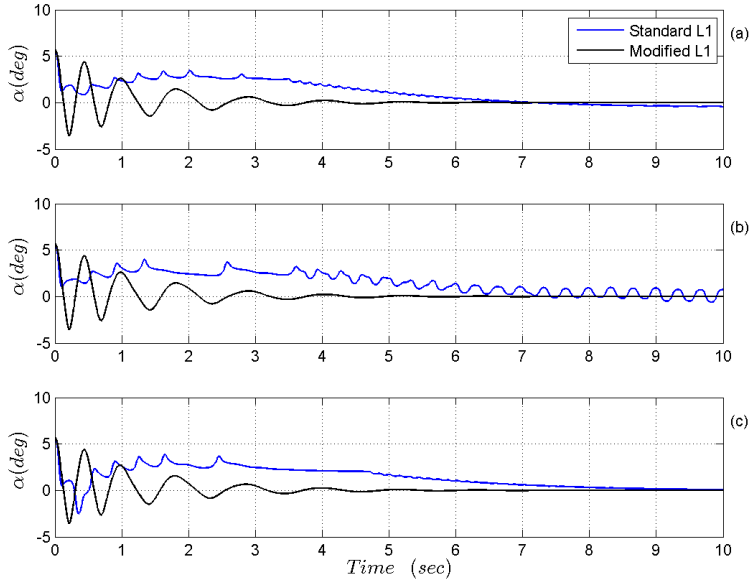

(b) L1 schemes response to gust at flutter speed and nominal stiffness, angle of attack time histories: a) exponential gust applied; b) random and sinusoidal gust applied; c) triangular gust applied.

Figure 4.19: MRAC schemes response to gust, cases 1-6. L1 schemes response to gust, cases 1-3

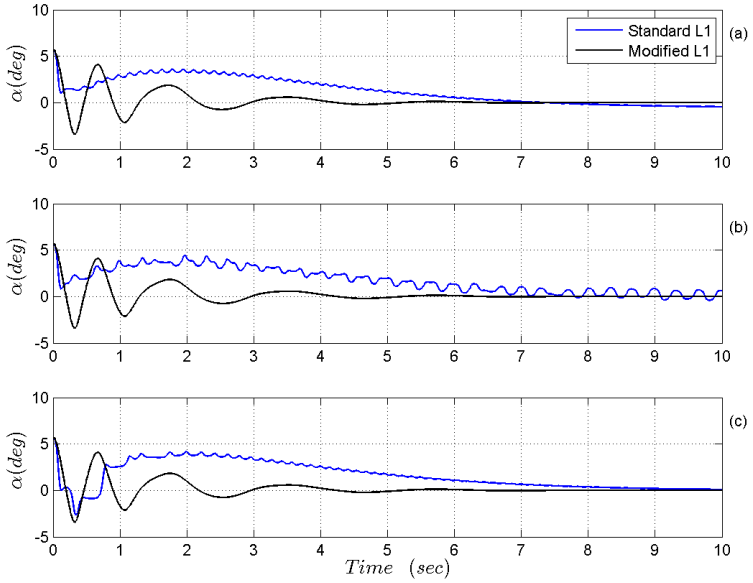

(a) L1 schemes response to gust at flutter speed with reduced stiffness, angle of attack time histories: a) exponential gust applied; b) random and sinusoidal gust applied; c) triangular gust applied.

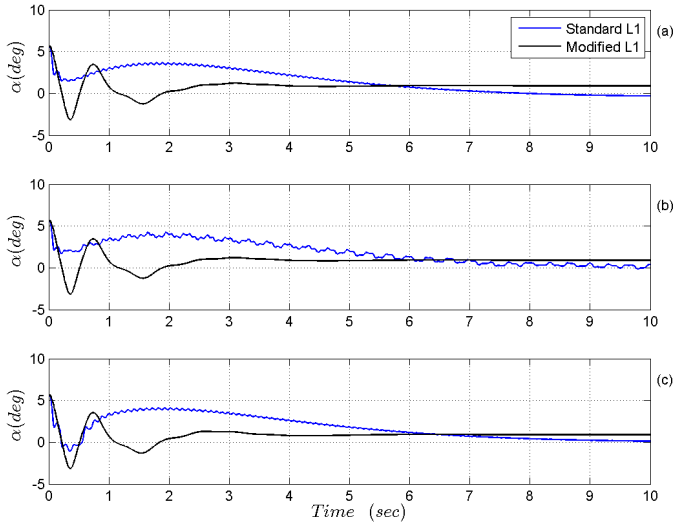

(b) L1 schemes response to gust at post flutter speed with reduced stiffness, angle of attack time histories: a) exponential gust applied; b) random and sinusoidal gust applied; c) triangular gust applied.

Figure 4.20: L1 schemes response to gust, cases 4-9

4.3 Flutter Suppression for the Wing-Spoiler Configuration

The aeroelastic model modified to account for the novel spoiler actuation system and coupled to the modified MRAC has been tested, for scientific consistency, by following the same test case definition and procedure used for the trailing-edge flap configuration, Table 4.1. It is worth stressing that the modified MRAC scheme is maintained the same of the other configuration, with the simple addition of a *round* operator on the control law output signal, which is the actual number of spoilers to open. The results are presented in the same form as before: for each test case the state variable $[\alpha \quad h]$, their derivatives $[\dot{\alpha} \quad \dot{h}]$ and the control signal time histories are recorded and analyzed. Figure 4.21a to Figure 4.24 highlight that the problem is well posed and the aeroealstic system belongs to the class of plant controllable by the modified MRAC scheme applied. This is verified by performing a wide set of simulations where convergence is always reached. The regulation takes place with a smooth and constantly decreasing motion, even if the response is slower if compared to the trailing-edge flap actuation system. This is a consequence of the single-side action of the spoilers, as the implemented aeroelastic model refers to the wing section designed and prototyped (see Chapter 5), where the stripe of multiple spoiler is installed only on the wing upper surface. Albeit slower, the regulation time of about 2 seconds remains acceptable considering the low frequency flutter phenomena for which this actuation solution has been thought. The subplots denoted by the letter e) of Figure 4.21a to Figure 4.24, show the time histories of the control signal, which is made up of discrete values, between 0 and 5, representing the actual number of open spoilers. This is obtained by bounding the signal with a saturation operator and explains the discontinuities encountered in the time histories. One additional effect of the rounding operation is that for $u < 0.5$ the control law output is floored to zero, which means none of the spoiler is active. This happens when the angle of attack α is at very small values and close to be fully regulated. For this reason, the actuation dead-zone does not have any impact on convergence, that is only postponed by a little delay. However, the dead-zone actuation issue can be easily overtaken by allowing gradual, and not binary, operation to at least the first open spoiler (that is #3), as explained in Chapter 5. The results' analysis demonstrates the robustness of the combined spoiler-Modified MRAC control architecture. In fact, the regulation time remains almost constant in all the seven test cases. Whereas an unexpected beneficial effect on the control performance due to the stiffness reduction and post-flutter wind speed is detected. This phenomenon derives from the higher effectiveness of each spoiler when higher amplitude oscillations and faster wind condition occurs.

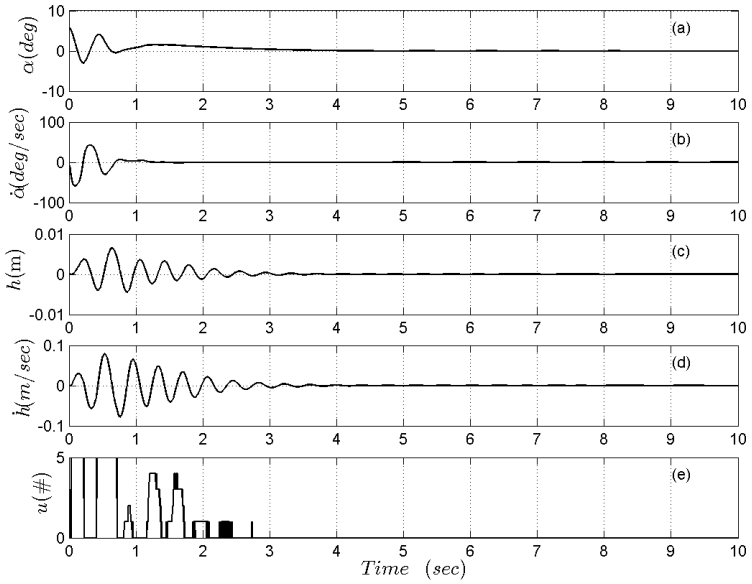

(a) Spoiler/MRAC configuration time response, simulation case 1

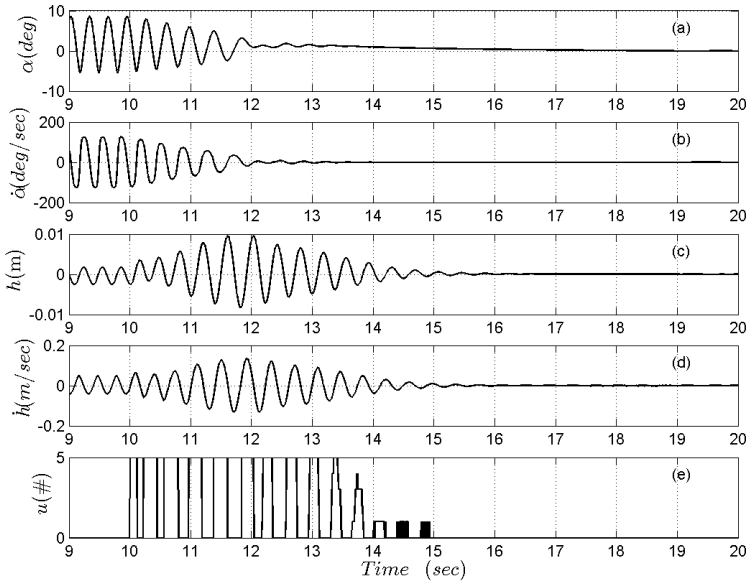

(b) Spoiler/MRAC configuration time response, simulation case 2

Figure 4.21: Spoiler/MRAC configuration time response, simulation case 1-2

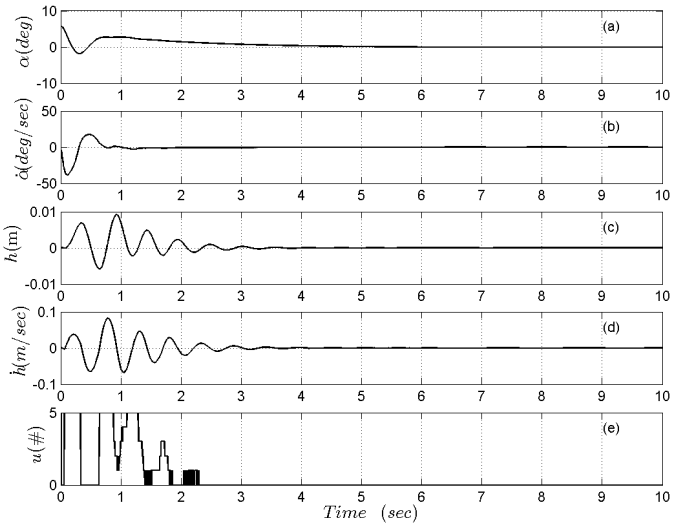

(a) Spoiler/MRAC configuration time response, simulation case 3

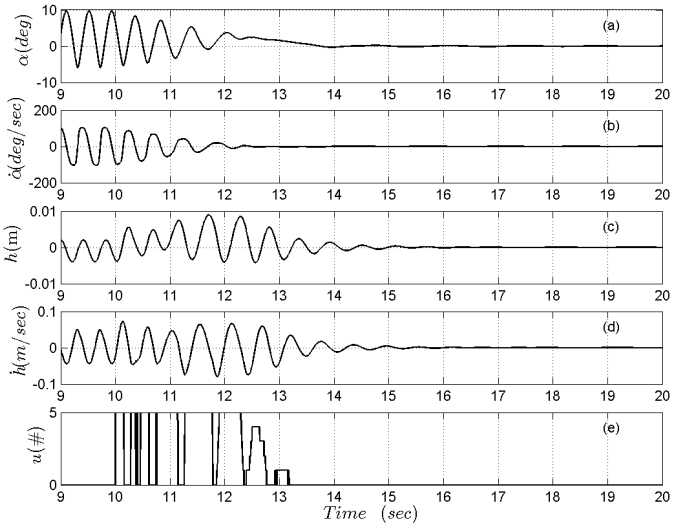

(b) Spoiler/MRAC configuration time response, simulation case 4

Figure 4.22: Spoiler/MRAC configuration time response, simulation case 3-4

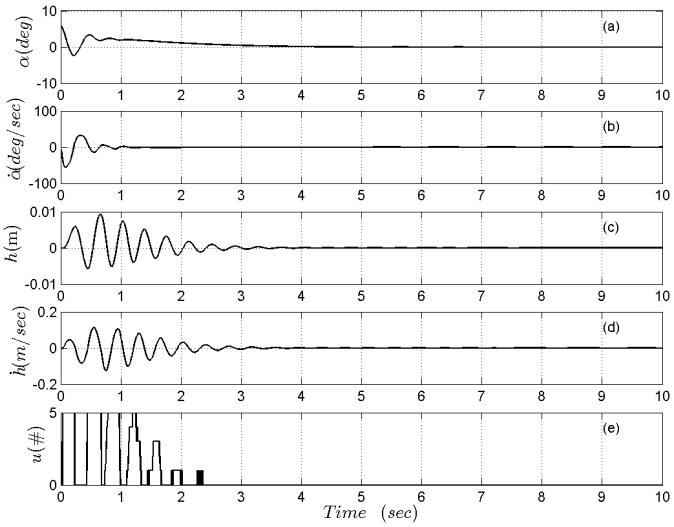

(a) Spoiler/MRAC configuration time response, simulation case 5

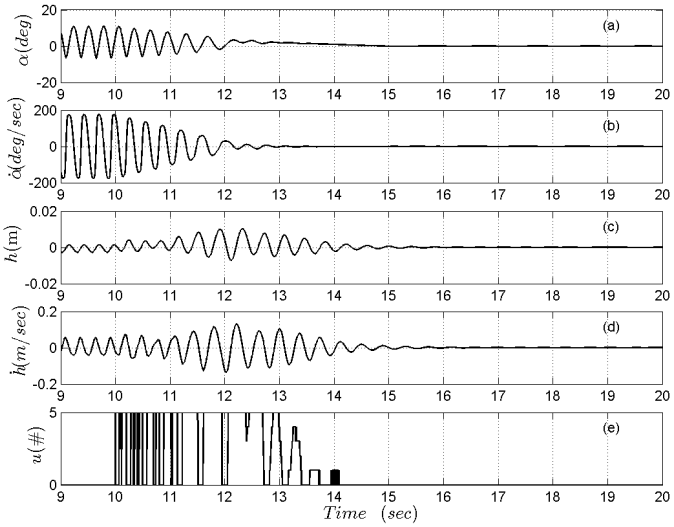

(b) Spoiler/MRAC configuration time response, simulation case 6

Figure 4.23: Spoiler/MRAC configuration time response, simulation case 5-6

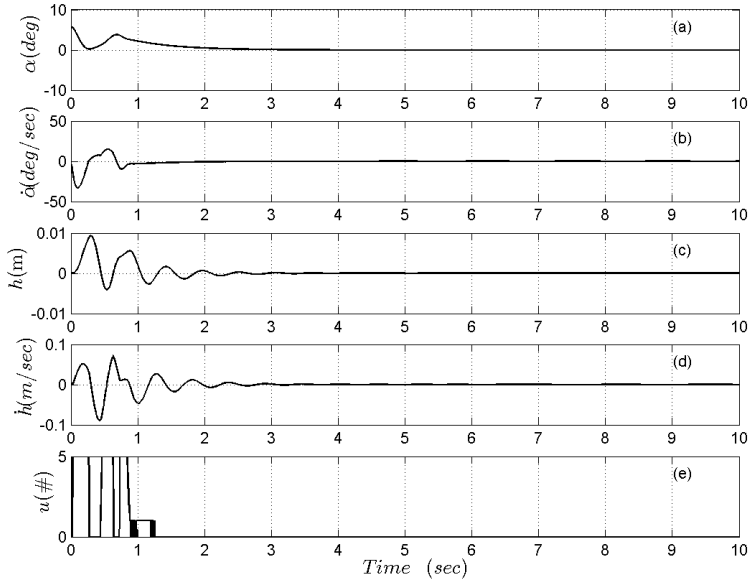

Figure 4.24: Spoiler/MRAC configuration time response, simulation case 7

4.4 Flutter Suppression Despite Gusts Loads: Wing-Spoiler Configuration

The disturbance rejection capabilities of the Spoiler/MRAC control architecture are verified using the same strategy described in Section 4.2. In this case time histories of the two states and the control signal are reported separately as comparison is not required. The pitch angle α is shown from Figure 4.25 to Figure 4.26b, the plunge displacement h from Figure 4.27a to Figure 4.28a and the control signal u from Figure 4.28b to Figure 4.29b. Each of the three subplots $a), b)$ and $c)$ is referred to the corresponding gusts described in Chapter 2, Section 2.2.3. The results show a very robust behavior inferable from the negligible influence during transient of the different gusts applied and regulation to zero is correctly reached. A closer look to the recorded responses reveals a very small delay to reach the zero value when exponential gust is applied (case a)), a slightly higher absolute values for the first peak when triangular gust is selected (case c)) and only for the combined sinusoidal-random gust some, more noticeable, residual oscillation around zero can be noticed (case b)). This effect derives, as explained in Section 4.3, from the rounding operation that transform the control signal into a discrete number of opened spoilers, generating a dead-zone in which the controller does not work. It is true that gradual and proportional opening motion, only for the first spoiler, will immediately solve the issue that is related to the conceived opening strategy. Robustness with respect to the changes in the wing operational condition is confirmed.

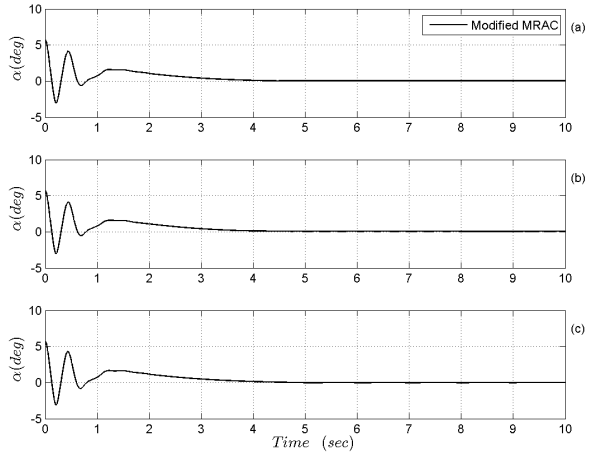

Figure 4.25: Spoiler/MRAC configuration flutter control response to gust, at flutter speed and nominal stiffness, pitch angle time histories

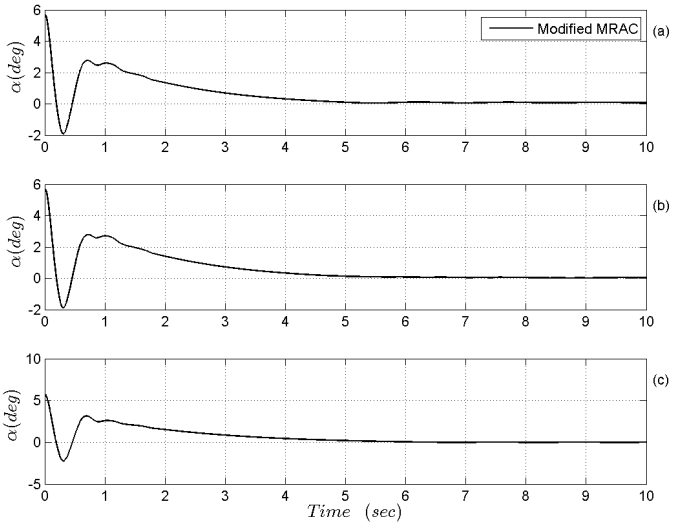

(a) Spoiler/MRAC configuration flutter control response to gust, at flutter speed and reduced stiffness, pitch angle time histories

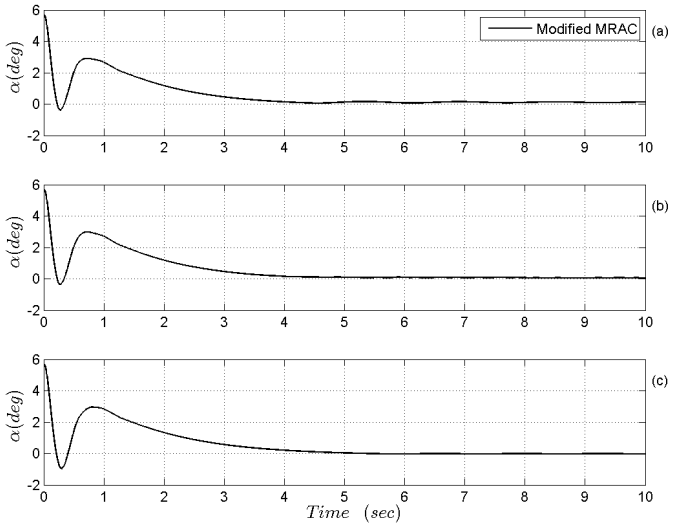

(b) Spoiler/MRAC configuration flutter control response to gust, at post flutter speed and nominal stiffness, pitch angle time histories

Figure 4.26: Spoiler/MRAC configuration flutter control response to gust

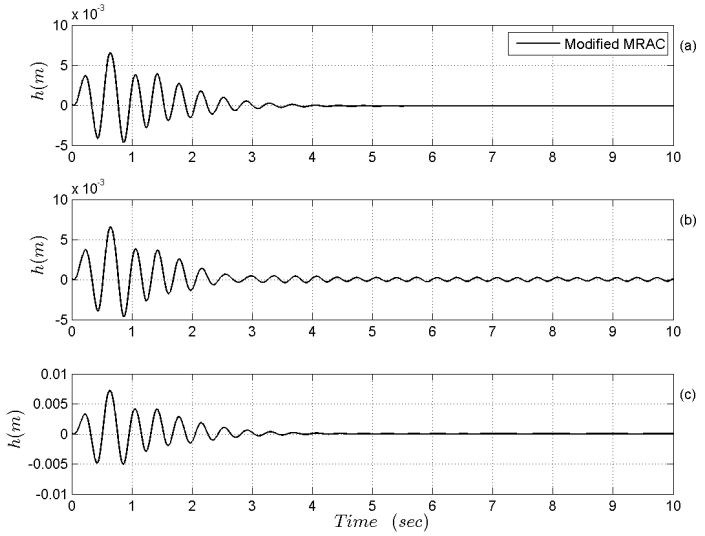

(a) Spoiler/MRAC configuration flutter control response to gust, at flutter speed and nominal stiffness, plunge displacement time histories

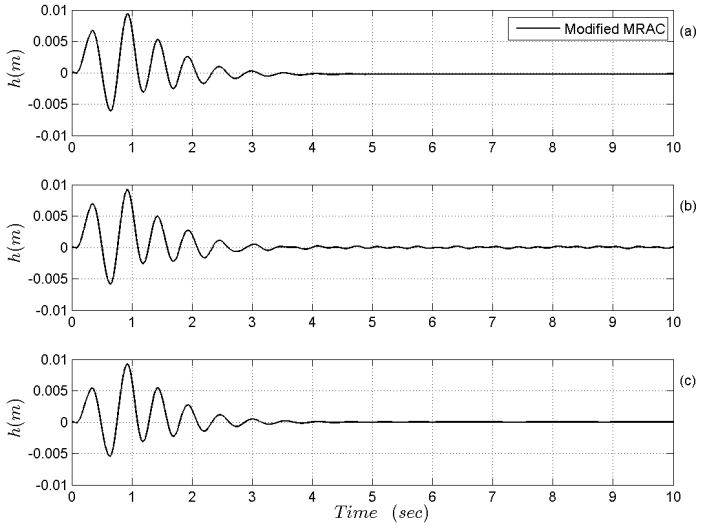

(b) Spoiler/MRAC configuration flutter control response to gust, at flutter speed and reduced stiffness, plunge displacement time histories

Figure 4.27: Spoiler/MRAC configuration flutter control response to gust

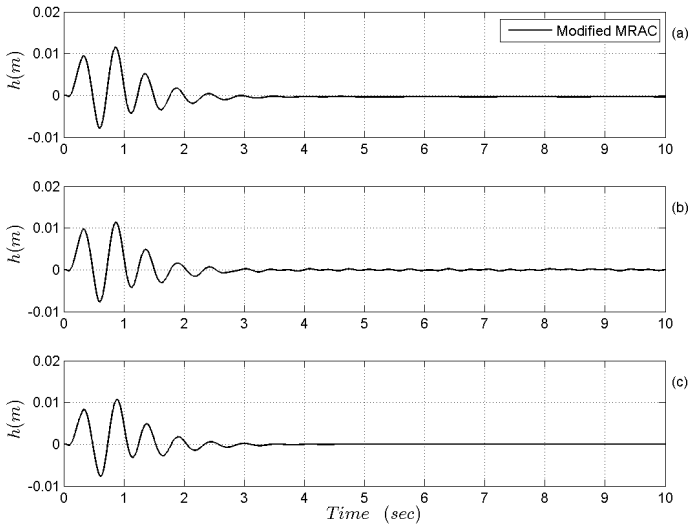

(a) Spoiler/MRAC configuration flutter control response to gust, at post flutter speed and reduced stiffness, plunge displacement time histories

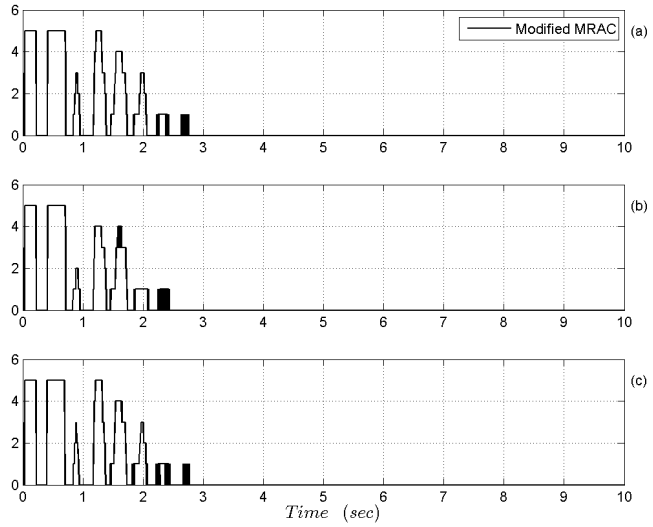

(b) Spoiler/MRAC configuration flutter control response to gust, at flutter speed and nominal stiffness, control signal time histories

Figure 4.28: Spoiler/MRAC configuration flutter control response to gust

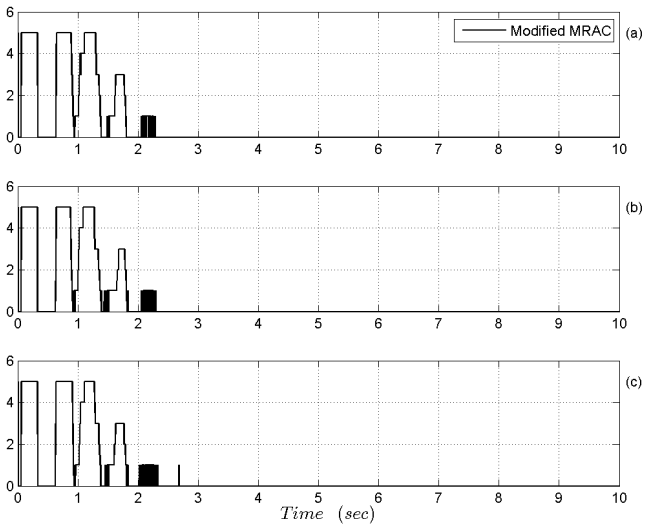

(a) Spoiler/MRAC configuration flutter control response to gust, at flutter speed and reduced stiffness, control signal time histories

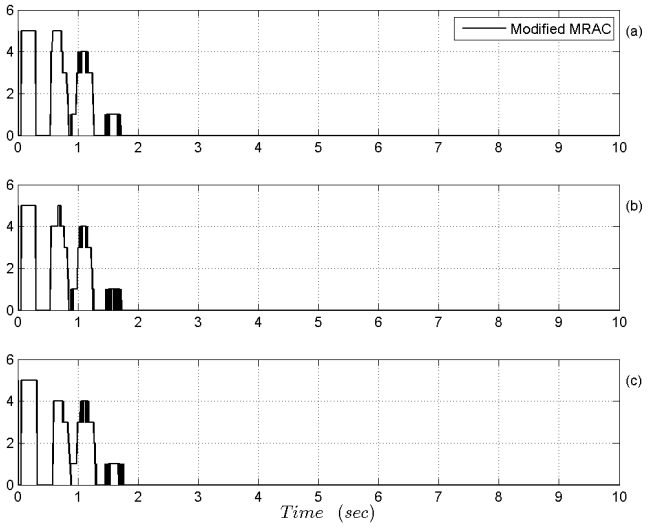

(b) Spoiler/MRAC configuration flutter control response to gust, at post flutter speed and reduced stiffness, control signal time histories

Figure 4.29: Spoiler/MRAC configuration flutter control response to gust

Chapter 5

Wing-Spoiler Configuration: Design, Prototyping and Experimental Setup

The proposed novel aeroelastic control architecture based on multiple spoilers' actuation, described in Chapter 2, Section 2.2, has also been prototyped and tested both for the aerodynamic database determination and to assess the feasibility in a real-world application. The design and manufacturing process, as well as the static and dynamic wind tunnel test campaign, are illustrated and discussed in this chapter. The novel control surface architecture has been conceived primarily to reduce lift and to generate an opposite sign pitching moment with respect to standard spoiler configuration. From the initial concept, the final actuation configuration has been achieved through several optimization steps. CFD analysis has been carried out to optimize the spoiler parameters, evaluating the effect in terms of aerodynamic coefficient variation, as addressed in Section 5.1. Once optimized, the available technology and budget have contributed to the decision of the material and actuator system employed on the final test article (Section 5.2). Static wind-tunnel testing has been set up and executed for aerodynamic coefficient evaluation, to guarantee consistency between the simulation and real-world wing model, in particular for control algorithm testing purpose (Section 5.3). The aeroelastic dynamic wind-tunnel test, implied the development of a 2 DOF plunging/pitching apparatus, which is described in Section 5.4. Finally an hardware setup has been assembled to allow closed-loop control of the wing section (Section 5.5).

5.1 CFD Analysis

An extensive set of CFD simulations, of which only the most relevant results will be shown and discussed, has been performed in order to optimize the

spoiler effect, evaluated in terms of aerodynamic coefficient. The aerodynamic numerical solver is the CFX module of ANSYS Workbench ver. 14.0. The wing section airfoil is a NACA 0024 with a chord length of 0.2 meters. A thick airfoil is required to accommodate the actuation mechanisms, as it will be explained in the next section. The three-dimensional wing model has a limited depth, with a spoiler spanning from one side to the otherside, compatible with the CFD investigation. The flow field is fully developed in a domain that is 10 chords long and 5 chords height (Figure 5.4c). The boundaries of the computational domain are far enough from the wing surface to cause negligible effect on the aerodynamic characteristics of the wing. The flow field has been discretized with a numerical mesh adequately dimensioned to obtain reliable results; if for the clear wing section configuration about 850,000 elements must be considered, more than 1 million elements are needed in meshing the domain which includes the wing-spoiler. Even if an unstructured mesh usually results in a lower fidelity than a structured mesh, it provides a computationally efficient solution to the problem at hand. In this investigation a triangular mesh was adopted, it simplifies the mesh generation around the spoiler edges, making the simulation more reliable. Figure 5.4a and Figure 5.4b show the numerical mesh generated. The macroscopic effect of the spoiler location is verified to assess the validity of the assumption on which the forward spoiler idea has grown. A constant setting of wind velocity vector equal to $[u \quad v \quad w] = [15 \quad 0 \quad 2](m/s)$, which makes the angle of attack constant at $7.59(deg)$, is used to give a rough estimation of the coefficient trend for three different spoiler positions. Precisely, the spoiler that have the same dimension of $15(mm)$ and opening angle of $54(deg)$, is analyzed in the rear (80%), middle (50%) and front (10%) positions. Results, reported in Figure 5.1, demonstrate that the pitching moment coefficient experience sign inversion when the spoiler location is moved forward crossing the zero value when in middle position. The well-known lift reduction and drag increment effect is reproduced. Once the desired effect and the corresponding spoiler position has been obtained, a fine tuning is performed to optimize the spoiler shape. The spoiler is parametrized as a function of size, opening angle, and position along the chord as shown in Figure 5.2. The mutual combination of these parameters is analyzed in the selected range of variation:

- Spoiler position: ranging from 10% to 30% of the chord length;
- Spoiler dimension: ranging form 10 to 25 mm;
- Spoiler opening angle: ranging from 30 up to 90 degree.

The boundary conditions are set as in Figure 5.4d, the bottom and front surface of the domain are considered inlet, the top and rear surface outlet. The velocity vector is maintained constant so as to reproduce an averaged

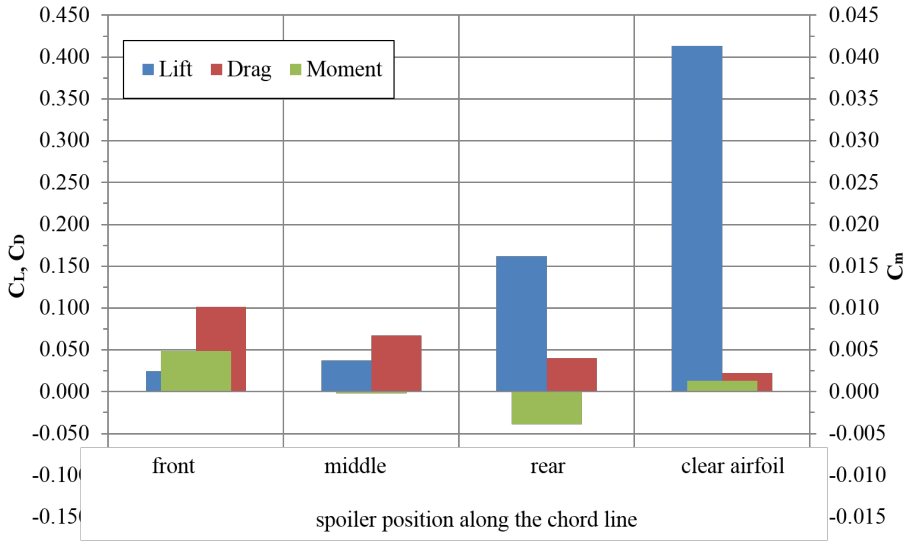

Figure 5.1: Spoiler location macroscopic effect

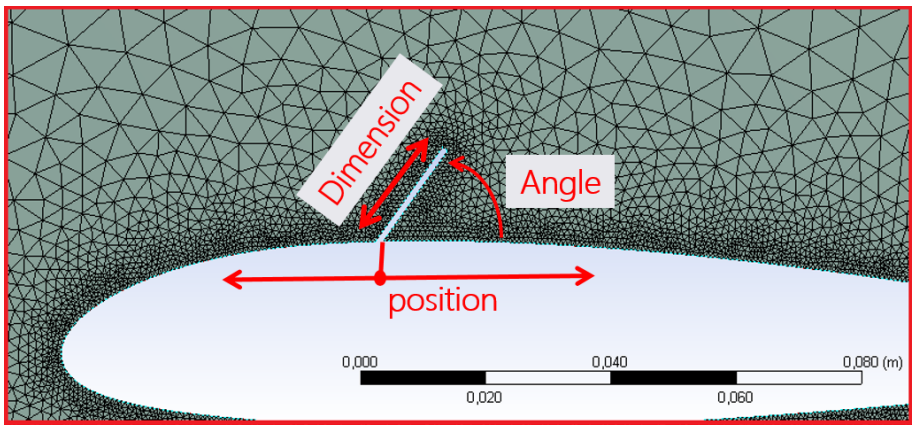

Figure 5.2: Spoiler parametrization

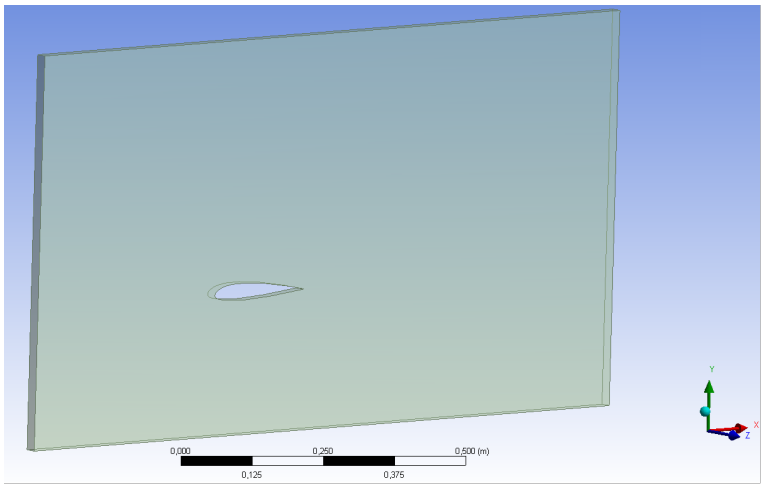

Figure 5.3: CFD simulation domain.

values of the wing angle of attack during LCOs. The turbulence intensity is set at a medium level (5%) and ambient sea level conditions are used for the flow-field. The outlets static relative pressure was set to be $0(Pa)$ and the flow is subsonic in the whole computational domain. The simulation is representative of an infinite wingspan with a two-dimensional flow by imposing symmetry on the two side walls of the computational domain. A standard roughness is set for the airfoil surface. The reference pressure is $101,325(Pa)$, and the turbulence model used is the *Shear Stress Transport* model, a modified $k-\omega$ turbulence model. Transitional turbulence option is enabled for more accurate low-speed computation. The convergence is smoothly reached after 350 iterations. The quality of the computation is verified by checking the Y+ on the surface of the wing, Figure 5.5a. Although $Y+ < 1$ is preferable, to strike a balance between accuracy and computational efficiency, a Y+ under 25 was considered to be acceptable. This is an adequate choice considering the preliminary nature of this parametric study in the spoiler design process. Some examples of the results achieved in terms of pressure distribution are reported in Figure 5.5.

The spoiler optimization process is performed iteratively by evaluating the effect of a single parameter modification per time. The other two parameters are maintained constant meanwhile. Starting from a standard spoiler configuration, defined as:

- Spoiler position: 70% of the chord length,
- Spoiler opening Angle: $30(deg)$,
- Spoiler length: $0.8(mm)$,

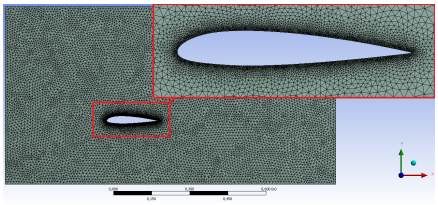

(a) Numerical mesh of clean configuration for CFD simulation.

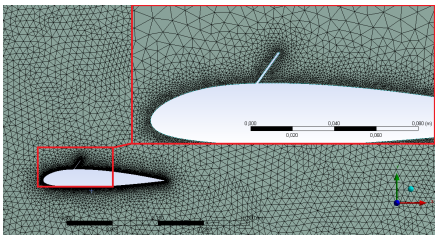

(b) Numerical mesh of active spoiler configuration for CFD simulation.

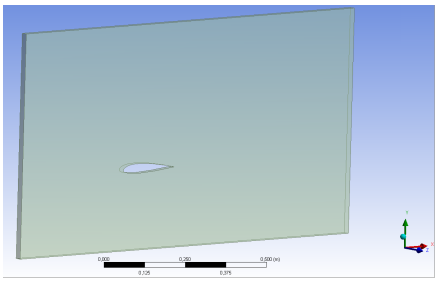

(c) CFD simulation domain.

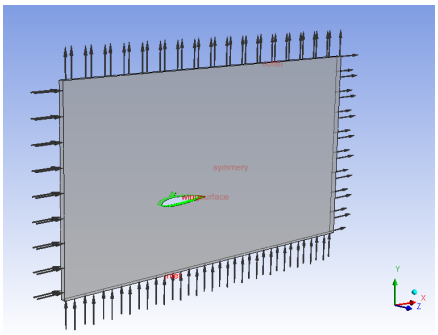

(d) CFD simulation, boundary conditions.

Figure 5.4: CFD parameter setup

the effect on the aerodynamic coefficients of the spoiler length modification is evaluated. From the same starting condition the same process is repeated for the opening angle parameter. Finally, the spoiler position is optimized maintaining constant the other two parameters at their already selected values. Again, Figure 5.2 describes the physical parameters of the spoiler optimization process. Recalling the main objective of the optimization process, Figure 5.6 reports the main results of the investigation and the chosen final configuration, highlighted by the red square boxes. Despite a negligible effect on δC_m provoked by the opening angle variation, the $90(deg)$ solution (which will become $85(deg)$ when prototyped) is chosen. This has been induced by considering the concurrent effect of lift reduction that is beneficial during flutter. The same argumentation is valid for the choice of the spoiler position parameter. Once the desired effect on the lift and pitching moment coefficient is obtained, the smallest length considered in the analysis is chosen. This is justified by the necessity of avoiding undesired coupling between flutter and lag motion during tests, caused by excessive drag acting on the opened spoiler.

Table 5.1: Spoiler Parameters Final Configuration

Parameter	Value
Position	$15\%chord$
dimension	$10(mm)$
OpeningAngle	$85(deg)$

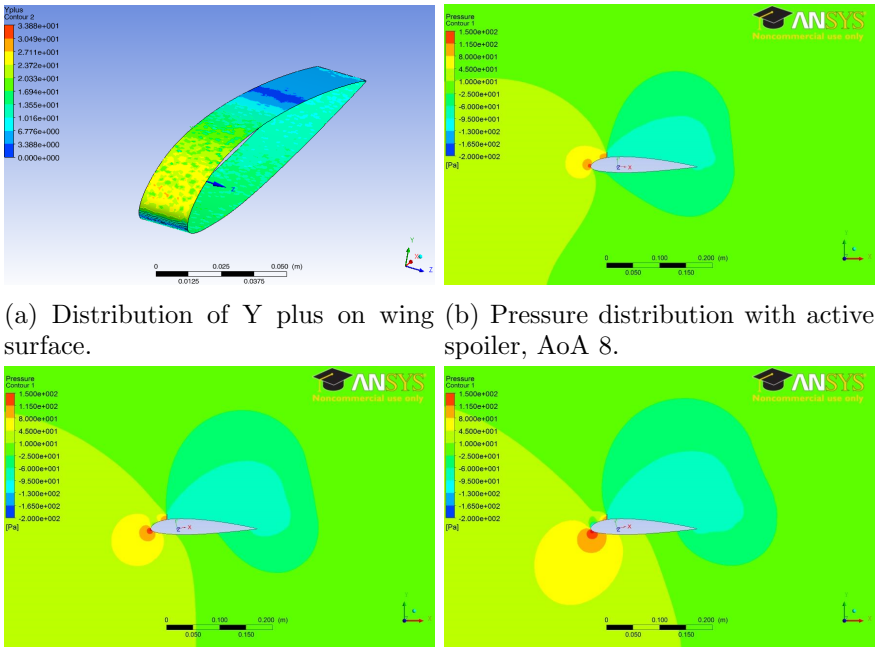

(a) Distribution of Y plus on wing surface.

(b) Pressure distribution with active spoiler, AoA 8.

(c) Pressure distribution with active spoiler, AoA 14.

(d) Pressure distribution with active spoiler, AoA 18.

Figure 5.5: CFD analysis, some results

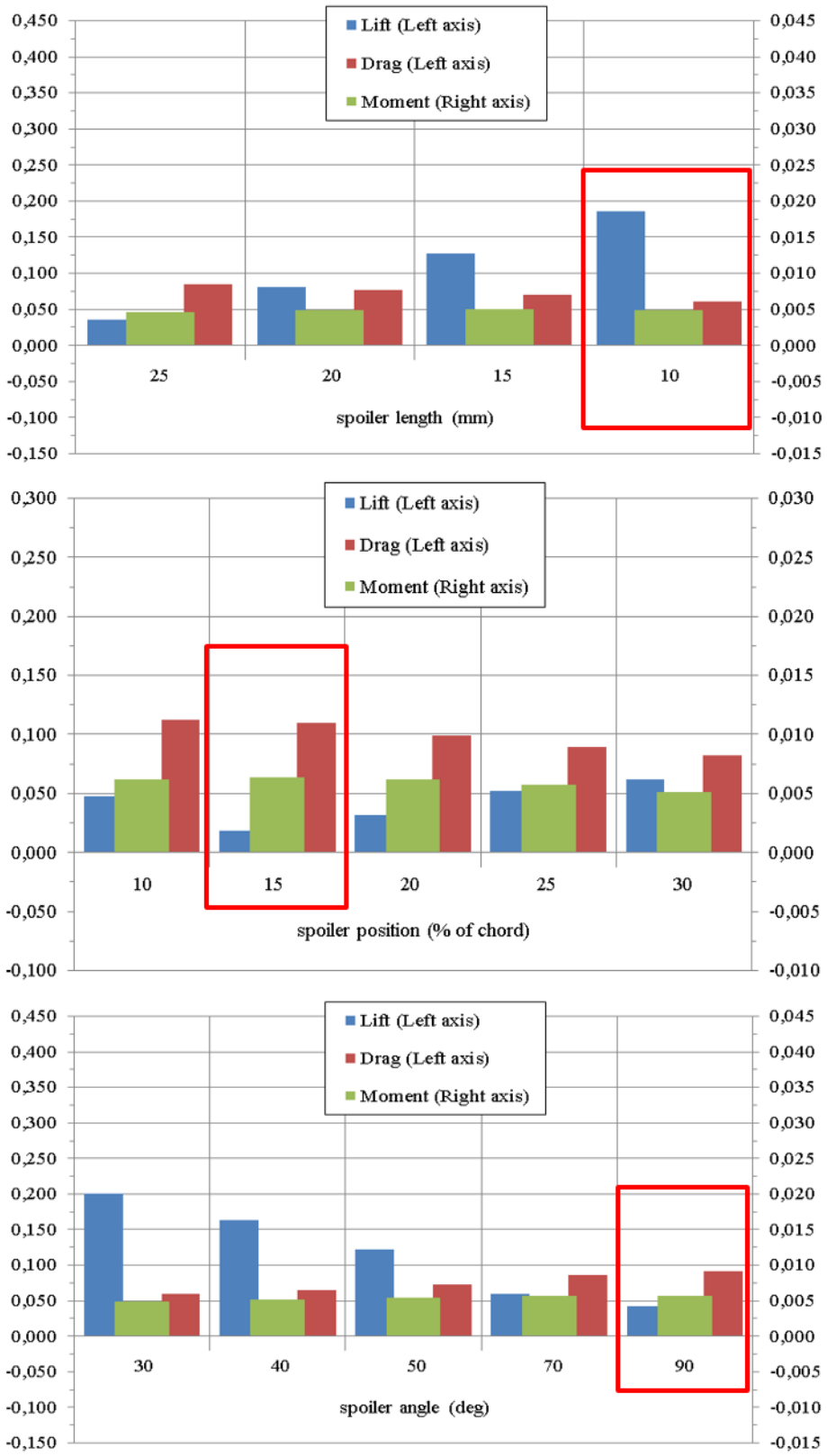

Figure 5.6: Spoiler optimization results.